Chapter 10

Numerical Simulations: Results

In this chapter we present the results of our numerical simulations for the six test cases mentioned in §9.1. Besides, relevant results from literature are presented for comparison and evaluation. The description of the results is sometimes accompanied by concluding remarks, though the main conclusions and general discussion of our results, and the vorton method in general, are postponed to Chapter 11.

10.1 Single Vorton Ring

In this section we compare the properties and characteristics of a single vorton ring, as illustrated in fig.9.1. In §10.1.1 we treat the velocity and vorticity distribution inside the core of the ring and its velocity of translation. In §10.1.2 the stability of vorton rings is discussed.

10.1.1 General Characteristics of the Vorton Ring

As mentioned in §9.1, the vorton ring is determined by four parameters: radius R, circulation Γ, strength γ of each vorton, and the number of vortons N. For given R and Γ, a relation between γ and N can be derived from relation (9.17).

In fig.10.1 a standard vorton ring ($N = 12$) has been visualized by means of isosurfaces of the magnitude of diagnostic $\tilde{\boldsymbol{w}}$ given by (9.18). Fig.10.1(a) shows that the vorton ring has a core. However, the contribution of each vorton remains detectable, which becomes clearer if the value of $|\,\tilde{\boldsymbol{w}}\,|$ is increased as shown by fig.10.1(b). Obviously, for larger number of vortons, the isosurfaces will become smoother.

In fig.10.2 the distribution of velocity and vorticity is shown for the core of a standard vorton ring along the lines indicated in fig.10.2(a). To avoid the singularity in both fields, the contribution of the vorton on line A has been disregarded. Comparison with the only experimental measurements known, from Maxworthy [149], shows reasonable qualitative agreement. Curve fitting has shown that the distribution of fig.10.2(b) can be described by a curve of the form $\mathrm{sech}^2(r)$ with r the radial distance from the core center which is the curve that has been proposed by Maxworthy.

The distances between the two peaks (maximum and minimum) in the velocity distribution as given in fig.10.2(c), can be taken as a measure for the core size a. In fig.10.3 the ratio between the non-dimensional core radius $\tilde{a}$, given by:

$$\tilde{a} \equiv \frac{a}{2\pi R/N}\,, \tag{10.1}$$

has been plotted as function of the number of vortons N and for the two lines across the ring shown in fig.10.2(a). In both cases, $\tilde{a}$ appears to converge towards a constant value. We conclude that for the standard vorton ring

$$a \propto \frac{R}{N} \quad \text{as} \quad N \to \infty\,. \tag{10.2}$$

(a)

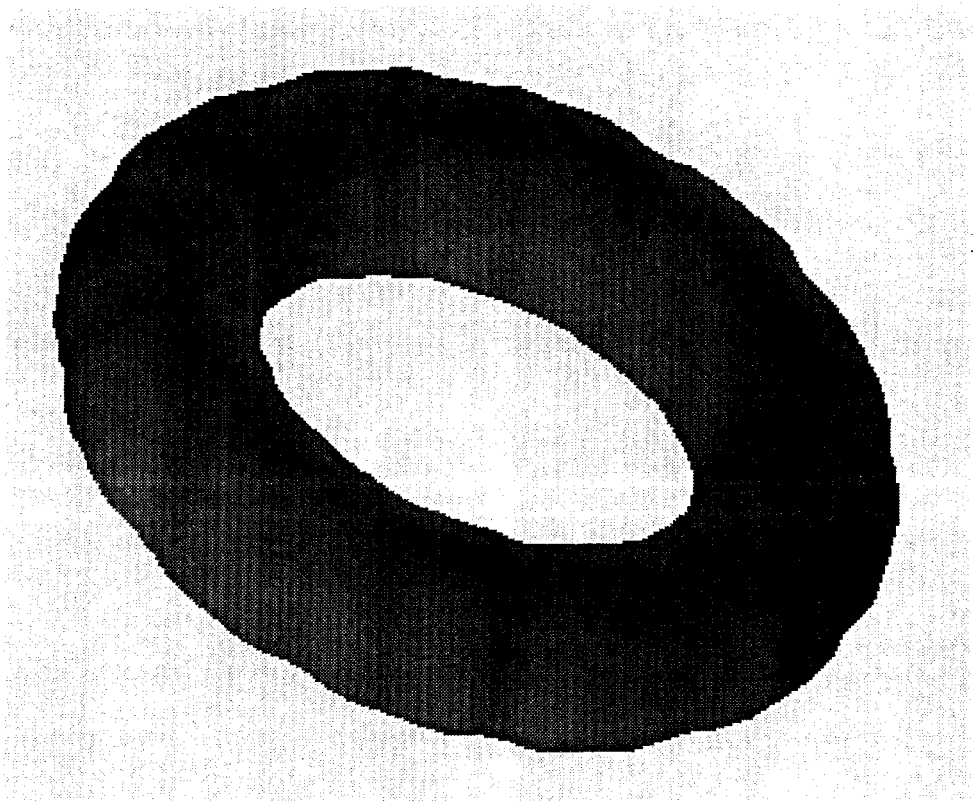

(b)

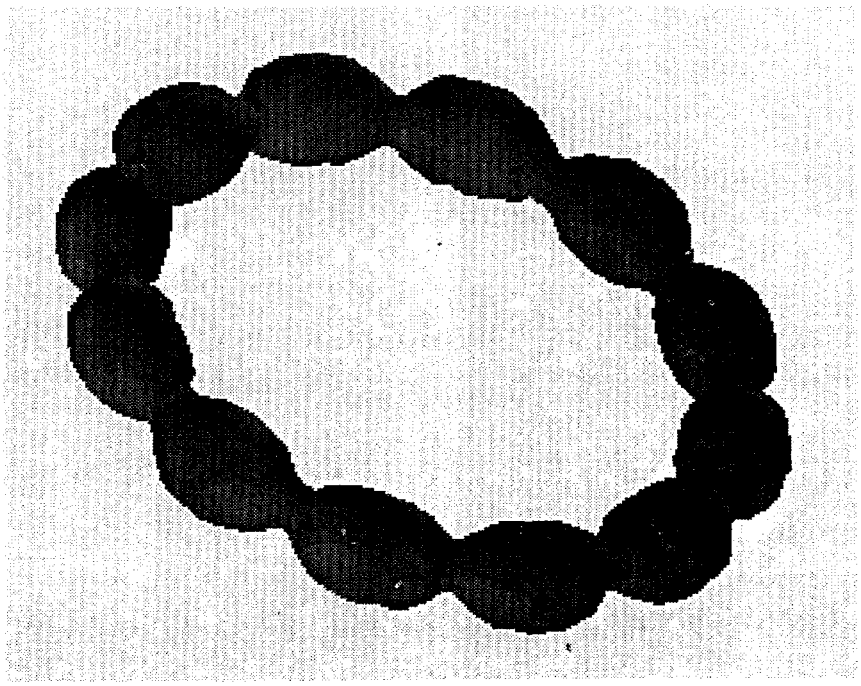

Figure 10.1: Single standard vorton ring ($N = 12$): isosurfaces of $|\ \bar{\mathbf{w}}\ |$ (see (9.18)) = (a) 1,000 $1/s$, (b) 10,000 $1/s$.

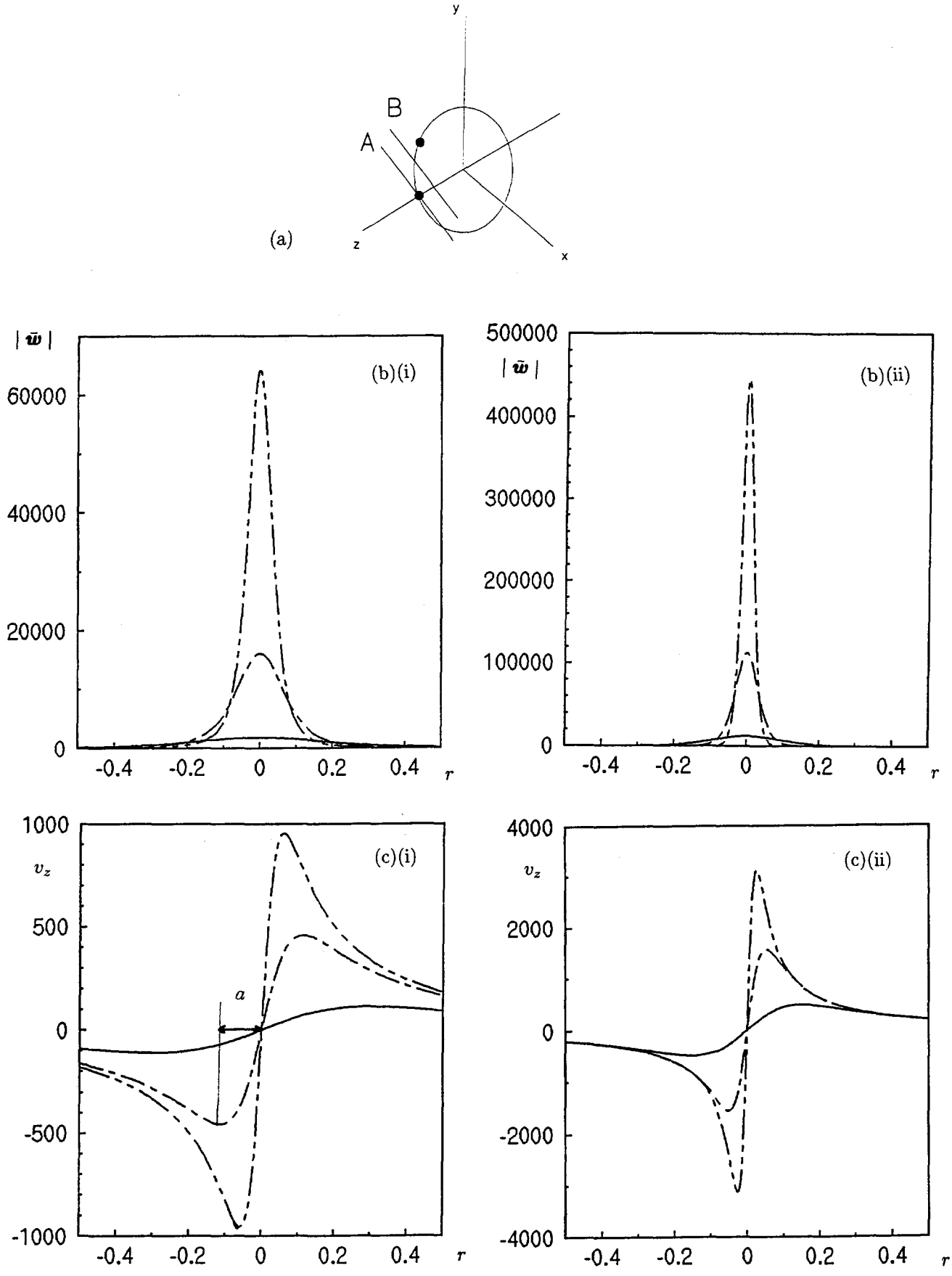

Figure 10.2: Single standard vorton ring (variable N): distribution of velocity and vorticity around the center line. (a) situation sketch (the dots indicate vorton locations on the vorton ring); (b) distribution of $|\,\tilde{\mathbf{w}}\,|$ (given by (9.18)) along (i) line A and (ii) line B; (c) distribution of velocity v_z along (i) line A and (ii) line B. Number of vortons $N = 12$ (—), 36 (– – –), 72 (– · – · –). r = distance along lines A and B. The contribution of the vorton on line A has been neglected. a is core radius.

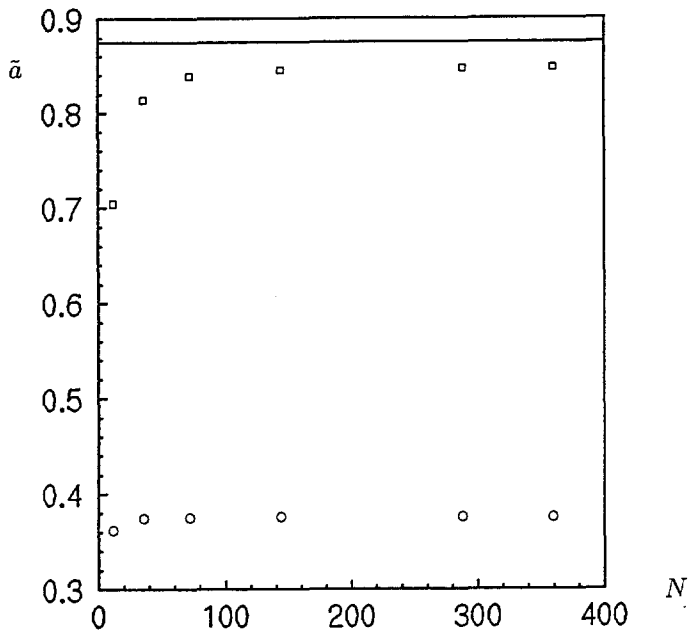

Figure 10.3: Single standard vorton ring: non-dimensional core radius $\tilde{a}$ (given by (10.1)) vs. number of vortons N. Core size a determined according to velocity distribution (see fig.10.2(c)) along line A (□) and B (○) (see fig.10.2(a)). The horizontal line $\tilde{a} \approx 0.875$ indicates the value derived from expression (4.3) for a Kelvin-ring.

However, the factor of proportionality appears to depend on the azimuthal location in the ring. In fig.10.3 we have also indicated the value of $\tilde{a}$ which follows for large N from Kelvin's expression (4.3) for the Kelvin-ring (see §A.2 of the Interlude); it appears to be ≈ 0.875 [1].

Fig.10.1 and figs. 10.2(b)(i) and (ii) show that the vorton ring has an azimuthally inhomogeneous distribution of vorticity. A large value for N can render a more homogeneous distribution in the ring. However, the value N can not be chosen at random when the circulation Γ, the radius R, and the velocity V of a ring are prescribed. This can be seen from the expression for V which can be derived from (10.2) and the general expression for the velocity of a vortex ring given in §A.2 of the Interlude:

$$V = \frac{\Gamma}{4\pi R}(\log N + A' - \frac{1}{2}) \,. \tag{10.3}$$

The factor A' depends on the factor of proportionality in (10.2) and on the vorticity distribution in the core, i.e. on N. Hence, the dependence of A' on N is ambiguous and complicated. In the simulations presented in the next sections, the determination of N has been done by taking the (integer) value of N which gives a velocity closest to the prescribed one.

We could wonder whether a change in the number of vortons also means a change in other properties of the vorton ring besides its core size. One indication may be gained from a calculation of the energy spectrum. In fig.10.4 the energy spectrum of a vorton ring ($R = 1$, $\Gamma = 1$) given by (9.11) is shown for two values of N.

[1] This value has also been found by Pedrizzetti [177].

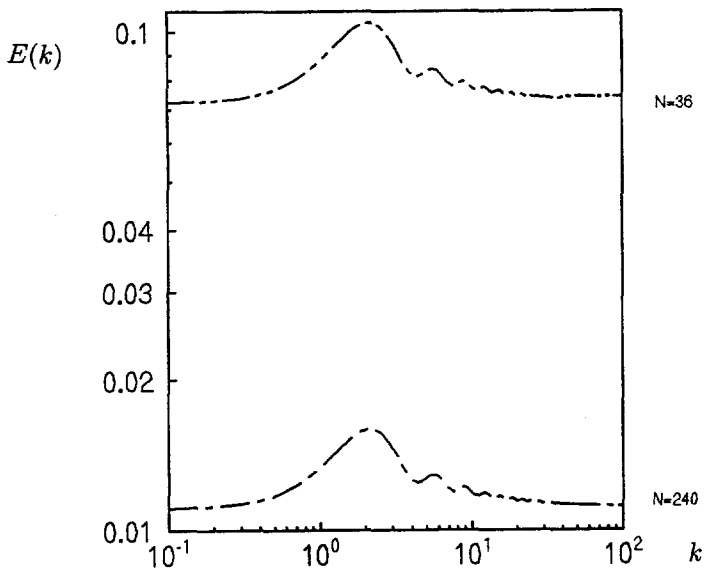

Figure 10.4: Single vorton ring ($R = 1, \Gamma = 1$): energy spectra $E(k)$ according to (9.11) for number of vortons $N = 36$ and $N = 240$. k is wavenumber.

We observe that the shape of the spectra is identical for both values of N; they are only shifted along the vertical axis. Apparently, the number of vortons does not influence the physical character of the vorton ring. However, with regard to the shape of the spectrum itself it is hard to make any remarks. According to the analytical result presented in [121] for a "coreless" vortex ring, the spectrum of a ring consists of two parts: a k^2 behaviour for small k is due to the nonzero impulse of the ring; a $1/k$ behaviour for large k is that of an isolated smooth vortex tube with $ka \ll 1$ where a is the core size. We could conclude from fig.10.4 that our vorton ring is not "coreless". Unfortunately, we have no information on the exact definition of this vortex ring and other (experimental) results have not been found.

10.1.2 Stability of the Vorton Ring

In §A.3 of the Interlude, the development of research on the stability of vortex structures (especially vortex rings), stimulated by Kelvin's vortex atom theory, has been reviewed. The work by Widnall and others on the stability of vortex rings has shown that even in the inviscid case instability can set in [2].

Numerical investigation of the stability of vortex rings has been performed by Knio & Ghoniem [108]. They used a vortex method which can be compared to the soft-vorton method (see Appendix B).

We have simulated the same rings as those used by Knio & Ghoniem, i.e. radius $R = 1$ and circulation $\Gamma = 2$. The initial disturbance has been a sinusoidal radial disturbance, given by:

$$\Delta R \sin(n\theta) \tag{10.4}$$

[2]The influence of viscous effects on the stability behaviour of vortex rings might be negligible, as is reported in e.g. [128].

where ΔR is the amplitude of the disturbance, n is the wavenumber and θ is the azimuthal coordinate (see fig.c of the Interlude for an illustration). For ΔR the value $0.02 * R$ has been chosen. The value of n has been varied and the value at which the amplitude of the disturbance increased fastest, is called n^*. In fig.10.5 the most unstable wavenumbers n^* are plotted against the non-dimensional velocity of the ring $\tilde{V}$, given by:

$$\tilde{V} \equiv V \frac{4\pi R}{\Gamma} \tag{10.5}$$

where V is the ring velocity, calculated directly from the displacement of the vorton ring. The

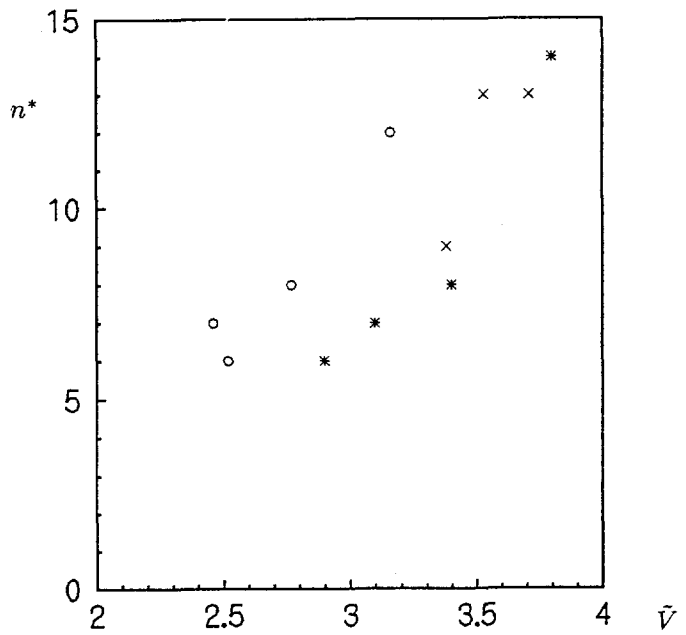

Figure 10.5: Single vorton ring ($R = 1, \Gamma = 2$): most unstable wave number n^* vs. the non-dimensional ring velocity $\tilde{V} = V(4\pi R/\Gamma)$. Results for ($\times$) the vorton ring are compared to ($*$) numerical results from [108] , and ($\circ$) experimental results from [278] .

amount of data may seem small. Unfortunately, the range of values of $\tilde{V}$ for which Knio & Ghoniem provide data is in a region where, for $\Gamma = 2$, the number of vortons in the vorton ring is about twice the number of waves n. This means that the representation of the sinusoidal disturbance is inaccurate with unknown effect on the instability behaviour of the vorton ring.

Nevertheless, we conclude that the stability behaviour of the vorton ring compares reasonably well with the numerical results of Knio & Ghoniem. However, both our and Knio & Ghoniem's results do not compare very well with experimental data as given by Widnall & Sullivan [278], also indicated in fig.10.5.

10.2 Behaviour of a Single Pseudo-Elliptical Vorton Ring

10.2.1 Introduction

The dynamics of a single vortex ring becomes much more interesting (and complicated) when its shape is changed from circular to elliptical. From accounts of the smoke ring experiments performed by Kelvin and Tait in the 1860s, it appears that they already recognized the peculiar

behaviour of elliptical rings (see §3.2). However, only in recent years this behaviour has been studied more deeply.

The behaviour of an elliptical ring is determined by its inclination to "oscillate", i.e. to constantly interchange its long and short axis. This can be ascribed to the variations in curvature, which induces unequal velocities along the circumference of the ring. The parts of largest curvature will move forwards at a higher velocity than the other parts of the ring, causing a bending of the ring perpendicularly to its plane. The parts staying behind will start to move outwardly, causing the the change of axes, mentioned above. The oscillating behaviour is clearly exposed in fig.10.6.

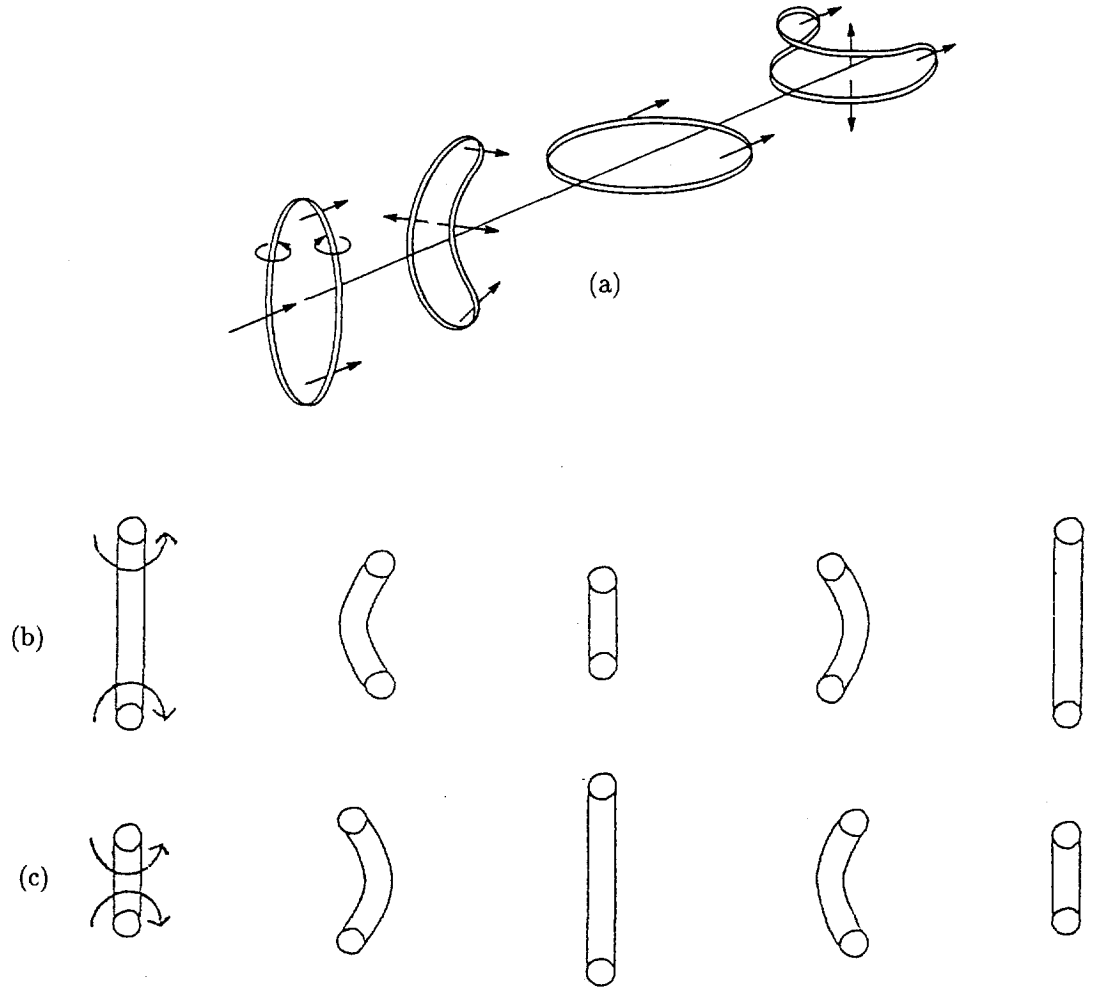

Figure 10.6: Oscillating behaviour of an elliptical vortex ring: (a) perspective view (sketch from [134]); (b) side-view; (c) top-view. Development in time is from left to right.

It has been shown experimentally that the behaviour of elliptical rings depends on the ratio of the lengths of the major and minor axis of the ellipse. When this ratio exceeds a certain value the periodic oscillating behaviour of fig.10.6 is "disturbed" due to vortex reconnection.

Kiya & Ishii [105] performed numerical simulations applying a soft-vorton method and did

experiments on the behaviour of a so-called pseudo-elliptical vortex ring whose shape is shown in fig.10.7. This ring is supposed to show similar behaviour as purely elliptical rings. They

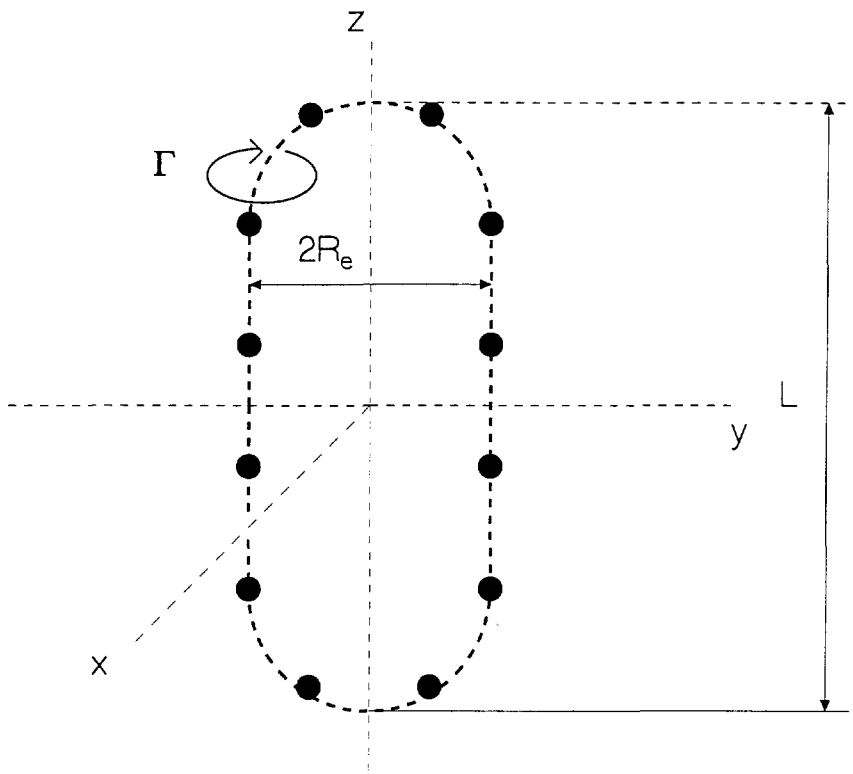

Figure 10.7: A pseudo-elliptical vorton ring. The dots indicate the vorton locations.

observed at least two different regimes in the behaviour of these rings, depending on the axis ratio $L/2R_e$:

1. for $2 < L/2R_e < 4$: oscillation as in fig.10.6 with a continuous interchange of the position of the long and short axis;

2. for $5 < L/2R_e < 8$: the ring's axes interchange one time (as in the first half of fig.10.6)(b); this is followed by splitting up into two rings.

As remarked above, the splitting behaviour may be attributed to the phenomenon of reconnection, introduced in the Interlude [3]. When the long straight parts of the ring approach each other under certain conditions, they are cut and reconnected as illustrated in fig.e of the Interlude.

10.2.2 Vorton Simulations

For our numerical simulations, we have taken the vorton representation of Kiya & Ishii's pseudo-elliptical ring (see fig.10.7). For this ring circulation $\Gamma = 225$ and $R_e = 1$. By changing the value of L we can change its axis ratio.

[3] We shall return to this topic in §10.4.

The behaviour of this ring with $N = 32$ and $L/2R_e = 7$ is shown in fig.10.8 in case of application of all three vorton deformation equations, i.e. the N-, K-, and N+K-equations. In case of the K-equation the simulation had to be stopped after a short time as the vorton strengths of some vortons increased dramatically. Time step reduction did not show improvement in this case. The other two cases (figs. 10.8 (a) and (c)) show qualitatively similar behaviour.

In fig.10.9 the development of the the x-component of linear momentum $\boldsymbol{P}$ according to (9.5), interaction-energy E_i according to (9.10), and self-energy E_0 according to (9.14) are shown for the three cases of fig.10.8. The results for the K-equation show severe violation of conservation of $\boldsymbol{P}$ and E_0. We observe that qualitatively the N-equation and the N+K-equation show no large differences, so that no preference for one of these can be expressed based on these results. However, the results on the conservation of $\boldsymbol{P}$ and E_i suggest that the N+K-equation performs slightly better.

The influence of the number of vortons N on the diagnostics has been investigated in case of the N+K-equation. In fig.10.10, the development of the same diagnostics as in fig.10.9 are shown for two values of N and an axis ratio of $L/2R_e = 7$. We again observe that the invariants are reasonably well conserved. For increasing N their deviations from perfect conservation decreases. Furthermore, we note that the curves of interaction-energy E_i and of self-energy E_0 show opposite behaviour.

Regarding the two different regimes of behaviour mentioned above, for our pseudo-elliptical ring (in case of the N+K-equation) we found that regime 1 occurs for $L/2R_e < 8$. Regime 2 does not occur, though in some range of $L/2R_e$ the behaviour seems close to reconnection (as can be observed in fig.10.8(c)). An increase of the numbers of vortons N showed an inclination towards regime 2 for the axis ratios found by Kiya & Ishii. However, above a certainvalue of N the initially straight parts of the pseudo-elliptical rings became unstable and the ring collapsed.

The disagreement between our numerical results and the results given by Kiya & Ishii has been confirmed by a comparison of our numerical results with the results from a simple experiment which we performed with smoke rings in the manner of Tait's 1867 experiment discussed in §3.2 [4]. In fig.10.11 we show both the isosurfaces of the magnitude of diagnostic $\bar{\boldsymbol{w}}$ given by (9.18) for our pseudo-elliptical vorton ring ($N = 8$, N+K-equation) and photographs of the experimentally observed smoke rings. In both cases the axis ratio $L/2R_e = 7$.

One possible explanation for the disagreement between vorton simulation and experiment is the presence of a slight restriction in the middle of the straight part of the smoke ring caused by the way of generation. We have tried to simulate this restriction as indicated in fig.10.12. For a slightly disturbed pseudo-elliptical vorton ring [5], reconnection indeed occurred for $L/2R_e = 7$. However, shortly after the splitting, the two rings linked to become one ring again; see fig.10.12. Apparently, the cause for the inability of our vorton simulation to show

[4] For a full description of our experiment, we refer to [44].

[5] The exact nature of the restriction appeared to be irrelevant. Fig.10.12 shows a simulation in which a sinusoidal disturbance on the straight parts of the ring has been imposed (see the sketch).

Figure 10.8: (*see inserted sheets*) Single pseudo-elliptical vorton ring ($N = 32, L/2R_e = 7$): behaviour in case of (a) N-equation, (b) K-equation, (c) N+K-equation. Three views of the ring are given at each time t.

$t = 0$

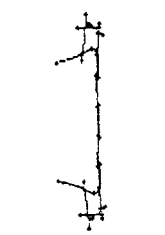

$t = 0.28$

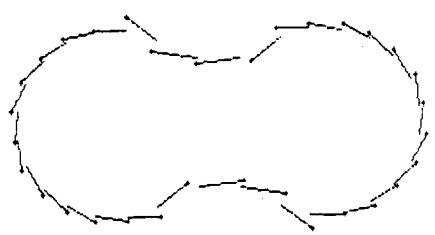

$t = 0.56$

$t = 0.84$

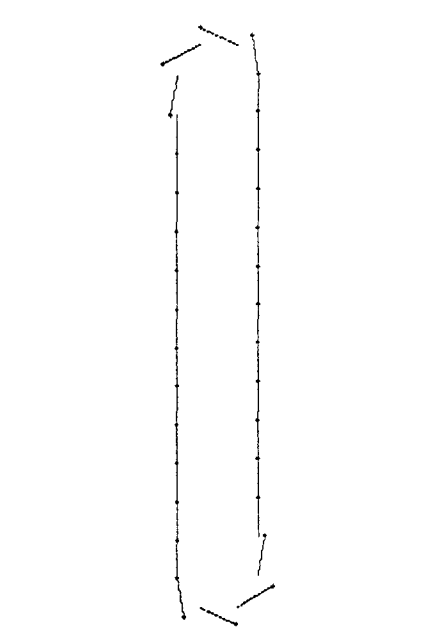

$t = 1.12$

$t = 1.40$

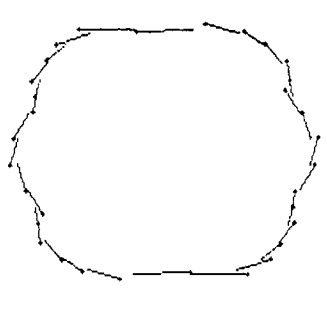

$t = 1.68$

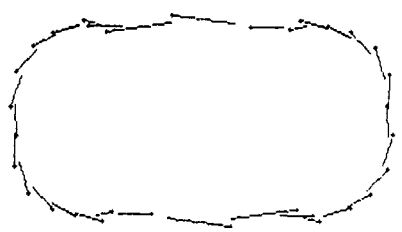

Figure 10.8 (a)

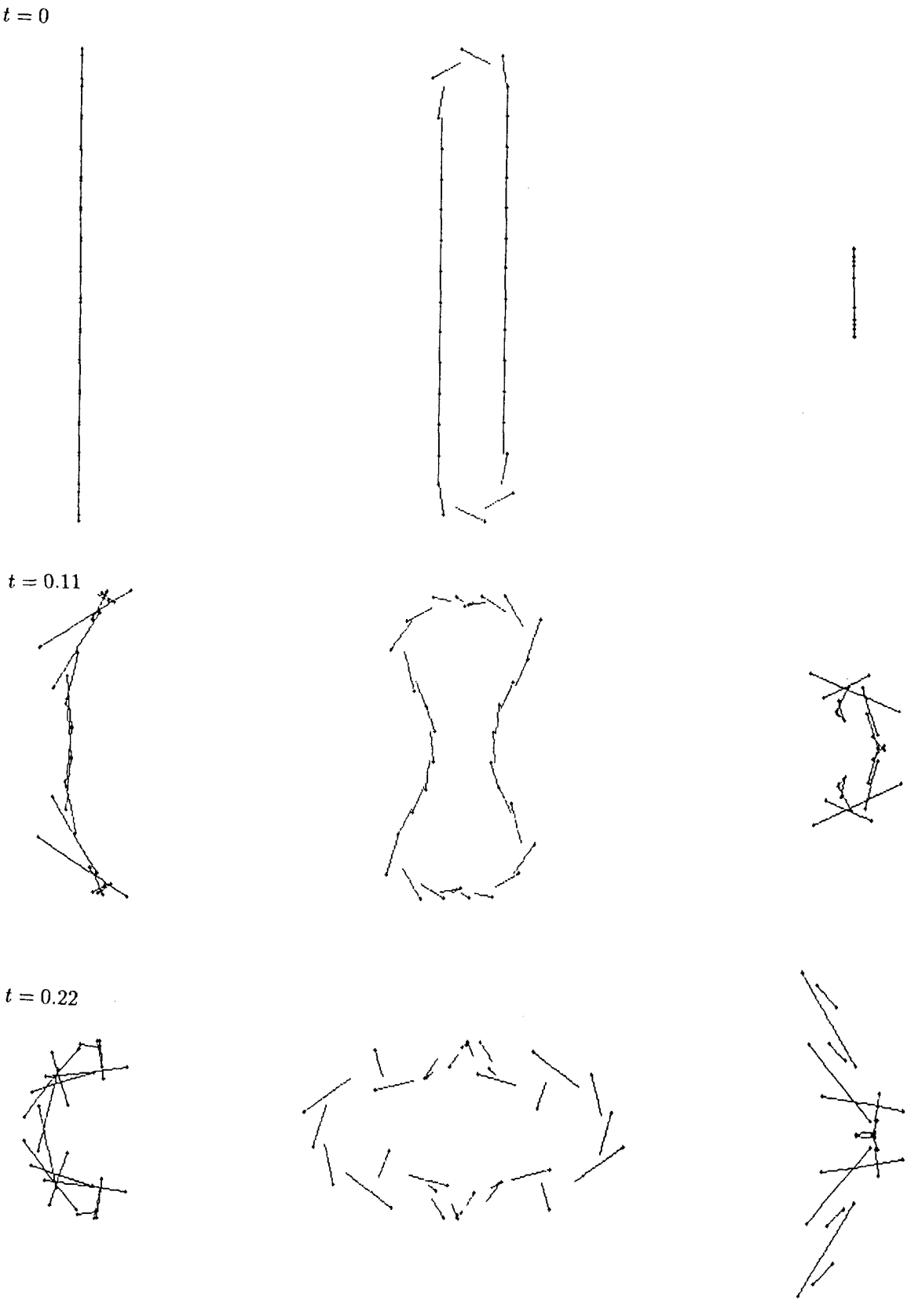

Figure 10.8 (b)

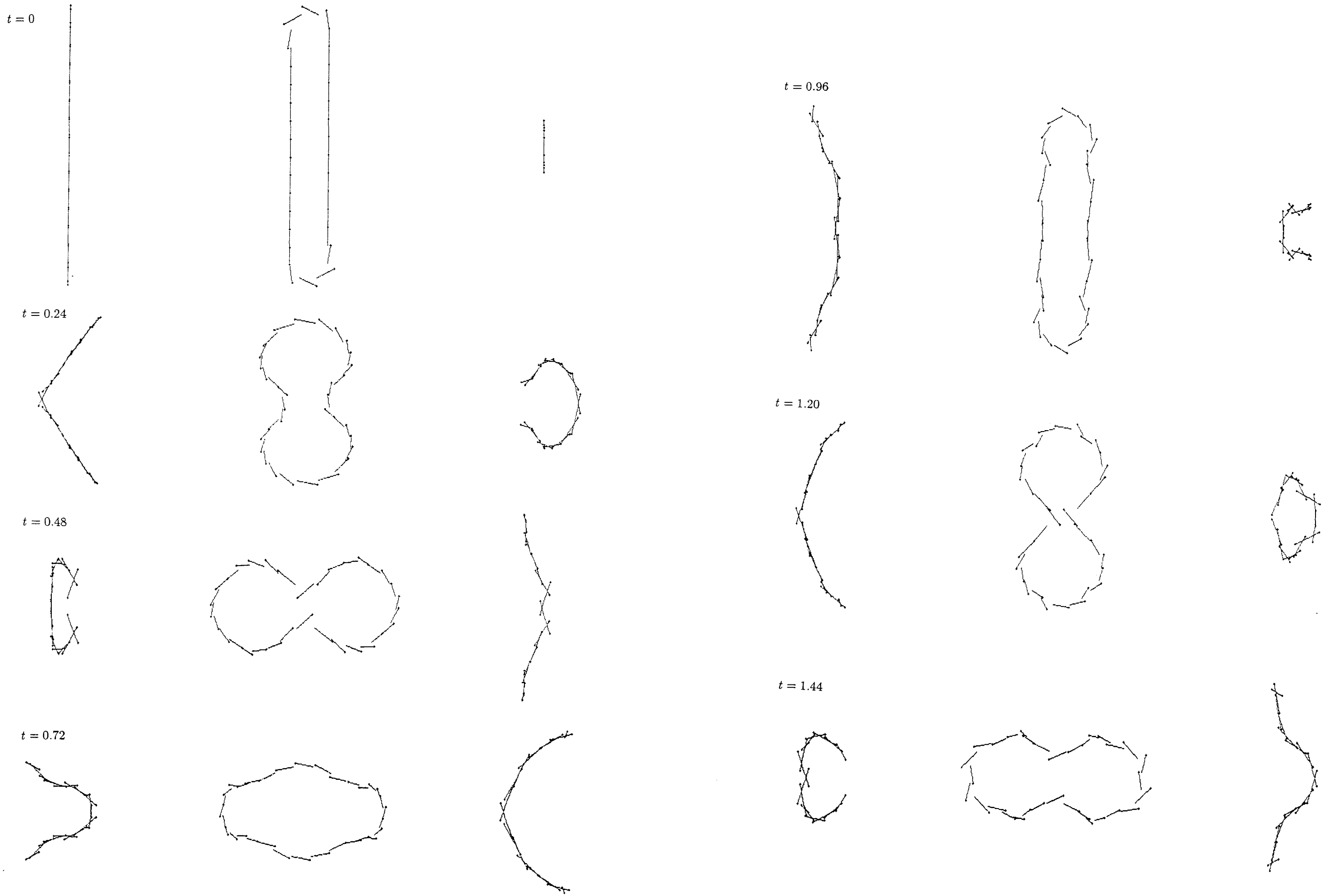

Figure 10.8 (c)

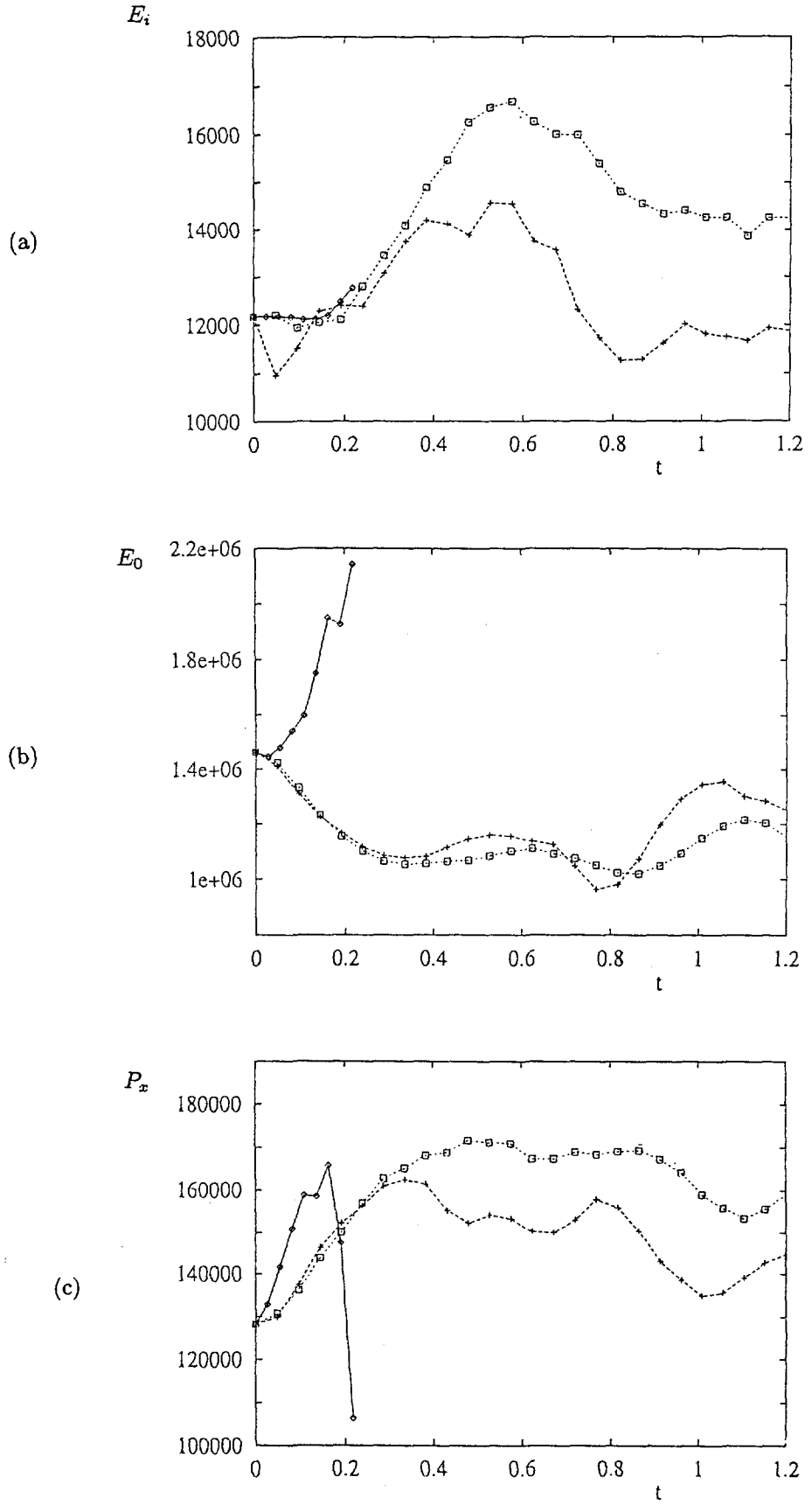

Figure 10.9: Single pseudo-elliptical vorton ring ($L/2R_e = 7, N = 32$): (a) interaction-energy E_i according to (9.10), (b) self-energy E_0 according to (9.14), (c) x-component of linear momentum $\mathbf{P}$ according to (9.5). Vorton deformation according to (□) N-equation, (◇) K-equation, (+) N+K-equation. t is time.

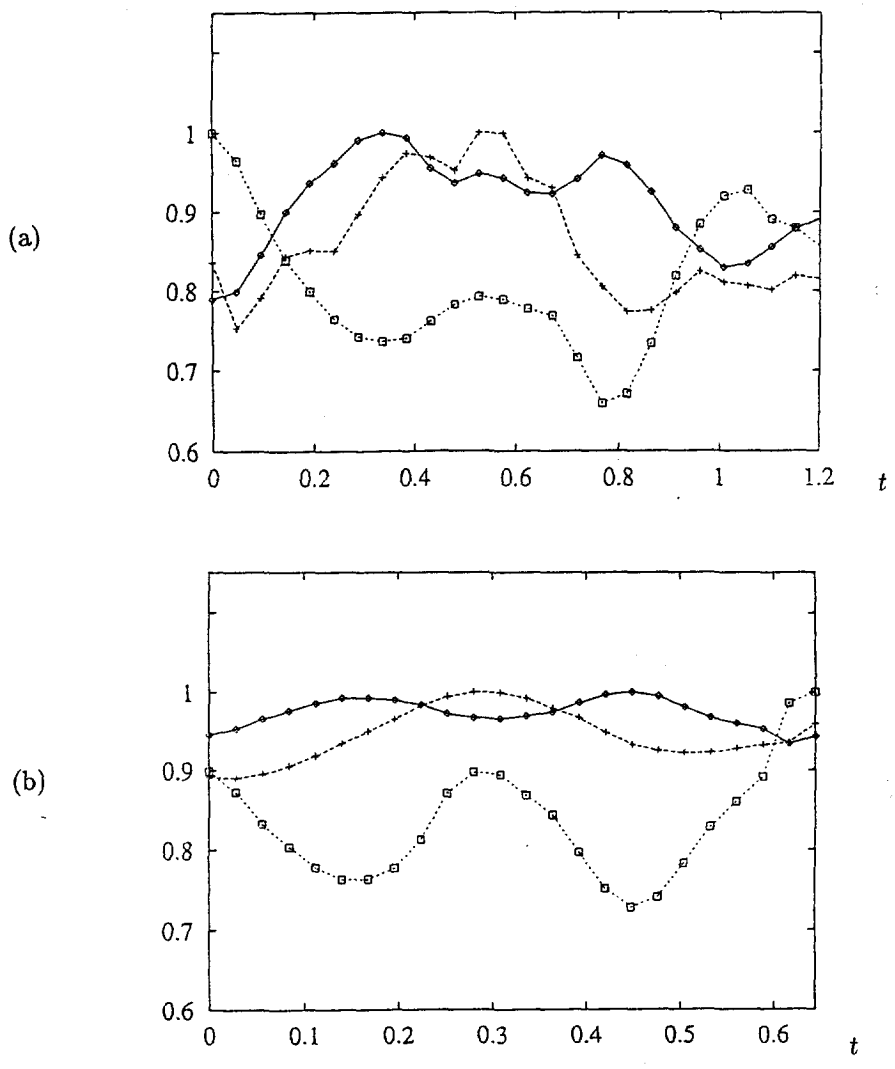

Figure 10.10: Single pseudo-elliptical vorton ring ($L/2R_e = 7$) consisting of N = (a) 32, (b) 192 vortons: (+) x-component of linear momentum $\mathbf{P}$ according to (9.5), ($\diamond$) interaction-energy E_i according to (9.10), ($\square$) self-energy E_0 according to (9.14). (The curves have been rescaled such that their maximum equals 1.) t is time.

reconnection has to be found elsewhere. This will be further discussed in Chapter 11.

Though the experiment mentioned above has been relatively simple, we have been able to compare one quantitative result. For both the vorton rings and the smoke rings of low axis ratio ($L/2R_e \leq 3.5$) the product of the period of one oscillation τ and the average ring velocity V have been calculated [6]. In fig.10.13 the results are compared. For the vorton simulations both the N- and N+K-equation have been used. In both cases the number of vortons N has been chosen such that the numerical results agreed best with the experimental results. This

[6]It can be shown that this quantity is independent of the circulation Γ. This is a fortunate circumstance, since Γ is hard to measure. See [44] for details.

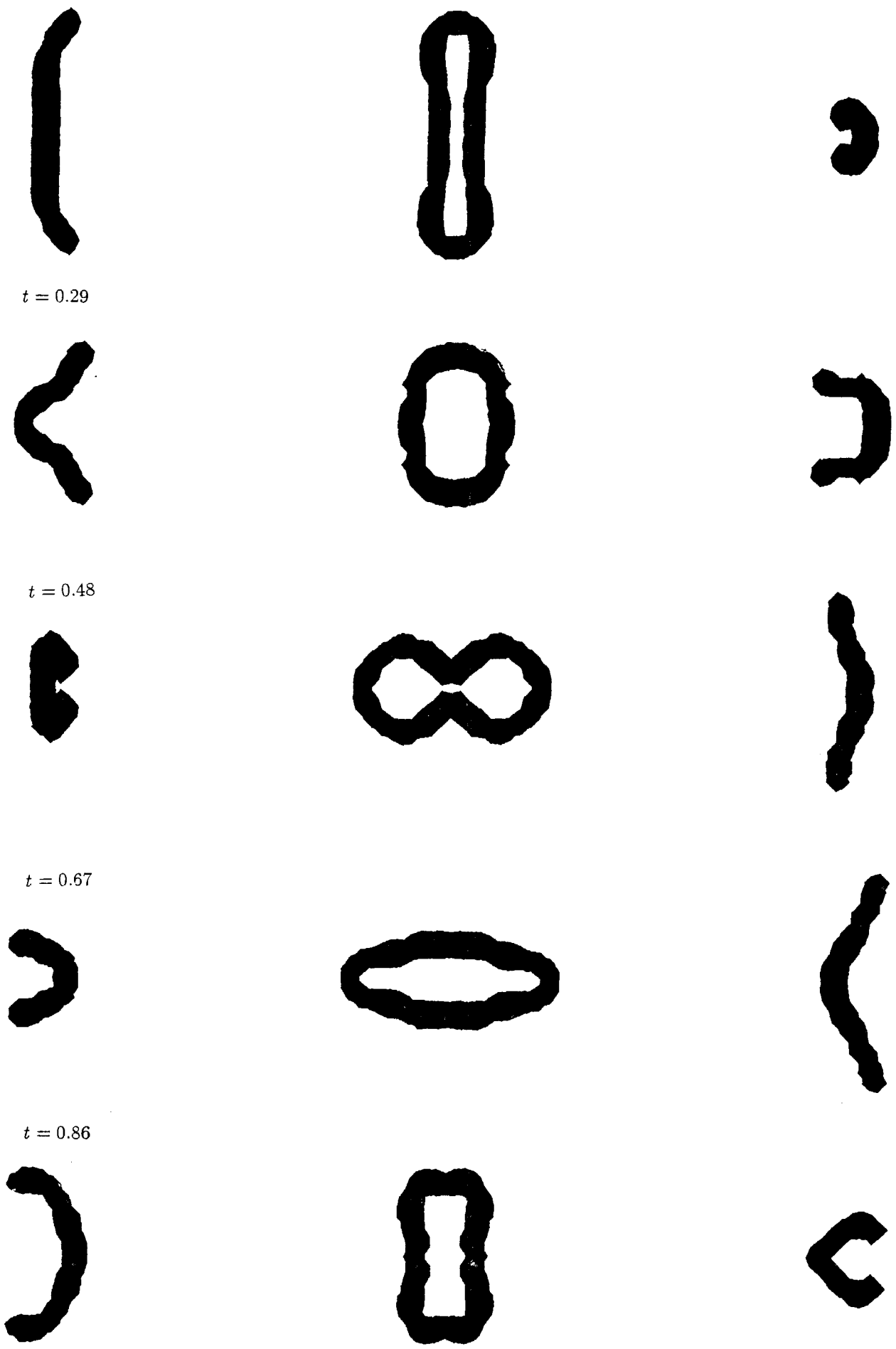

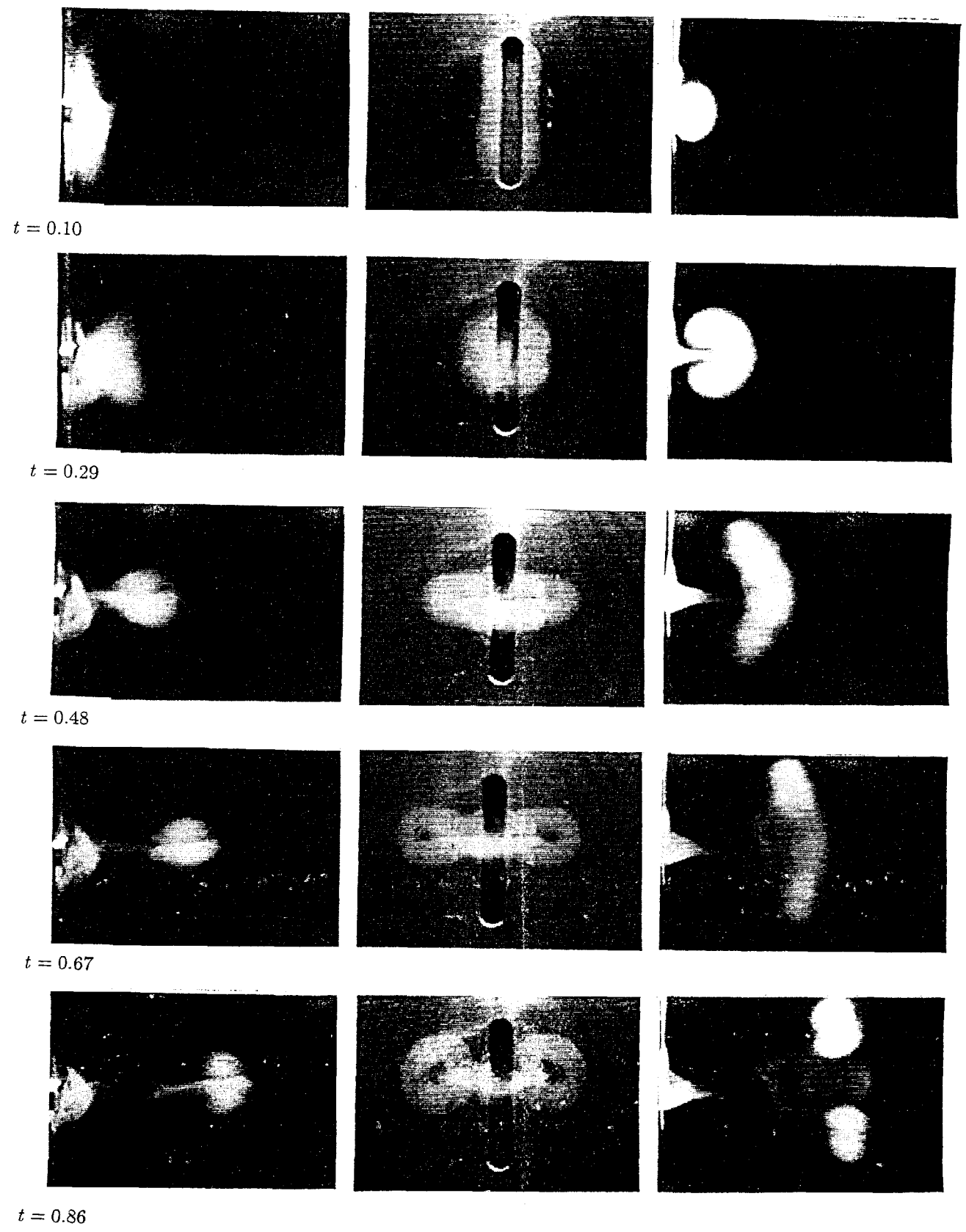

Figure 10.11

resulted in $N = 10$ in case of the N-equation and $N = 8$ in case of the N+K-equation. We observe agreement between numerical and experimental results with regard to the trend of the curves. The N-equation seems to perform somewhat better. However, the fact that vorton rings can only contain discrete values of N strongly restricts the adaptation of the numerical ring to the experimental ring.

10.3 Head-on Collision of Two Coaxial Vorton Rings

10.3.1 Introduction

As remarked in Chapter 2, in 1858 Helmholtz had already showed that if two coaxial and identical vortex rings approach each other, their radii increase and their velocities decrease. He had also remarked that this situation could be compared to a single ring approaching a flat wall perpendicularly, in which case the ring collides with its own "mirror" image (compare fig.7.1). The former case will be called ring/ring interaction and the latter ring/wall interaction.

The initial configuration of ring/ring interaction is shown in fig.10.14. Notice that this configuration can only represent ring/wall interaction if the free-slip condition on the wall is valid, i.e. if no condition is imposed on the tangential velocity at the (imaginary) wall.

In §A.2 of the Interlude we mentioned Dyson's impressive analytical results of 1893 on this configuration. After Dyson's remarkable paper, it seems to have lasted more than 70 years before interest in the interaction of vortex structures with planes, or other objects, revived. Direct incentive for this revival can be found in the concern which arose in the early 1970s over the hazard presented by trailing vortices as produced by large aircrafts [276], which could interact with the ground and other aircrafts. One of the phenomena only then discovered was the rebound effect: at close approach towards a wall the movement of the vortex showed reversion, i.e. the vortex started to move away from the wall. Though initially the rebound was explained by inviscid core deformation (see [128]), it soon became clear that the effect was due to the influence of the boundary layer: when the distance between ring and wall is of the order of the apparent thickness of the core, the boundary layer is disturbed and a secondary ring is generated at the wall, which induces an upward motion on the approaching ring and sends it from the wall (see e.g. [274]). After the rebound the first ring may again approach the wall since the secondary ring becomes weaker, and the rebound may occur again.

More generally, the rebound effect made clear that interaction of vortex structures with viscous boundaries (no-slip condition) are fundamentally different from inviscid boundary interactions (free-slip condition) represented by mirrored structures.

10.3.2 Recent Results from Literature

While results on ring/ring interaction are scarce, ring/wall interaction has been given more attention. Chu *et al.* [40] have done experimental work on rings approaching both a solid surface and a (slightly contaminated) free surface. For the circulation of the ring, they have found that during the free-travelling stage Γ is almost constant, while during the vortex stretching at close approach of the surface Γ strongly decreases. This violation of Kelvin's Circulation The-

Figure 10.11: (*see inserted sheet*) Single pseudo-elliptical vorton ring ($N = 8$, $L/2R_e = 7$): comparison between numerical simulation (in case of N+K-equation) and experimentally produced smoke ring. The vorton ring is represented by isosurfaces of $|\ \tilde{\mathbf{w}}\ |$ given by (9.18). Three views of the ring are given at each time t.

orem indicates that viscosity becomes influential at that stage. Apparently the only numerical simulation on this configuration has been performed by Kambe and co-workers. Their viscous vortex model also showed a variation of circulation: first it is constant, then it decreases at close approach. Energy appeared to decrease from the start [98].

The only recent experiment on head-on colliding vortex rings seems to have been performed by Lim *et al.* [128]. They have compared the ring/ring interaction with the ring/wall interaction. During the ring/ring interaction, the radius of each ring continues to increase, in good agreement with Dyson's equation (see fig.d of the Interlude). They have found no rebound effect for the ring/ring interaction and concluded that the generation of secondary vorticity at the wall is indeed the cause of rebound in the ring/wall case. For the ring/ring case, the experiments also showed that an azimuthal instability can develop along the rings. A remarkable consequence of this wave formation is the formation of smaller rings around the circumference of the original rings. Once formed, these move outward radially [7].

10.3.3 Vorton Simulations

We have simulated the head-on collision of two standard vorton rings with the number of vortons per ring $N = 36$ and the vortons in both rings located opposite each other. Initially, the rings are separated 4 times the initial radius R, i.e. $d = 4R$ and $R = 0.8\ cm$; see fig.10.14. Only the N+K-equation has been applied, since all three vorton deformation equations showed the same simulation results.

In fig.10.15 we compare the development of radius R of the approaching rings as a function of their distance (i.e. the distance between opposite vortons), given by d. It shows good qualitative agreement with Dyson's analytical curve for the Kelvin-ring, given in fig.d of the Interlude [8]. The curve shows no rebound.

From fig.10.16 we derive that distance d between the rings, defined as the distance between the opposite vortons in both rings, almost stops decreasing as radius R of each ring starts to increase strongly. This moment will be called t^* and it is about equal to 0.006. Comparison with fig.10.15 shows that t^* is also the moment R starts to increase severely.

Apparently, the rings have a core which hinders their approach beyond a (small) distance. It should be mentioned that Dyson's elaboration also predicts a lower limit for the distance d.

To find out what is happening to the core during collision, we show in fig.10.17 and fig.10.18 contour plots of $\mid \tilde{\boldsymbol{w}} \mid$ (given by (9.18)). The first figure shows the deformation of the core in plane A of fig.10.14, the other the same result in plane B. In both figures, we depict at $t = 0$ the same maximum value of $\mid \tilde{\boldsymbol{w}} \mid$ in order to show the difference in the vorticity distribution between the two locations. At subsequent times, the values of $\mid \tilde{\boldsymbol{w}} \mid$ on the contour levels has been adapted to the overall maximum of $\mid \tilde{\boldsymbol{w}} \mid$ in each plane.

[7] This phenomenon resembles the formation of rings in the so-called Crow instability of rectilinear trailing vortices (see e.g. [276]).

[8] Quantitative comparison has not been attempted, since in that case one needs to know the core size a. As we have shown in §10.1.2, a cannot be defined unambiguously.

Figure 10.12: (*see inserted sheet*) Single pseudo-elliptical vorton ring ($N = 96, L/2R_e = 7$): behaviour in case of the N+K-equation and a slight restriction (exaggeratedly illustrated by the sketch at bottom right). Tree views of the ring are given at each time t.

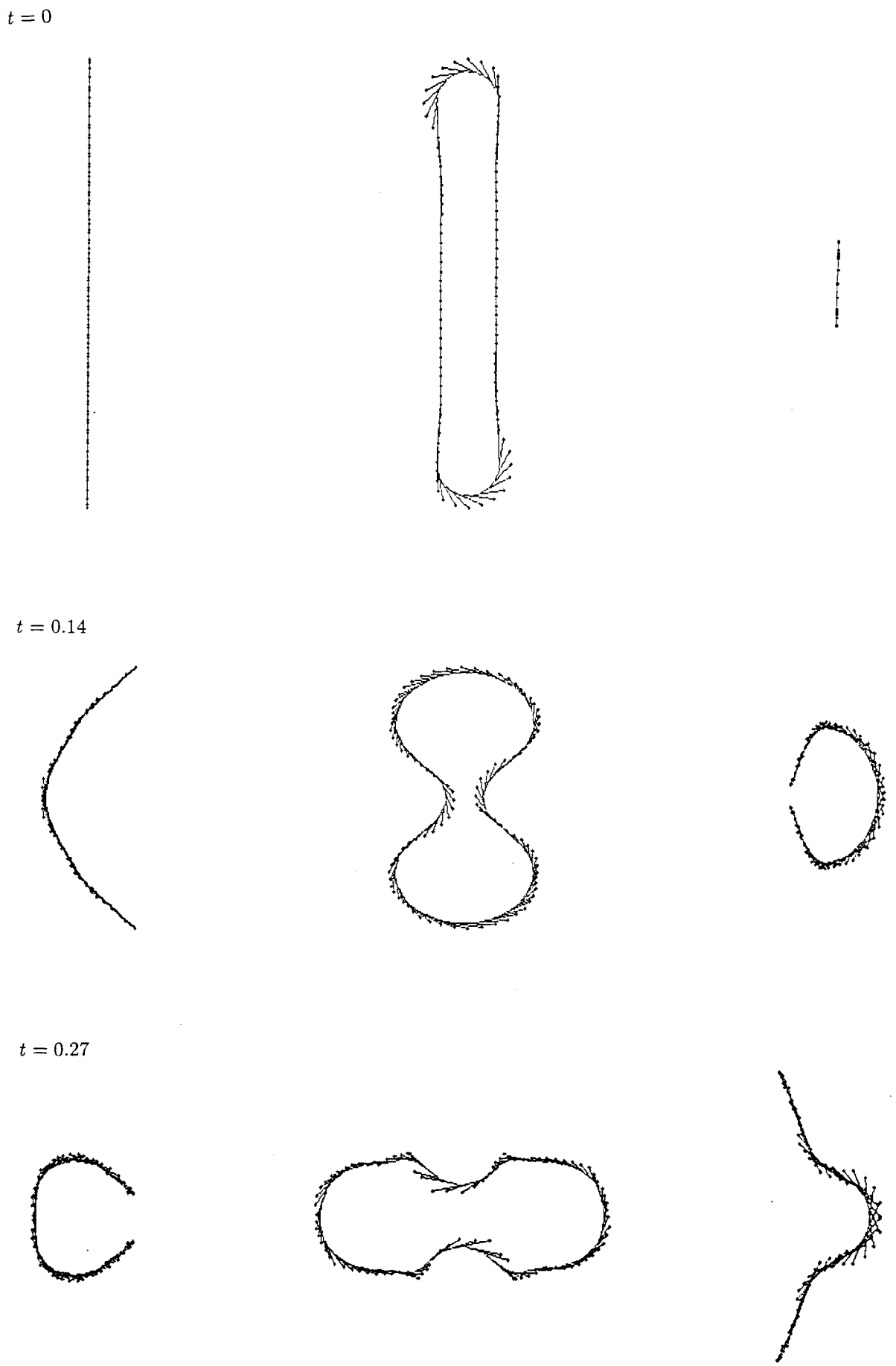

Figure 10.12

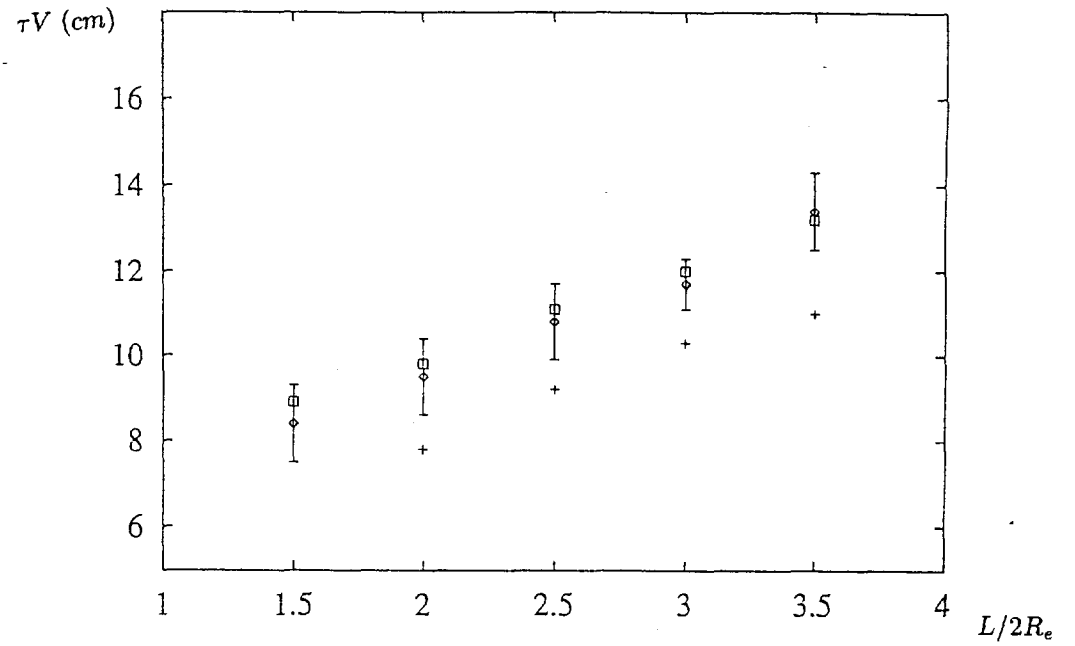

Figure 10.13: Single pseudo-elliptical vorton ring ($\Gamma = 225$): comparison of τV (τ is the duration of one complete oscillation; V is the average ring velocity) vs. axis ratio $L/2R_e$. Comparison between results from numerical simulations ((□) N-equation ($N = 10$) and (+) N+K-equation ($N = 8$)) and from experiment (◇) (error bars have been provided).

Comparing the time development of the cores in figs. 10.17 and 10.18 with figs. 10.15 and 10.16, we observe that at t^*, defined above, the cores become deformed and asymmetrical. This is also illustrated by fig.10.19(a) in which the development in time of the non-dimensional core radius $\tilde{a}$ (defined in 10.1) in plane B (see fig.10.14) has been illustrated. The core is again derived from the velocity distribution around the centre line of the vorton ring (see fig.10.19(b)), but as is evident in the figure, the radius at the front of the ring (i.e. where the rings touch each other) finally becomes smaller, while the radius at the back starts to increase.

In fig.10.20 the development of circulation Γ of each ring is presented as calculated from integration along the two different curves A and B indicated in fig.10.14. Comparing with figs. 10.15 and 10.16, we conclude that conservation of circulation starts to be violated at t^*. However, the direction of the deviation of Γ depends on the curve used in the calculation. As mentioned in §10.3.2, decrease of Γ has also been found in experimental and numerical experiments in literature, where it can be attributed to viscosity. For our simulation, this explanation is not workable. Apparently, the calculation of Γ by means of the curves A and B is no longer allowed the moment the distance between the core centers has decreased beyond a certain value.

As the developments of R, d, and Γ are now known, we can check Dyson's results for the rate of change of R, given in §A.2 of the Interlude. In fig.10.21 the relation between circulation Γ divided by distance d is plotted against the rate of change of radius R. We conclude that for

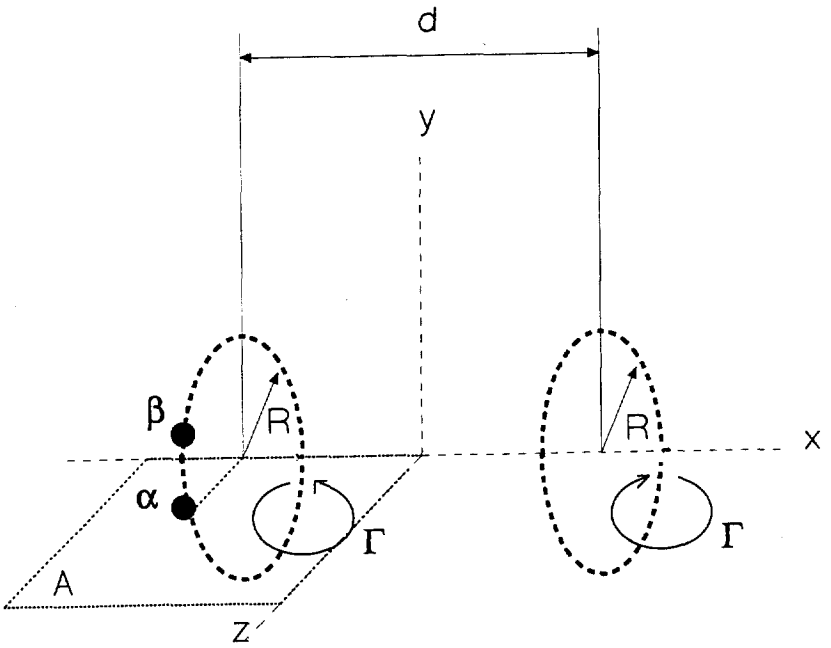

Figure 10.14: Initial configuration of two head-on colliding vortex rings (ring/ring interaction). The dots indicate vorton locations. Plane B (curve B) is plane A (curve A) rotated around the the x-axis, such that it intersects the vorton ring at the location between vortons α and β.

a certain period of time the linear relationship, as found by Dyson, exists. After t^* the rings stop behaving as Kelvin-rings.

Regarding the conservation of the motion-invariants mentioned in §9.3.1, one may recognize that due to the symmetry of the configuration, expression (9.5) for linear momentum, expression (9.8) for angular momentum, and expression (9.16) for helicity are always zero. This is indeed confirmed by the simulation results, though some very small scattering around the zero line is present. In fig.10.22 the development of interaction-energy E_i, according to (9.10), and of self-energy E_0, according to (9.14), are shown. We observe that conservation of E_i and E_0 is almost immediately violated. Furthermore, both curves show opposite trends.

In the second simulation of this section, we have tried to reproduce the phenomenon of the formation of smaller vortex rings on the circumference of the two initial rings, as observed by Lim [128] and discussed in §10.3.2. As the simulation presented above did not lead to sinusoidal disturbances by itself, we decided to introduce a slight axial sinusoidal disturbance to the rings. The simulation was done with standard rings consisting of $N = 72$ vortons each. The wave mode number was chosen $n = 12$ (compare (10.4)), and initial separation was $2R$. In fig.10.23 the simulation result is shown by means of the vorton locations. Initially, when the rings are separated at relatively large distances, the imposed wave mode is stable and the disturbance will be damped. However, when the rings approach each other, their velocities decrease and the wave mode becomes unstable at the moment when the non-dimensional velocity $\tilde{V}$ reaches the critical value for this specific mode (compare with fig.10.5). In the next phase, reconnection takes place and small rings are formed. Note, however, that these rings seem to be still connected to each other by vortons lying in between them.

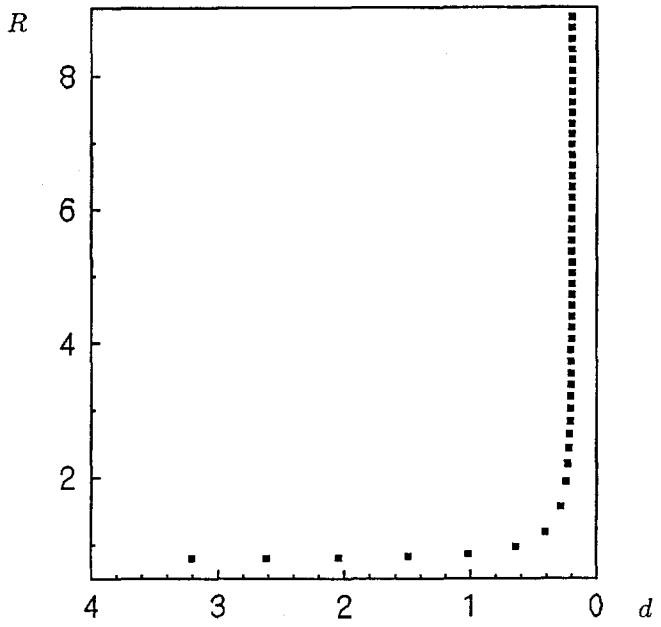

Figure 10.15: Head-on collision of two standard vorton rings ($N = 36$), initially separated $d = 4R$: radius R vs. distance d.

Finally, we have investigated the effects of vorton division (see §9.4) on this configuration. At least one reason to apply vorton division in this case can be obtained from the simultation results presented above. In fig.10.18 we observe that the location of maximum vorticity, which is supposed to be the location of the core centre, starts to revert at a certain time, even though the vortons of both rings keep approaching each other as is shown by fig.10.16.

We have applied the vorton division procedure as described in §9.4. For λ we have taken the value given by Pedrizzetti [177] from his analysis of the conservation of "vortex volume" to a vorton. In §10.1.1 we found that the core size of a vorton ring (for a circular, undeformed core) is proportional to the length of the vortex tube (see (10.2)). Supposing that the vortex volume is proportional to $a^2\Delta x$ (Δx has been defined in fig.9.3), one can easily derive that λ should be $2^{\frac{2}{3}}$. Notice that this value implies that stretching of a vortex tube will cause a decrease of its core size, whereas in the absence of division the core size grows during stretching.

We have applied vorton division to the case of two standard rings ($N = 36$) initially separated 4 times their radius. In fig.10.24 we show the development of interaction-energy E_i (9.10) for three cases: no vorton division, division without updating of the vorton strengths in order to conserve circulation, and division with updating (see §9.4). We observe that our division procedure including updating is able to prevent the continuous decrease of the level of E_i as happens without division. Division without updating is seen to give unsatisfactory results in this respect.

However, the simulation of this configuration has also made clear an important drawback of vorton division. As explained in §9.4, the added vortons are positioned at locations which are linearly interpolated between the locations of the existing vortons (see fig.9.3(b)). In case of rings this means a (slight) azimuthal disturbance on their shape. From our simulations we found that after division had occured several times, an azimuthal disturbance started to grow

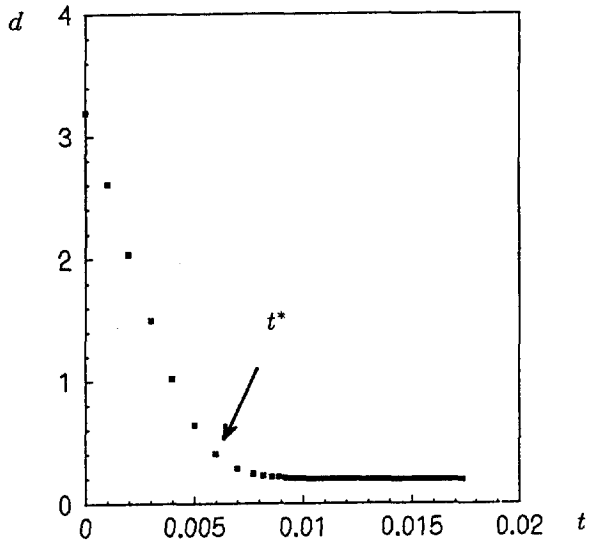

Figure 10.16: Head-on collision of two standard vorton rings ($N = 36$) initially separated $d = 4R$: distance d vs. time t.

on the rings and the configuration became unstable. The wave number of this unstable mode appeared equal to the initial number of vortons, from which we conclude that the instability was not due to physical effects.

10.4 Oblique Interaction of Two Vorton Rings

10.4.1 Introduction

In §A.1 of the Interlude the experimental observation of the reconnection and subsequent oscillation of two obliquely inclined vortex rings by Wood [285] (1901) and by Northrup [166] (1911) were presented. The configuration they studied is in essence the one sketched in fig.10.25.

This configuration is not only challenging for experimentalists and for testing numerical codes, but is also of considerable interest as it is one of the most elementary configurations in which interaction and reconnection of vortex tubes can be studied in isolation, i.e. without other disturbing influences [9]. As already indicated in fig.e of the Interlude, this reconnection is generally supposed to be a competition between vortex stretching and smoothing by viscous stresses. The adjacent edges of the rings undergo severe strain and axial flow arises along the cores. At the same time, severe core deformation takes place.

Obviously, this process is very complicated. Only numerical simulations have enabled fluid dynamicists to get some more insight into several details of the actual phenomena, but in our opinion a really complete picture of reconnection, and its understanding, is still lacking.

[9] Another useful configuration in this respect may be the (pseudo-)elliptical vortex ring. However, in §10.2 we have seen that pseudo-elliptical vorton rings do not show the expected reconnection behaviour.

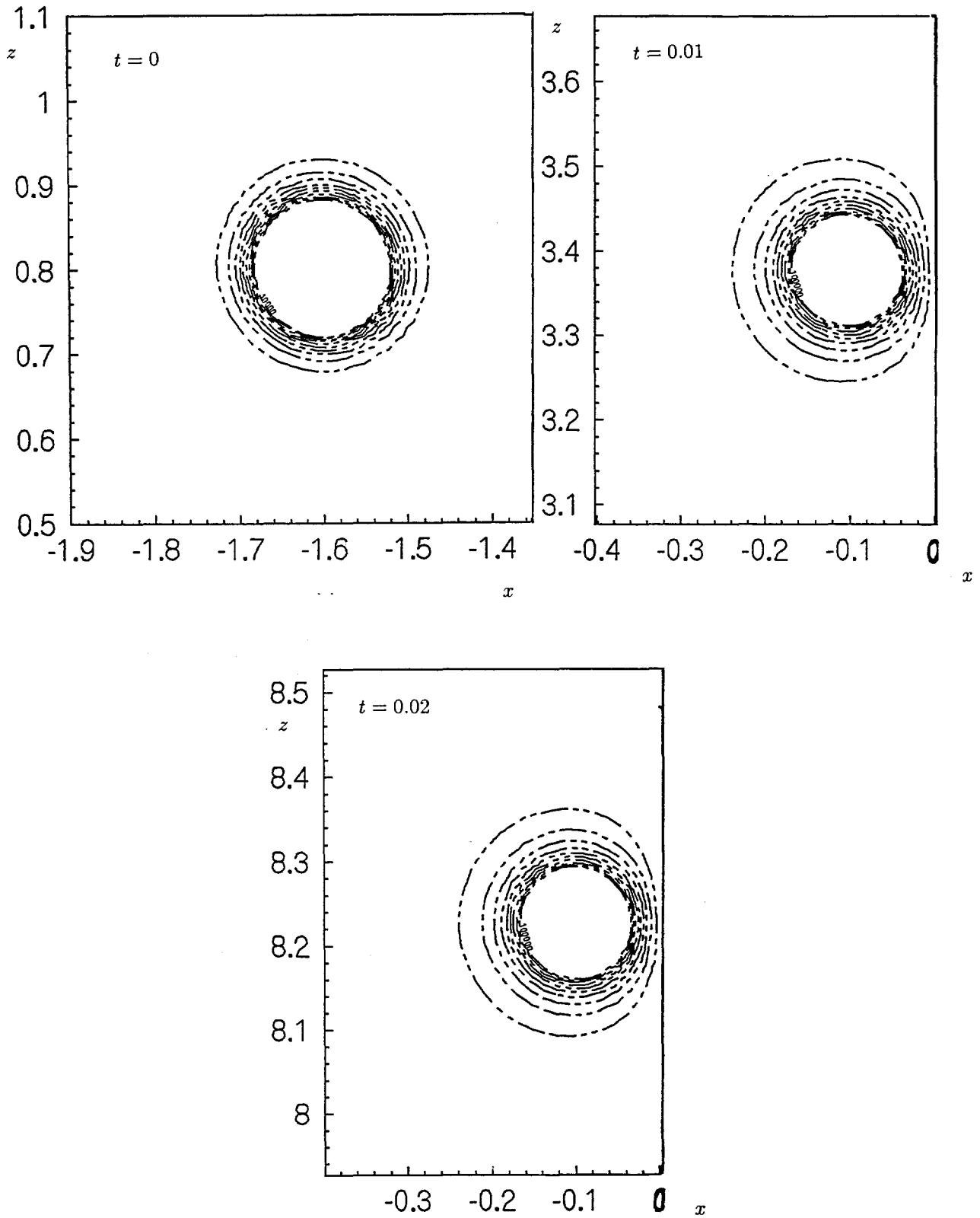

Figure 10.17: Head-on collision of two standard vorton rings ($N = 36$) initially separated $d = 4R$: deformation of the cores by means of contour lines of $|\ \bar{\mathbf{w}}\ |$ in plane A (see fig.10.14). t is time. Only the cross-section of the left ring is shown.

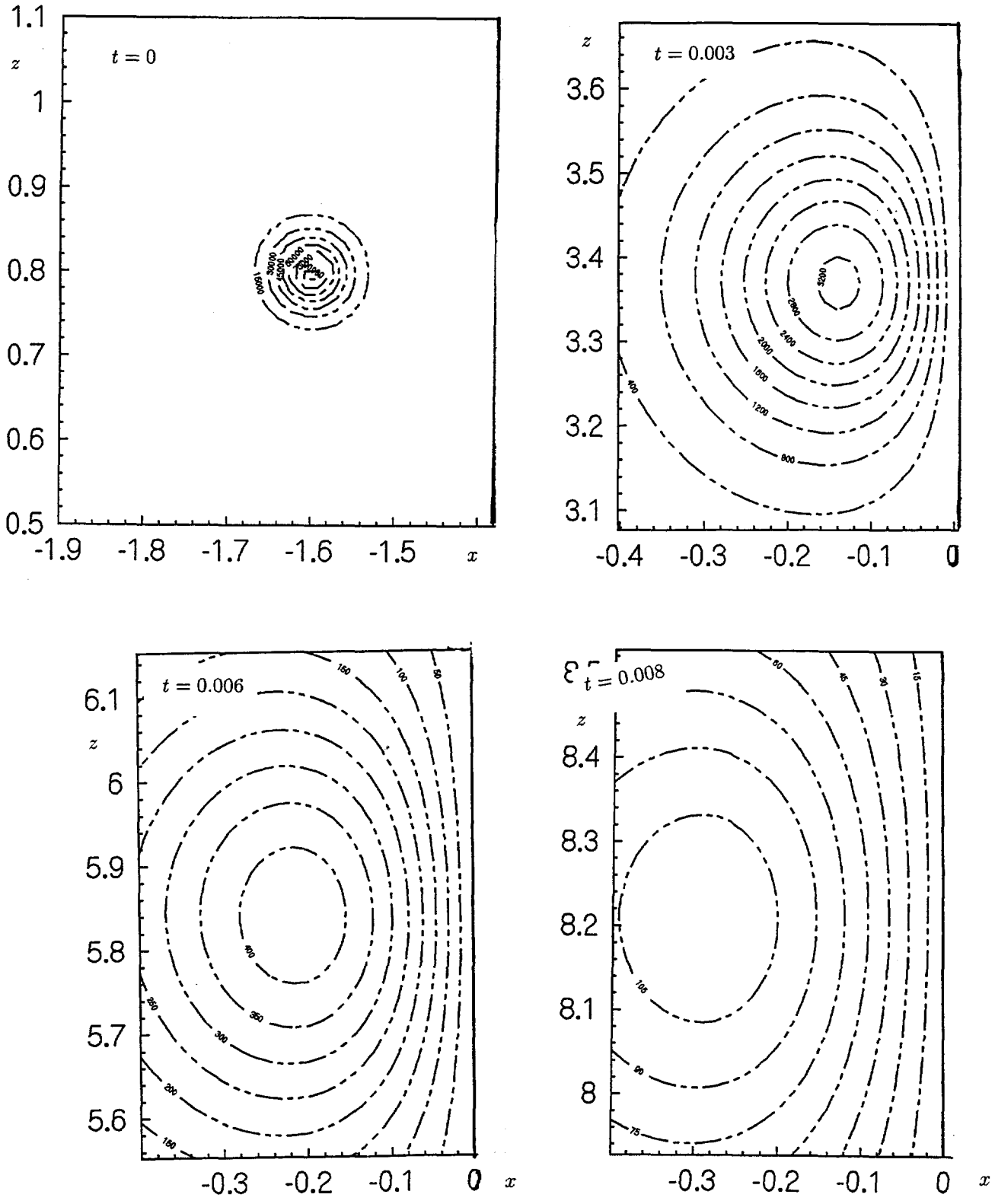

Figure 10.18: As fig.10.17, for plane B.

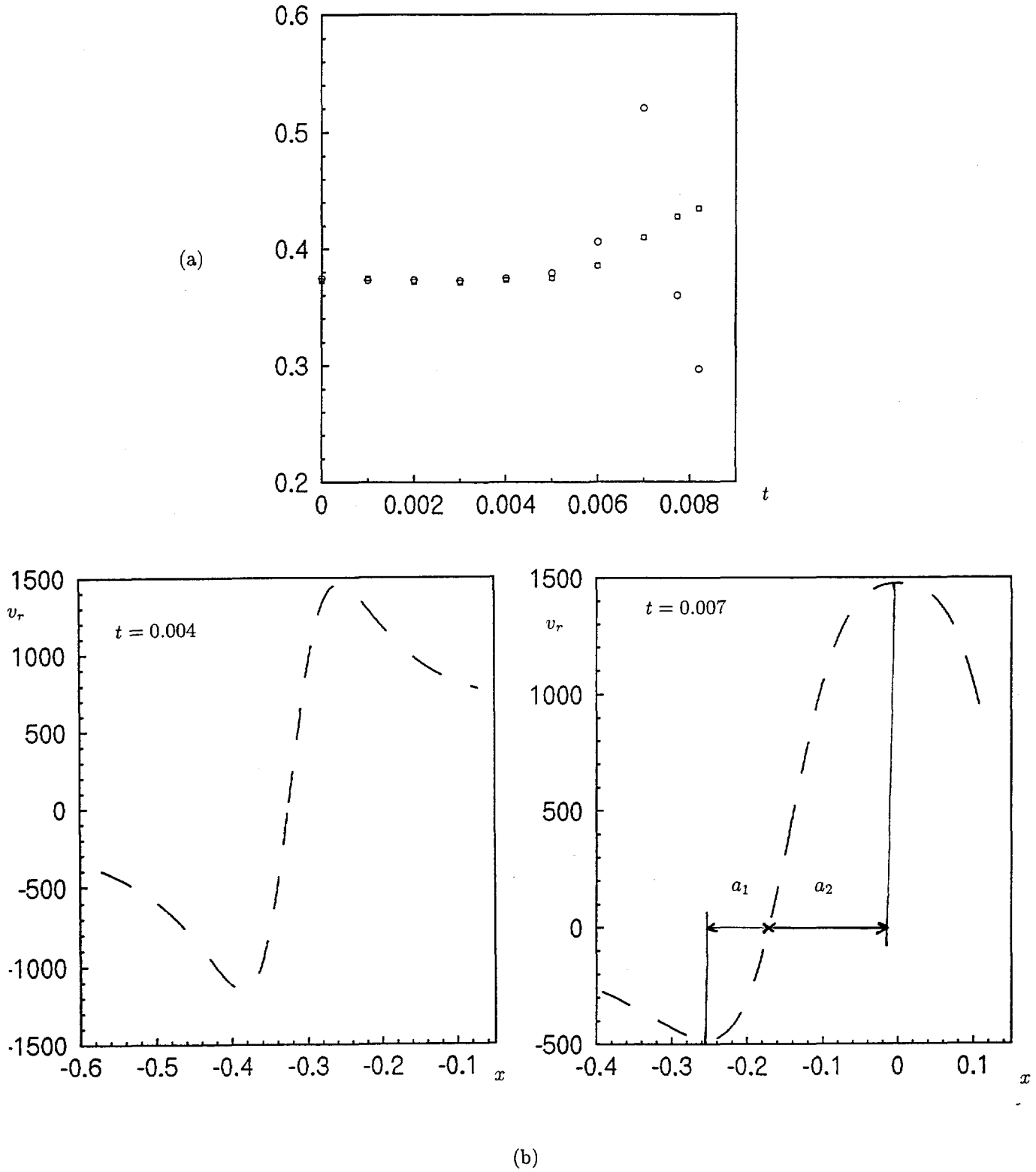

Figure 10.19: Head-on collision of two standard vorton rings ($N = 36$) initially separated $d = 4R$: (a) development of non-dimensional core radius (□) $\tilde{a}_1$ and (o) $\tilde{a}_2$ as derived from (b) the velocity distribution in plane B (see fig.10.14) (*left*: before and *right*: after core deformation). Compare fig.10.2. t is time.

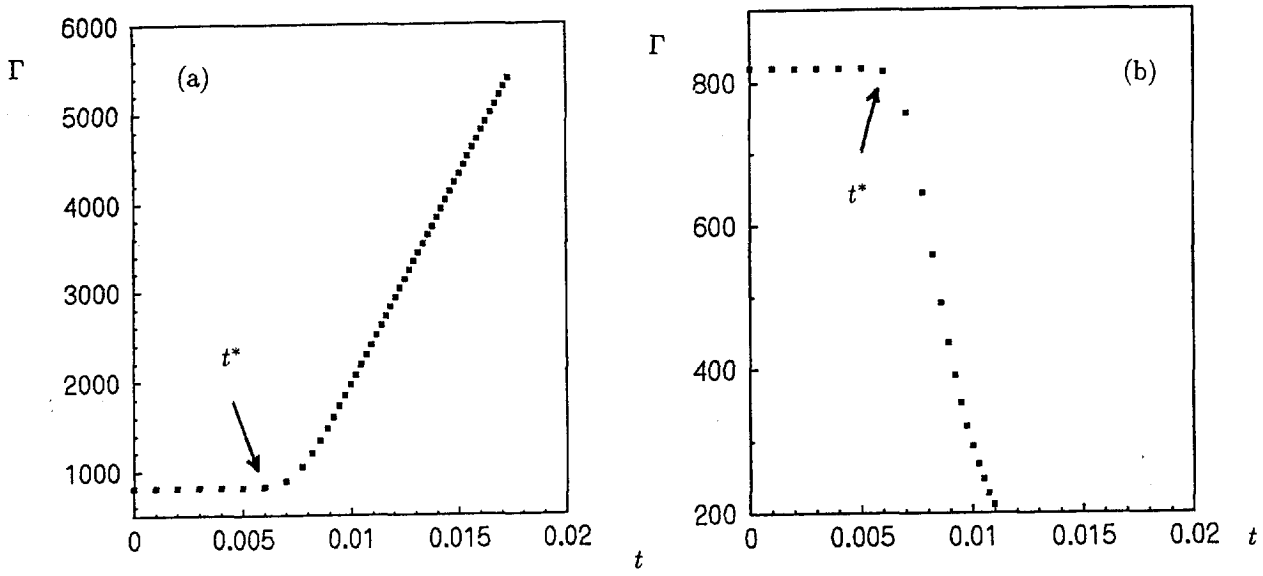

Figure 10.20: Head-on collision of two standard vorton rings ($N = 36$) initially separated $d = 4R$: circulation Γ vs. time t: Γ is calculated along (a) curve A and (b) curve B (see fig.10.14).

10.4.2 Recent Results from Literature

Only more than 60 years after Northrup, experimental work on the oblique interaction of vortex rings was taken up again, both in water and air. The experiments by Fohl & Turner and Oshima & Asaka (see [102] for references) have shown that the initial Reynolds number ($\mathrm{Re} = \Gamma/\nu$) and the angle θ of the rings with the horizontal (see fig.10.26) determine the interaction process. The latter authors have shown that three regimes of interaction can be observed, depending on the value of Re; see fig.10.26. For Re = 230-300, the two rings reconnect and merge into one elliptically shaped ring; after that this ring remains oscillating (stage A in fig.10.26). For Re = 300-420, after the reconnection (stage A) the elliptical ring eventually splits up again into two rings (stage B). For still higher values of Re, the two rings, formed after splitting, reconnect again (stage C).

Recently, extensive experiments on this vortex ring interaction have been performed by Schatzle [208] and Izutsu & Oshima [93] (see also [171]).

The experiment by Izutsu & Oshima (IO) will be discussed here in some detail, since their results will be used to evaluate our vorton simulations. By means of hot wires they were able to measure the velocity field on a grid containing the two interacting vortex rings in air. From these measurements they calculated the vorticity field. In this way not only quantitative data could be obtained, but also the possible errors of interpretation have been avoided which are involved in the common method of visualizing vortex structures by means of tracer particles. Namely, the spatial pattern of these passive scalars does not faithfully represent the vorticity field, since a scalar only undergoes convection and does not undergo deformation. Therefore, at the locations of high vortex stretching, a depletion of tracer particles will occur.

In the IO experiment, the full formation of both rings took about 7.2 *ms* after a loudspeaker was switched on to produce the rings. At that time, the radius of the vortex rings were

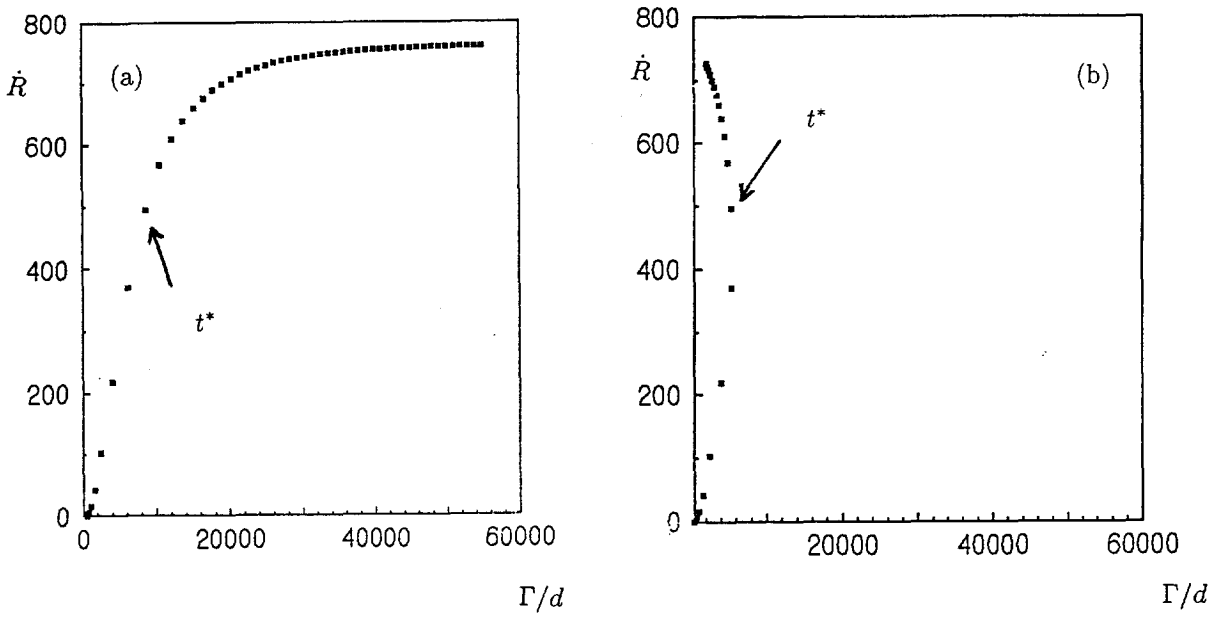

Figure 10.21: Head-on collision of two standard vorton rings ($N = 36$) initially separated $d = 4R$: Γ/d vs. rate of change of ring radius, $\dot{R}$. Γ is calculated along (a) curve A, (b) curve B (see fig.10.14).

$R = 1.16R_0$ where $R_0 = 0.8\ cm$ is the radius of the orifices. However, from their contour plots of vorticity, the radius appears to grow up to about $1.25R_0$ after the initial moment. The initial distance D between the rings' centres was taken equal to $4R_0$. The initial circulation is given as $\Gamma_0 = 813.2\ cm^2/s$ and the initial velocity V_0 of both rings as approximately 183 cm/s.

If we want to compare our numerical results with the experimental results presented by IO, we have to be sure our initial configuration resembles the initial configuration in the experiment as closely as possible. This means that we have to start the simulation with the same positions and characteristics of the rings. One check point for this correspondance is the angle of inclination θ of the rings during the early stage of the interaction. This angle is based on the locations of the core centers in the $x - y$ plane. IO mention $\theta = 86.3°$ at $t = 10\ ms$ and $\theta = 81.3°$ at $t = 14.8\ ms$ [10].

In fig.10.27 isosurfaces of vorticity magnitude are shown as derived by IO from their measurements. We observe that for this configuration, the interaction does not evolve beyond stage A as shown in fig.10.26. Besides, the arrows indicate the presence of a weak pair of parallel vortex tubes, which have been called **threads** [11].

[10] These times are the times which have elapsed since the switching on of the loudspeaker in the experiment.

[11] In this thesis we will not speculate on the mechanism of reconnection which is exposed by these experiments or our numerical simulations. Comparison of our results with those by IO is only meant to investigate the applicability of the vorton method to this configuration. Nevertheless, we will mention shortly IO's conclusions on the reconnection process, as they have expressed it in [171]. According to IO, the actual cut-and-connect phenomenon does not take place at one location or moment, but "the cutting points dissolve gradually". The tubes of the approaching rings "consist of a number of vortex filaments ... Each filament individually cross-links one by one and moves away quickly in the direction normal to the plane of the filament because of its strong curvature". They suggest that an essential part is the bridging process, i.e. the formation of "new vorticity concentrations" which form the links of the two rings.

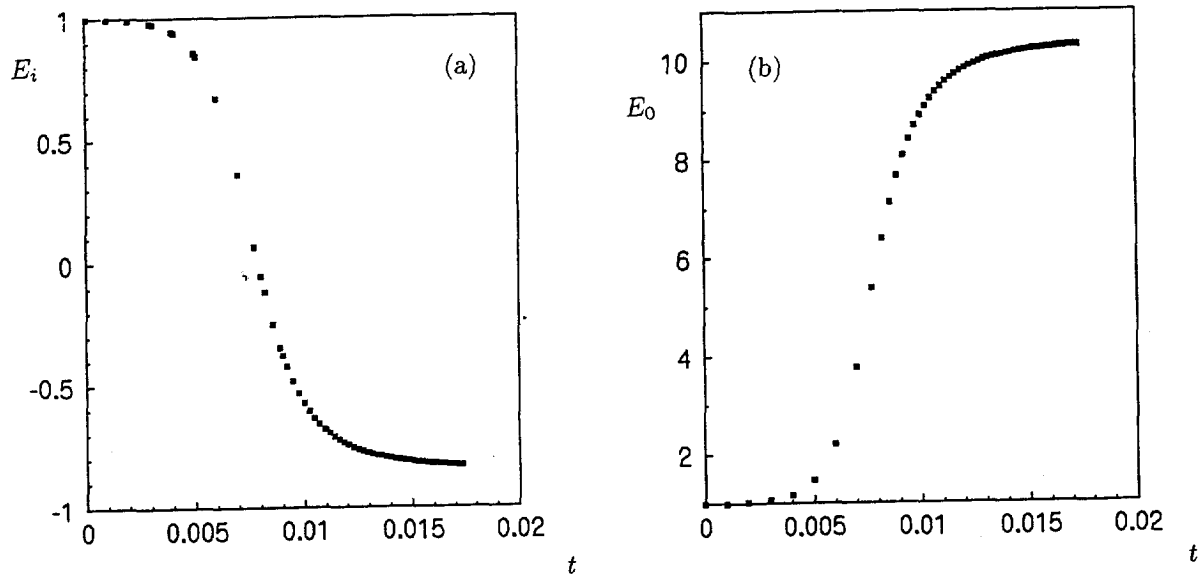

Figure 10.22: Head-on collision of two standard vorton rings ($N = 36$) initially separated $d = 4R$: the development (a) interaction-energy E_i according to (9.10), (b) self-energy E_0 according to (9.14). Both curves have been scaled with their initial value. t is time.

The configuration treated here has also been used for the investigation and calibration of several vortex methods and numerical methods. Besides, as remarked, numerical simulation is still the only way to investigate the reconnection process in more detail. Some examples of recent numerical research are presented:

- Anderson & Greengard in [9] have applied a vortex-filament method (see §7.3.1) and added a numerical scheme to simulate diffusion of vorticity. They found that the cores of the rings deformed but were not uniformly pressed against each other during the interaction at infinite Reynolds number. This, they suggest, means that the process depends on Re. They have also remarked that "perhaps the reconnection process is too subtle to admit representation by a universally valid model" and pointed at the impossibility of several Eulerian grid methods to represent the small scales that arise in the region of reconnection.

- Winckelmans [283] (also in [32]) applied both the vorton method and the soft-vorton method (see Appendix B) to a configuration in which the two rings were initially inclined at an angle $\theta = 75°$. The cores consisted of a symmetrical pattern of vorton rings centered around a central vorton ring; see fig.10.28. From his numerical results, Winckelmans concluded that the K-equation is preferable to the N-equation and N+K-equation. However, he added that the vorton method is not applicable to this configuration and cannot represent reconnection. The conservation of motion-invariants (linear momentum $\boldsymbol{P}$ as given by (9.5) and interaction-energy E_i as given by (9.10)) appeared to be severely

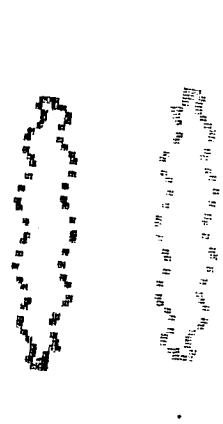

$t = 0$

$t = 0.0010$

$t = 0.0019$

$t = 0.0025$

$t = 0.0026$

Figure 10.23: Head-on collision of two vorton rings ($\Gamma = 10$, $R = 2$, $N = 72$, initial distance $d = 2R$) with initial axial sinusoidal disturbance of wave mode number $n = 12$. Dots indicate vorton locations. t is time.

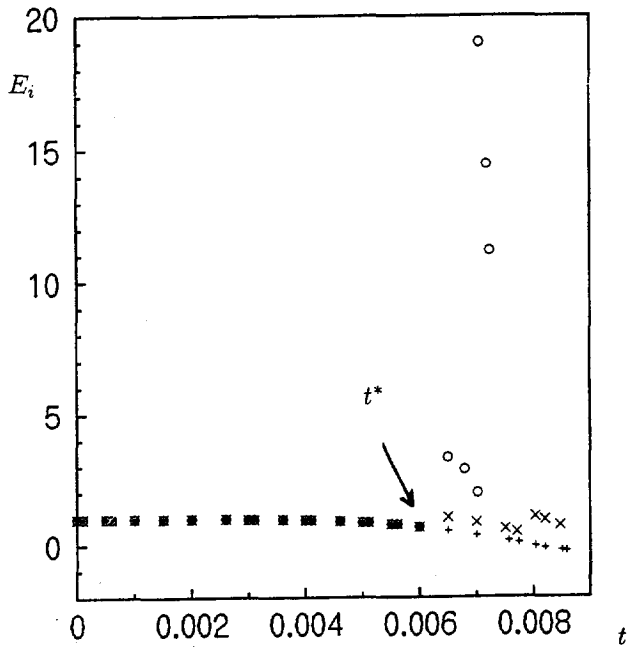

Figure 10.24: Effect of vorton division on the head-on collision of two standard vorton rings ($N = 36$) initially separated $d = 4R$: interaction-energy E_i (scaled with initial value) vs. time t in case of: (+) no vorton division, (o) vorton division without updating, (×) vorton division with updating.

violated at the moment of reconnection.

With regard to the soft-vorton method, he concluded that this vortex method *may* be useful, though no complete reconnection occurred in his simulations. He found none of the three vorton deformation equations to be preferable. The conservation of the motion-invariants mentioned was again violated. From the simulation of the same configuration by means of a soft-vorton method including a viscous diffusion term [12], Winckelmans concluded that the "physics of the problem" was well reproduced (he only investigated the K-equation). Linear momentum was not conserved, though, as he remarked himself, in unbounded viscous flows it should be. Winckelmans's simulations also showed threads.

- Kida *et al.* [103] performed extensive numerical studies of the reconnection of two viscous vortex rings, using several initial values for θ, R, D, and also for viscosity ν and core radius a. The flow was simulated solving the Navier-Stokes equation by means of a spectral method. The simulations showed the process of formation of so-called bridges and threads, as introduced earlier by Hussain and co-workers in work on the reconnection of two anti-parallel vortex tubes with a sinusoidal disturbance (see e.g. Melander & Hussain in [160]). The reconnection showed three stages (see fig.10.29 and compare with fig.e of the Interlude):

  1. core deformation and stretching during collision of the closest parts of the rings

[12] This viscous vorton scheme will not be explained in this thesis. For details we refer to Winckelmans's thesis [283].

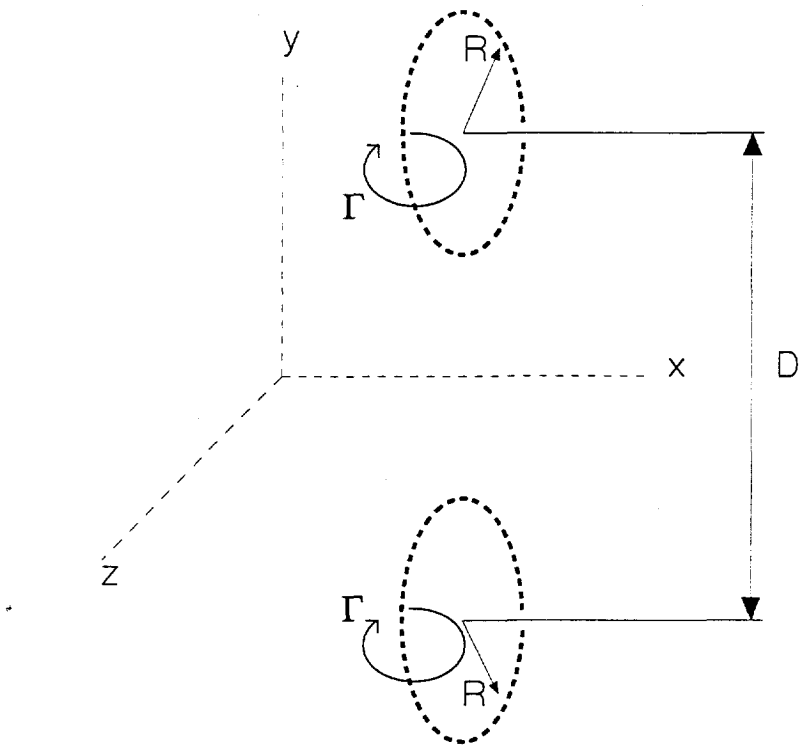

Figure 10.25: Initial configuration of the oblique interaction of two vortex rings.

(figures (a) and (b));

2. annihilation of vorticity due to diffusion and bridging, causing dramatic change in topology due to cross-linking of vortex-lines; bridging, or cross-linking, is the formation of connections between the two original rings, while unlinking is the process of annihilation of the colliding anti-parallel parts of the original vortex rings (figures (c) and (d));
3. threading, during which a remnant (unreconnected part) of the original vortex pair is sustained by stretching of the newly formed bridges (figures (d) and (e); see also the arrows in fig.10.27).

The authors also discussed the twisting of vortex-lines during reconnection. They argued that reconnection cannot occur in inviscid flows since "both topology and circulation of vortex lines do not change in time" [103, p.584].

For comparison with some of our numerical results, we show in fig.10.30 the contours of the vorticity magnitude in one of the symmetry-planes of the configuration, i.e. the $x-y$-plane of fig.10.25.

- Aref & Zawadzki (in [160]; see also [15]) used a vortex-in-cell method (see §7.3.2), with which they could simulate a slightly viscous flow. Their simulations showed weak threads during reconnection, but, unlike the results found by Kida *et al.* (see fig.10.30), these soon disappeared completely.

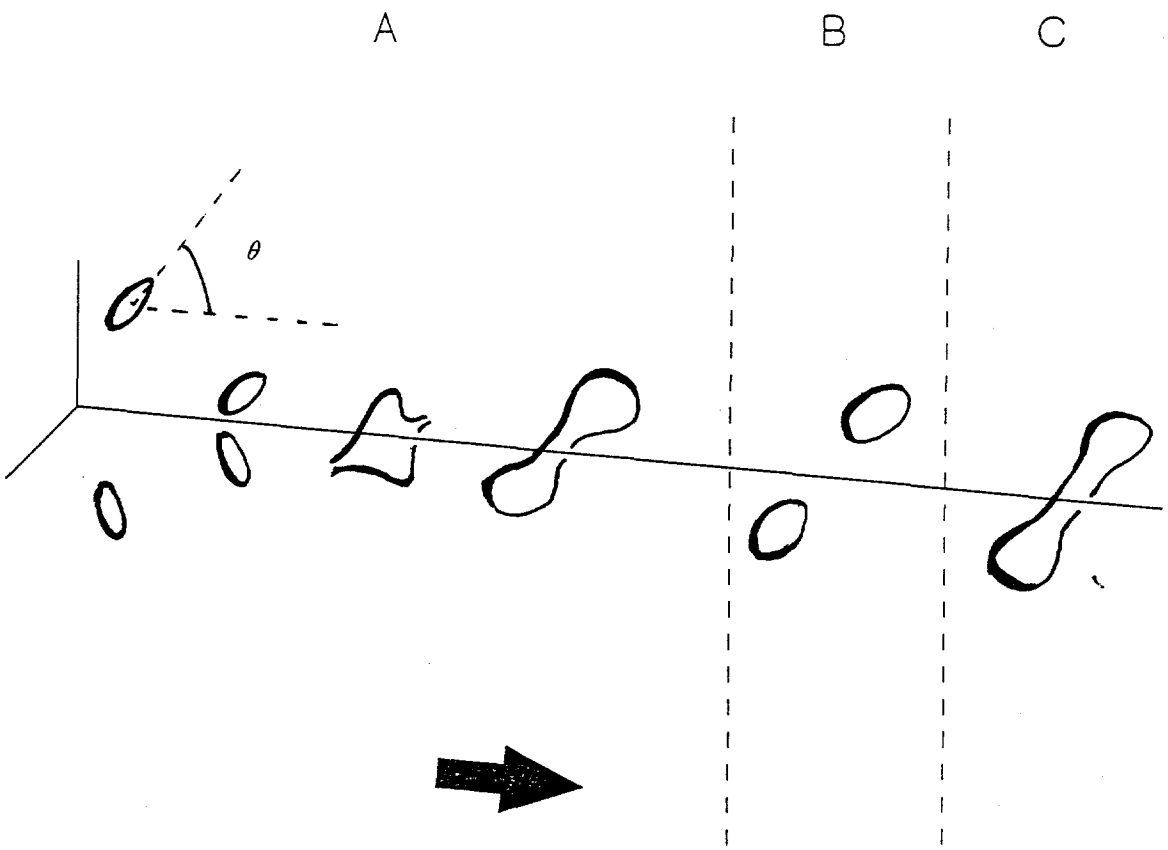

Figure 10.26: Three possible, consecutive, stages (A, B, C) in the development of the oblique interaction of two vortex rings with initial configuration as in fig.10.25 (see text). The arrow indicates time development. Compare fig.10.27.

10.4.3 Vorton Simulations

As mentioned, the numerical simulations presented in this section are compared with the experiment by Izutsu & Oshima (IO) [93]. For the initial configuration of fig.10.25 we have taken: $R = 1.25R_0 = 1.0\ cm$; $D = 4R_0 = 3.2\ cm$; $\Gamma = 820\ cm^2/s$; and for the number of vortons $N = 15$ (based on the initial ring velocity $V = 183\ cm/s$).

One has to realize that the initial positions of the vortons in the rings may be influential on the results. Initially, we will study the two configurations shown in fig.10.31. We can indicate these by the value of the ratio between the angle ϕ as indicated in fig.10.31(b) and $2\pi/N$, the initial angle between the vortons in the ring.

The simulations of both configurations have been performed for the N-, the K-, and the N+K-equation. Therefore, we have six possible combinations to investigate. In fig.10.32, the simulation results are shown by means of the vortons in the rings.

Above we mentioned the possibility to check the agreement between our numerical and IO's experimental initial condition. In all six cases of our simulation, the angle of inclination θ of 86.3° was reached at $t \approx 18.5\ ms$ (IO: 10 ms) and that of 81.3° at $t \approx 33.5\ ms$ (IO: 14.8 ms). This means that a certain amount of time has to be subtracted from the timesteps mentioned in fig.10.32 in order to get a proper comparison with the experimental results.

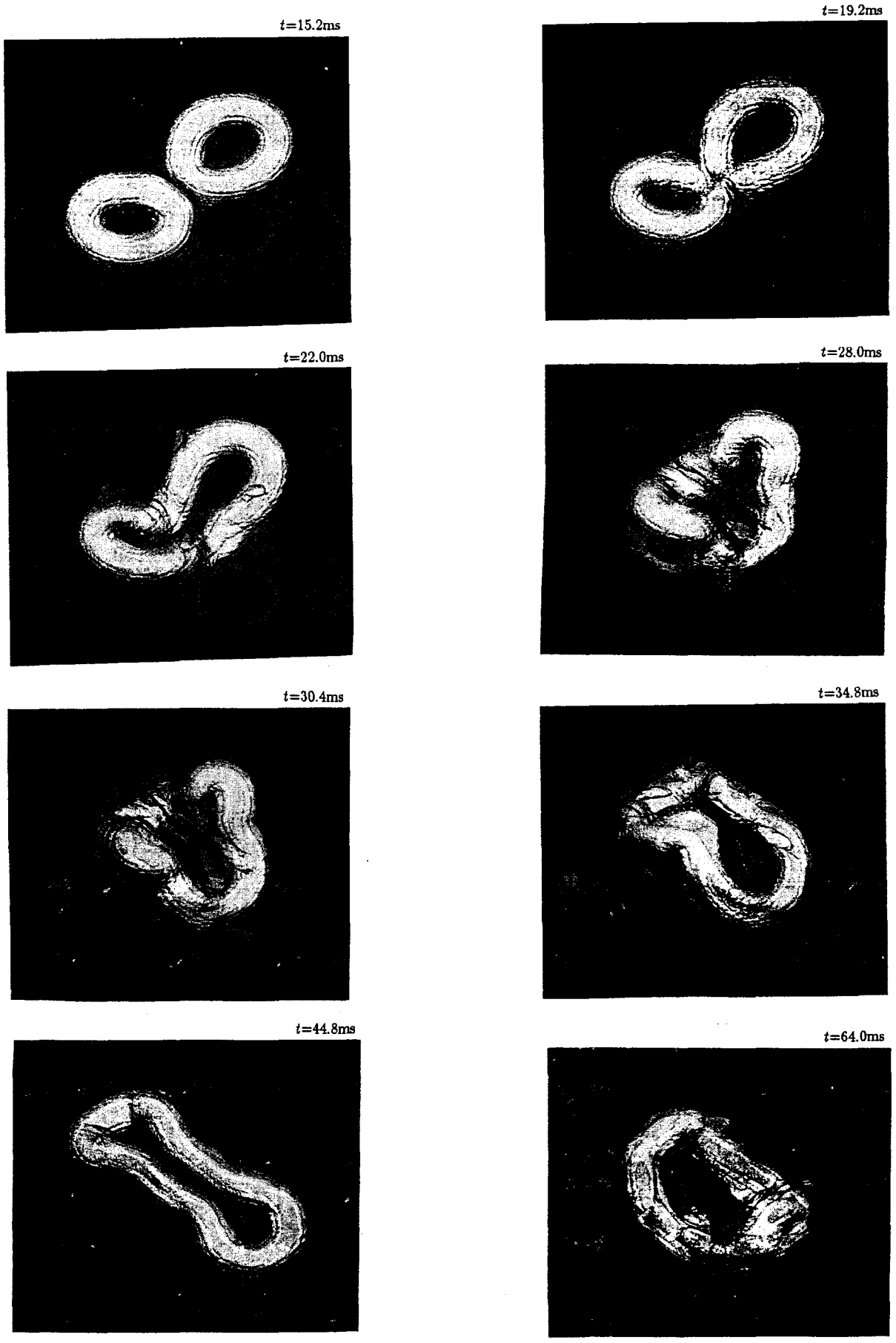

Figure 10.27: Isosurfaces of the vorticity magnitude for oblique interaction of two vortex rings. t is time. Arrow indicates threads. Experimental results from Izutsu & Oshima [93].

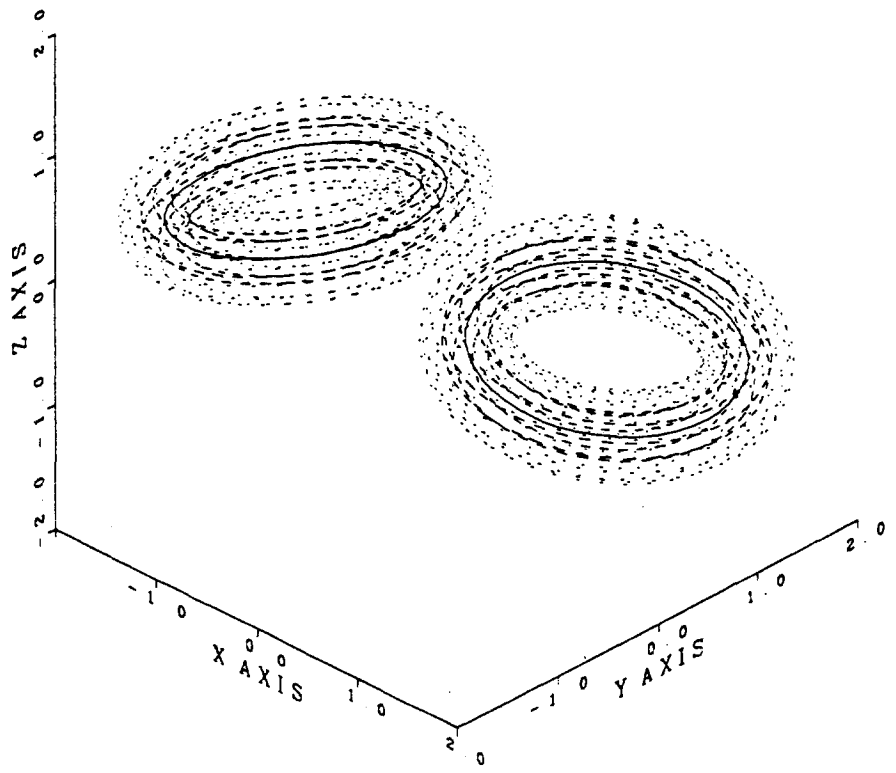

Figure 10.28: Initial configuration of a numerical simulation performed by Winckelmans. From [283].

However, we also have to conclude in our simulations the development of the configuration is slower. One possible explanation can be found in a disagreement between IO's and our definition of the inclination angle θ or of the ring velocity V. This result warns us that a quantitative comparison will be without meaning. However, below it will become clear that qualitative comparison makes sense.

From fig.10.32 we observe that the simulations of the configuration according to fig.10.31(a) show the formation of a "dipole" consisting of two anti-parallel vortons which eventually move away in a direction opposite to the movement of the reconnected vorton rings [13]. This dipole-structure does not seem to have occurred in the IO experiment. At this moment, it is unclear whether it has any relation with the threads mentioned above [14].

Though all simulations for case (i) in fig.10.32 do not agree with the IO experimental results, we observe that the alignment of the vortons is better conserved in the case of the N+K-equation than in case of the N-equation.

For the configuration of fig.10.31(b) we observe that the simulation of fig.10.32(b)(ii) (i.e. the K-equation) blew up after a short time. If we compare the other simulations with the results presented by IO as shown in fig.10.27, we observe that only the simulation of fig.10.32(c)(ii)

[13]For this reason, the "dipoles" disappear out of the pictures in fig.10.32. In passing, we have to remark that this dipole "blew up" (i.e. the strengths of both vortons grew indefinitely) when the vorton equations were completely solved for all vortons, while in the simulation of fig.10.32 advantage was taken of the symmetry of the configuration, i.e. only for one ring the equations were solved after which the new configuration was mirrored. Apparently, the behaviour of these dipoles depends strongly on the accuracy of the numerical procedure.

[14]Takaki & Hussain (see [13]) have remarked that two curved vortex tubes or ring before and after reconnection differ by a vortex ring.

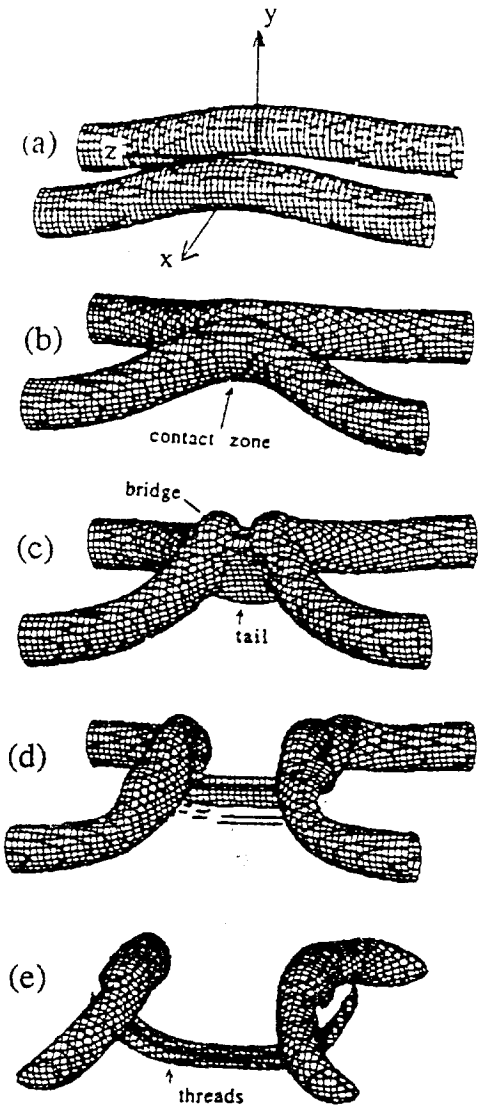

Figure 10.29: The reconnection process as proposed by Melander & Hussain in [160] (see text). Time development is from top to bottom.

(i.e. the N+K-equation) gives good agreement.

Further evidence of the better performance of the N+K-equation as compared to the N-equation is obtained from comparison of the development of some of the motion-invariants introduced in §9.3.1; see fig.10.33. Again, we remark that interaction-energy E_i and self-energy E_0 (not shown) show opposite time developments.

In the rest of this section, we will only present results related to the simulation presented in fig.10.32(c)(ii), i.e. configuration with $\phi/(2\pi/N) = 0.5$ and application of the N+K-equation. In fig.10.34 isosurfaces of $\mid \tilde{\boldsymbol{w}} \mid$ (given by (9.18)) are shown. Comparing these results with those from the numerical simulation by Kida *et al.*, shown in fig.10.30, we observe that our simulations do not show the same core deformation as in their case (in which a "tail" is formed behind the core centres). Though fig.10.34(c) suggest the presence of a thread-like object, we

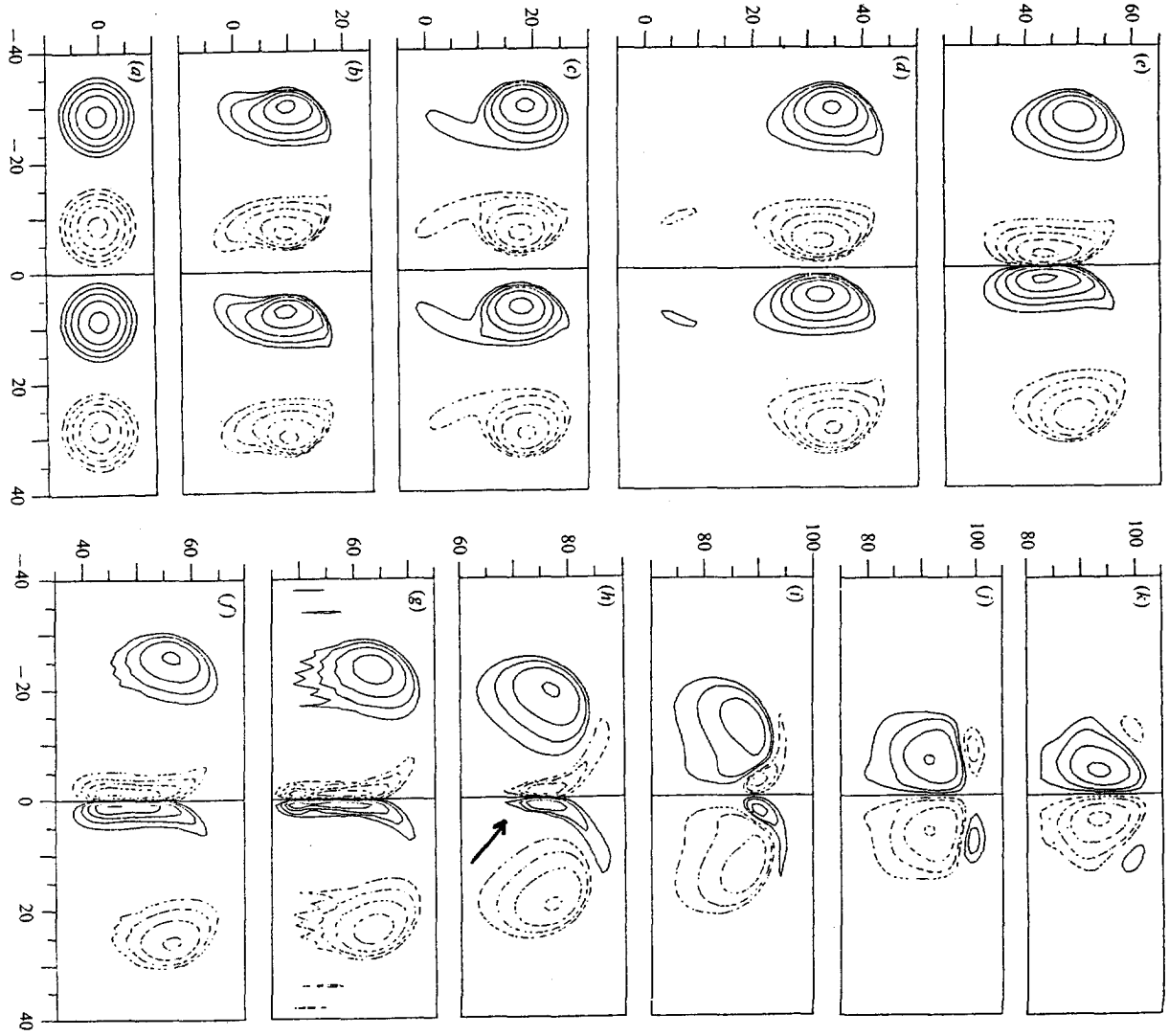

Figure 10.30: Contours of the vorticity magnitude from the numerical simulations by Kida *et al.* [103]. Cross-sections are in the $x-y$-plane (see fig.10.25). Time development is from left to right and from top to bottom. The arrow indicates the threads.

could not find a clear indication for this, as Kida *et al.* (see fig.10.30) and IO (see fig.10.27) did.

A final comparison of our numerical results and IO's experimental results (see fig.10.27) can be made by means of fig.10.35 with regard to the isosurfaces of vorticity magnitude. We observe that the development in time differs, as we had already expected from the comparison of the evolution of the inclination angle θ, discussed above. Furthermore, fig.10.35(c) shows the absence of any thread-like structure in our simulated configuration. Finally, we have to remark that whereas IO's experiment seems to have ended in complete dissolution (due to viscosity) of the last configuration shown in fig.10.27, in our simulation the configuration shown in fig.10.35(f) continued to oscillate until it finally broke down into two unlinked vorton rings.

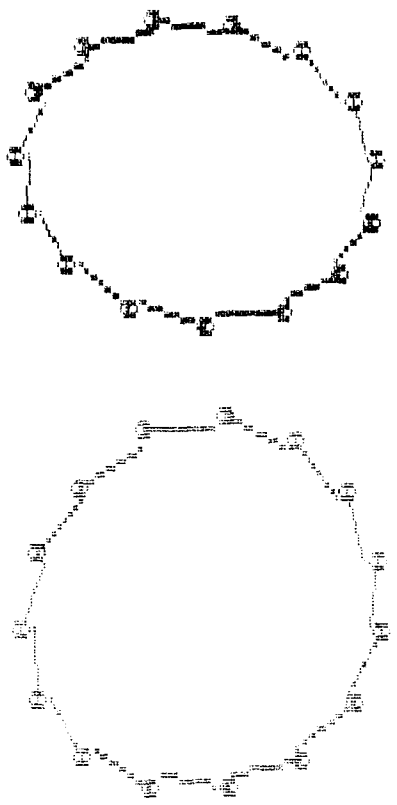

$x, t = 0.040$

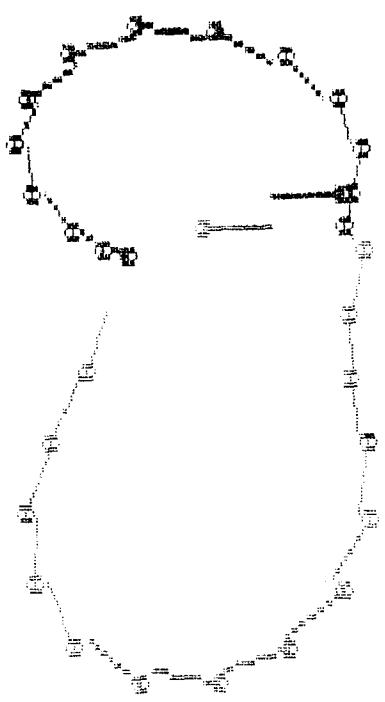

$x, t = 0.048$

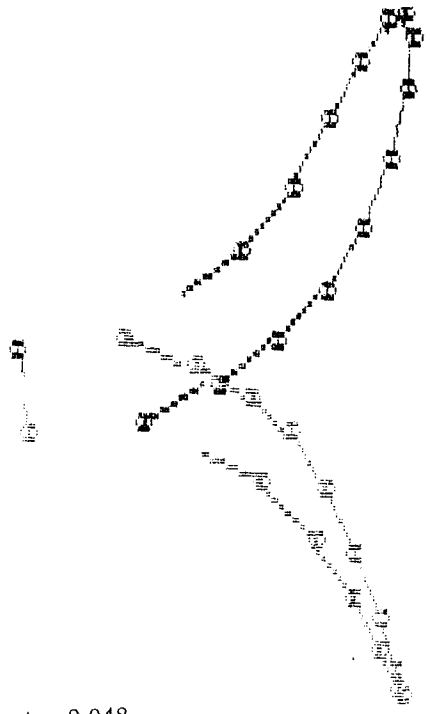

$z, t = 0.048$

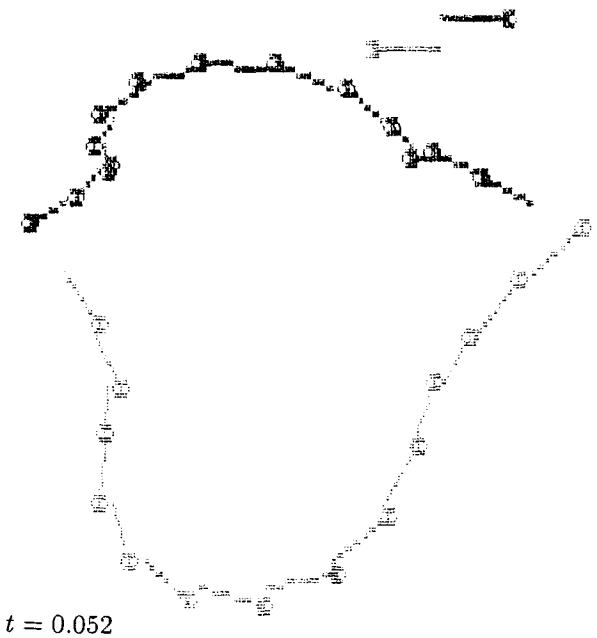

$x, t = 0.052$

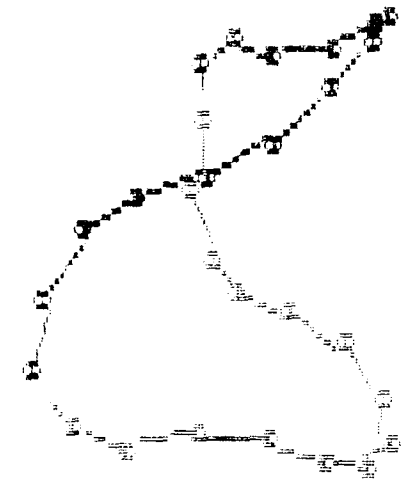

$z, t = 0.056$

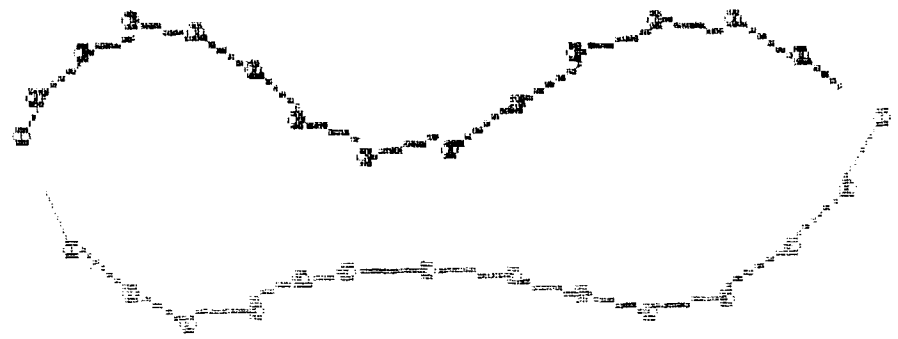

$x, t = 0.064$

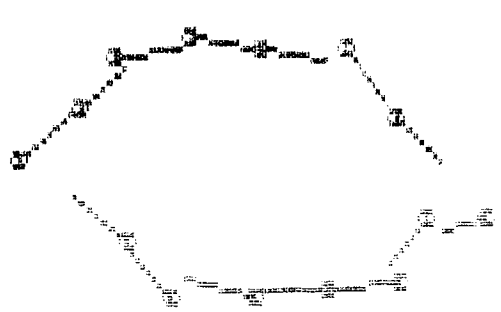

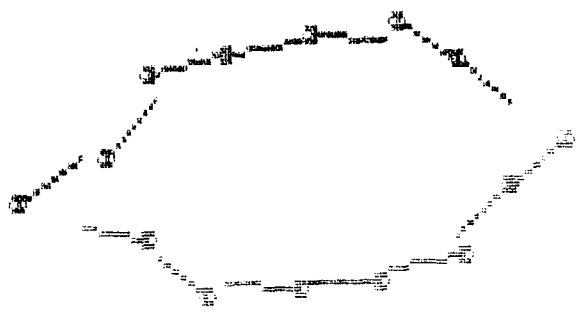

$x, t = 0.072$

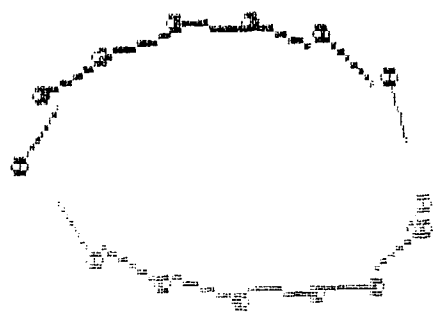

$x, t = 0.076$

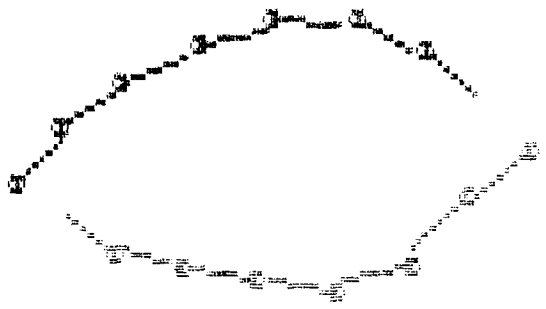

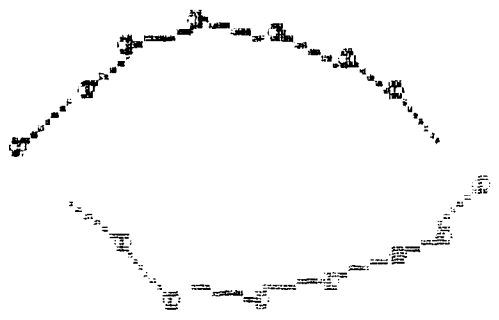

$x, t = 0.108$

Figure 10.32 (a) (i)

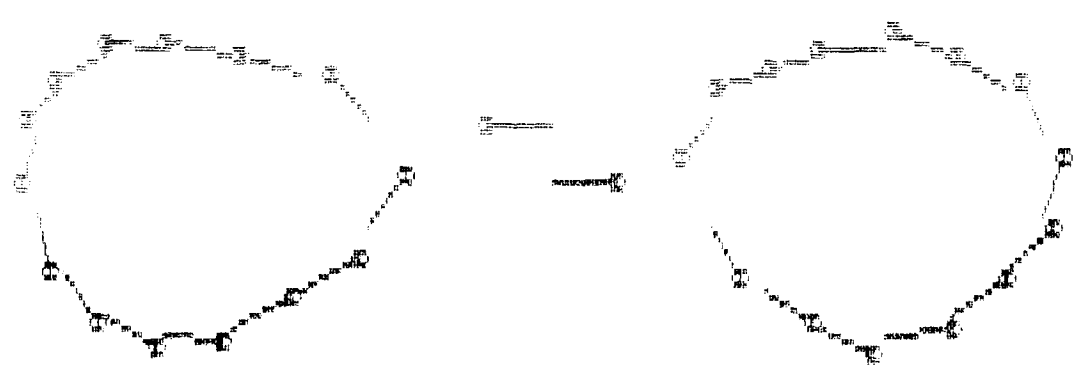

$x, t = 0.060$

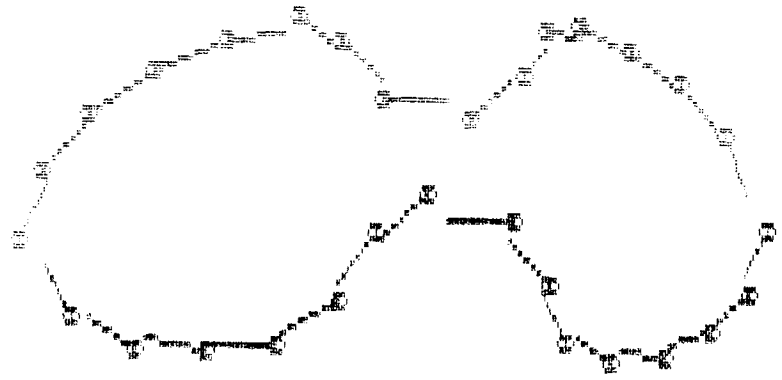

$x, t = 0.080$

$x, t = 0.105$

$x, t = 0.110$

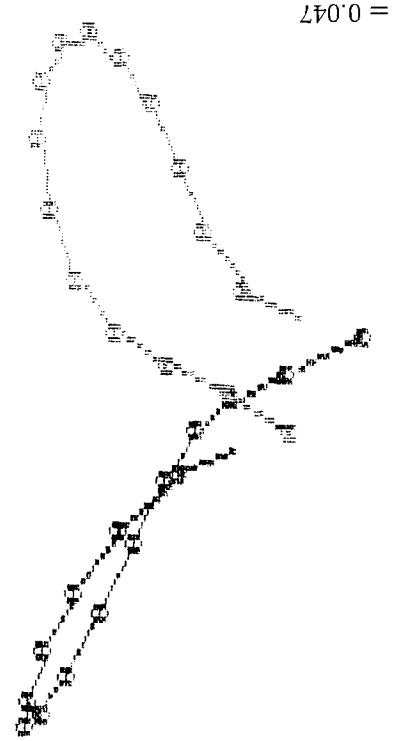

$z, t = 0.047$

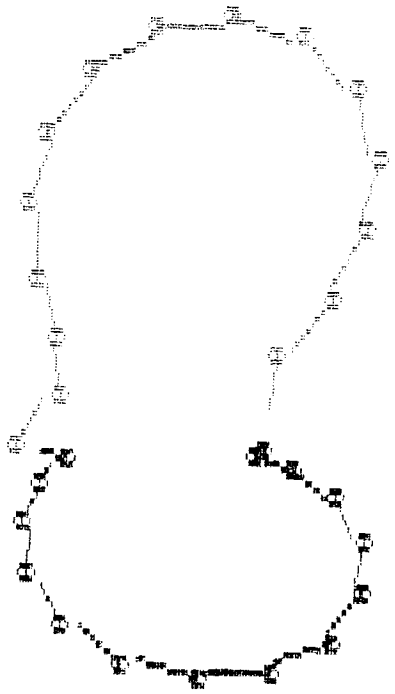

$x, t = 0.047$

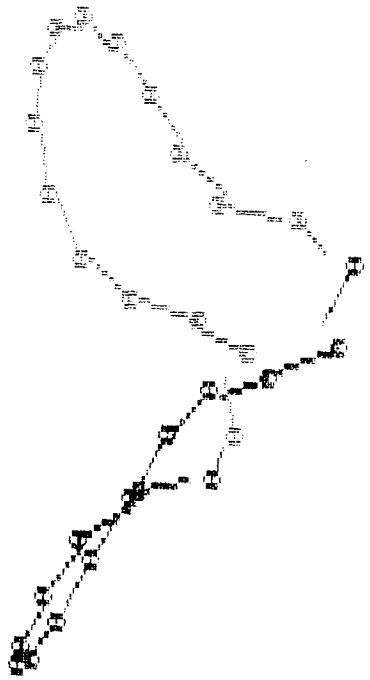

$z, t = 0.049$

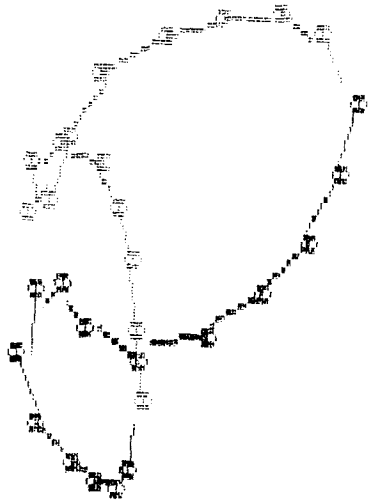

$z, t = 0.060$

Figure 10.32 (a) (ii)

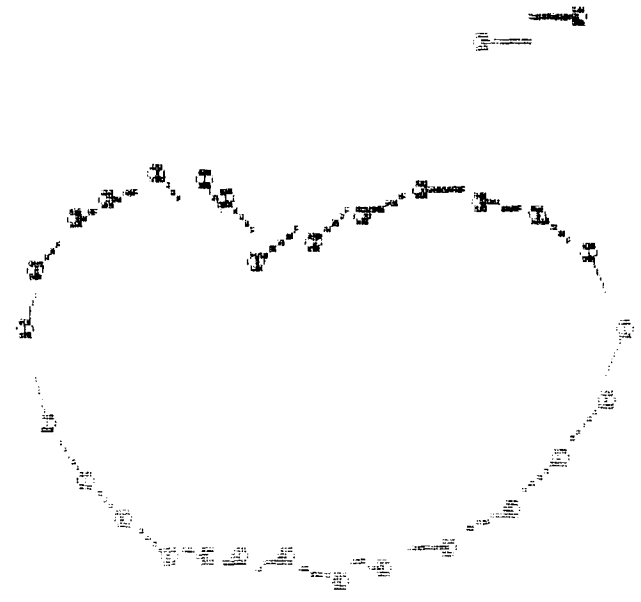

$x, t = 0.053$

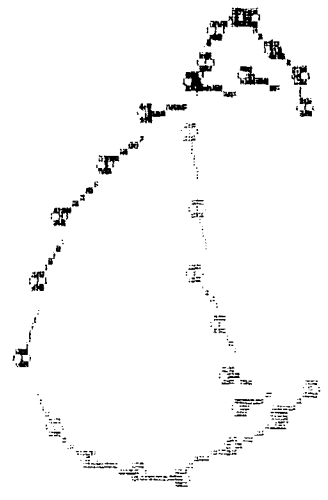

$z, t = 0.053$

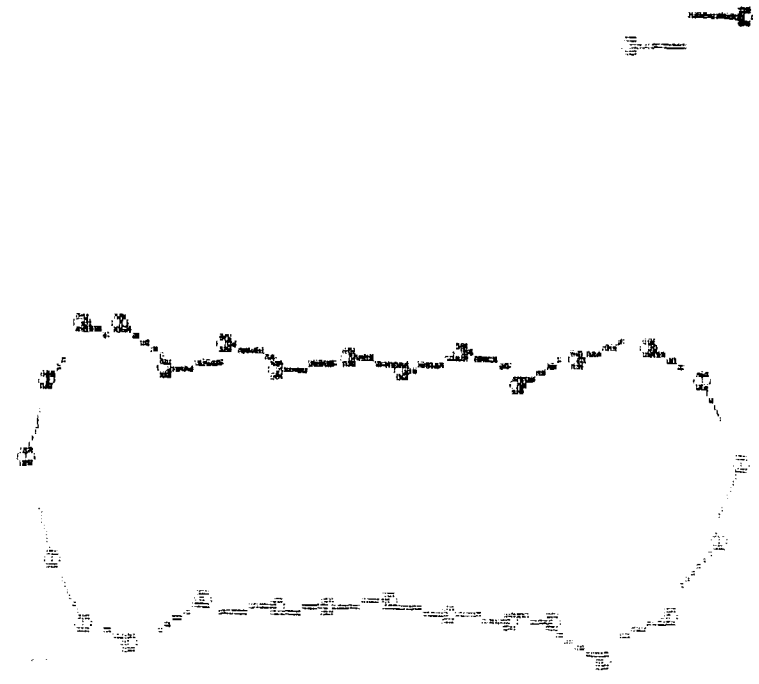

$x, t = 0.056$

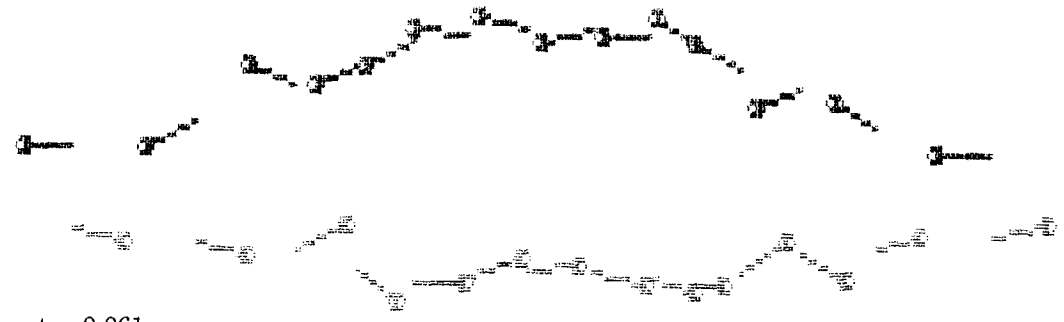

$x, t = 0.061$

$x, t = 0.077$

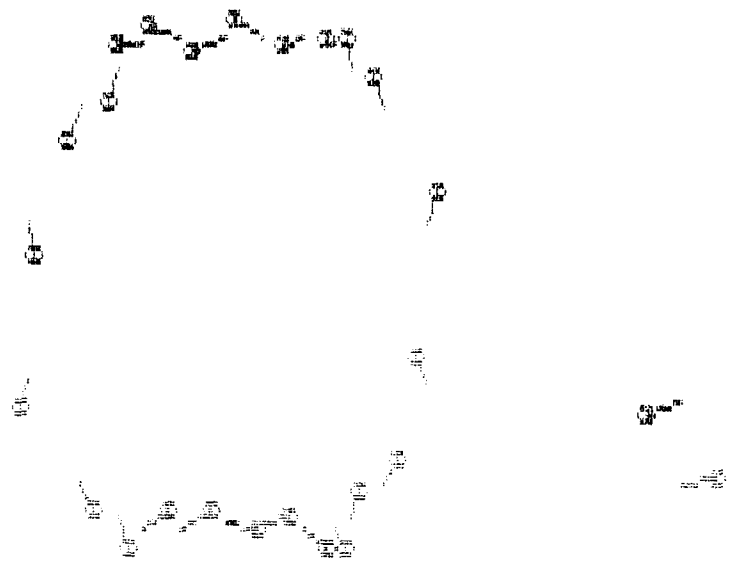

Figure 10.32 (b) (i)

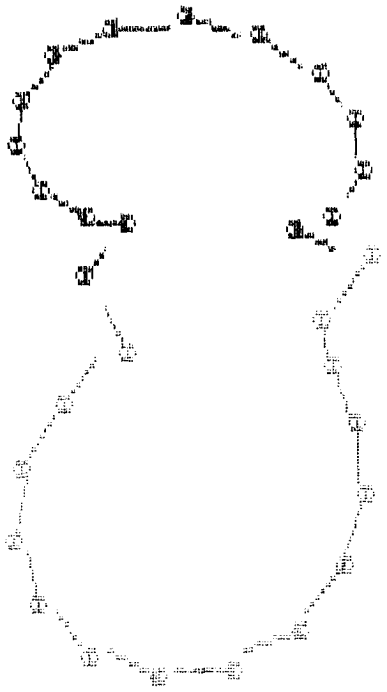

$x, t = 0.047$

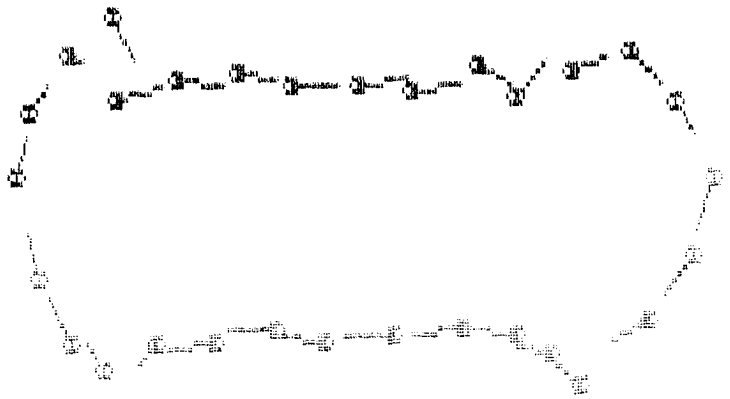

$x, t = 0.053$

$x, t = 0.057$

Figure 10.32 (b) (ii)

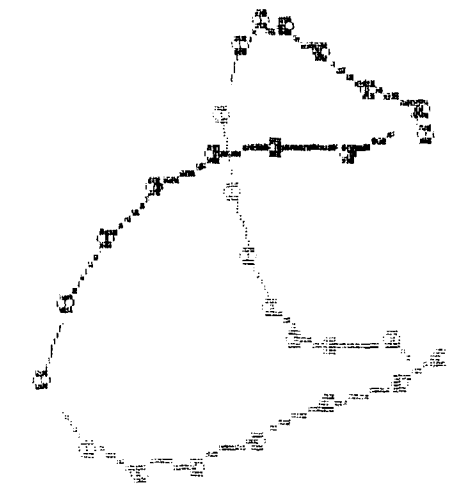

$z, t = 0.058$

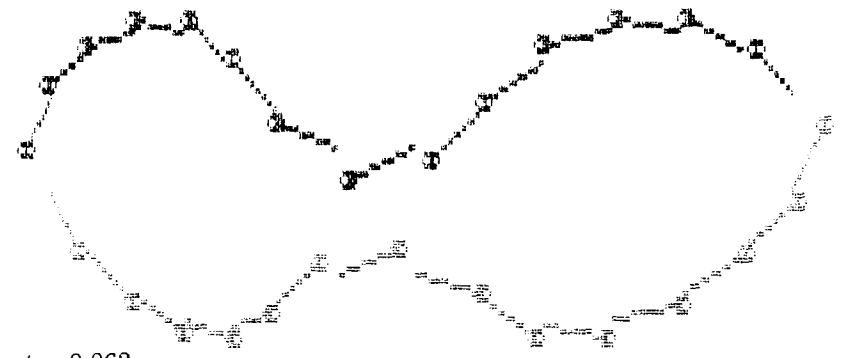

$x, t = 0.062$

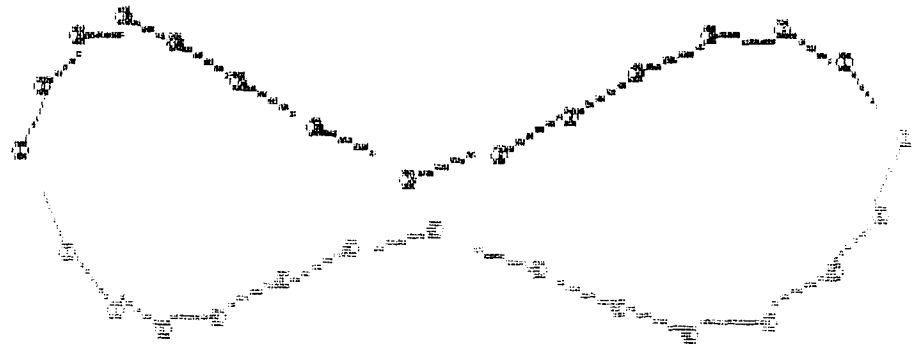

$x, t = 0.065$

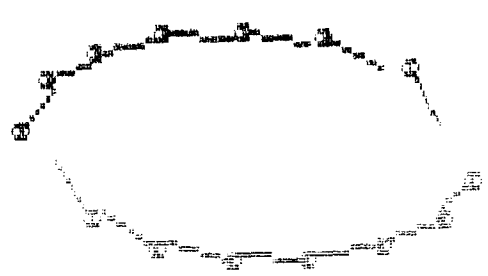

$x, t = 0.075$

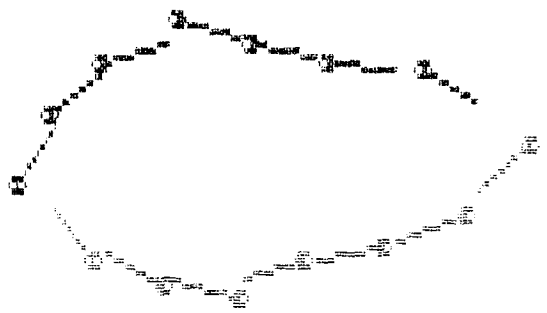

$x, t = 0.100$

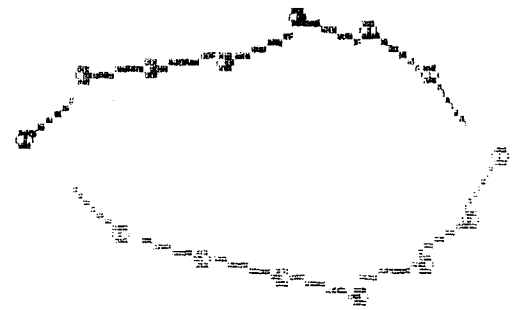

Figure 10.32 (c) (i)

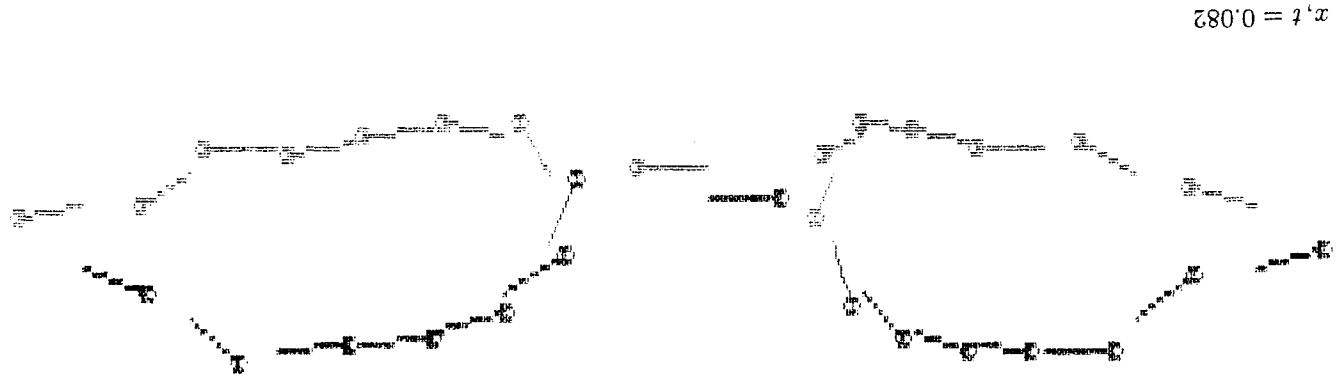

$x, t = 0.082$

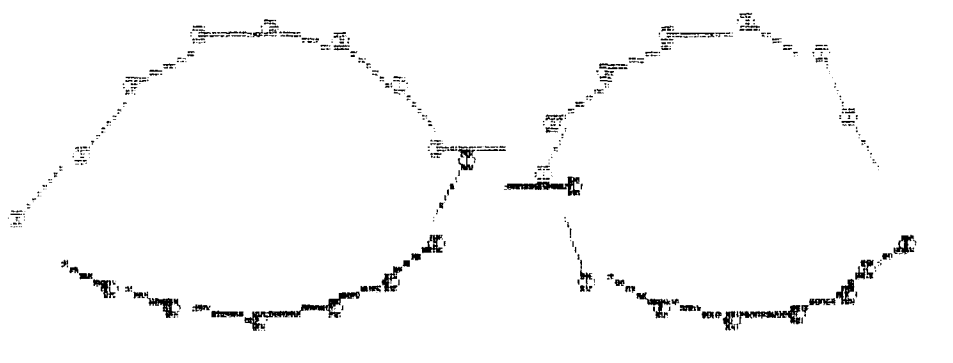

$x, t = 0.068$

$x, t = 0.170$

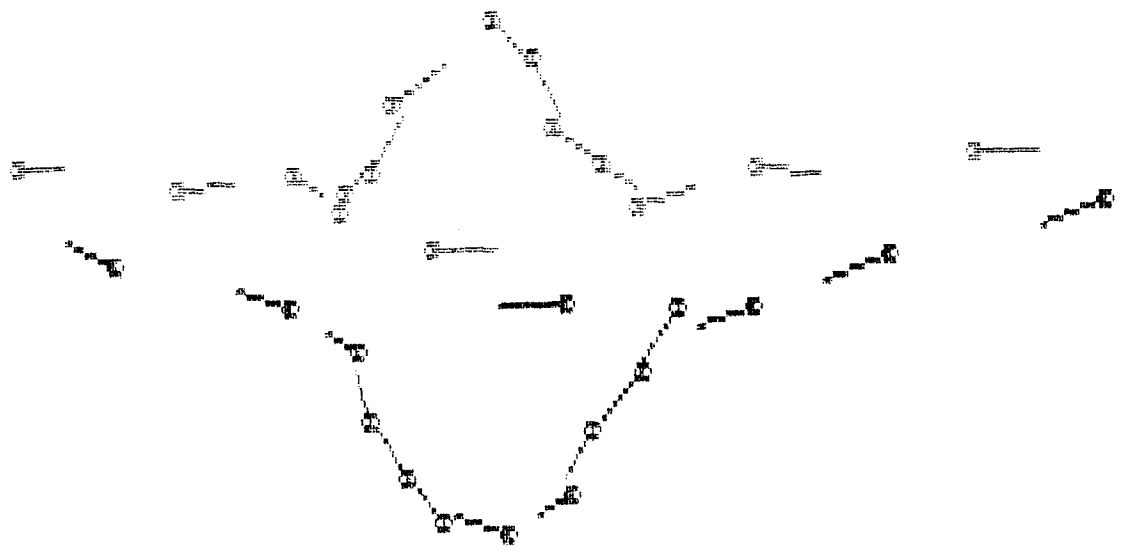

$x, t = 0.130$

Figure 10.32 (c) (ii)

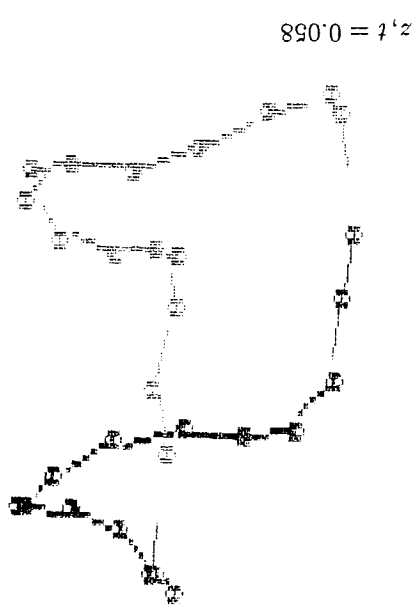

$z, t = 0.058$

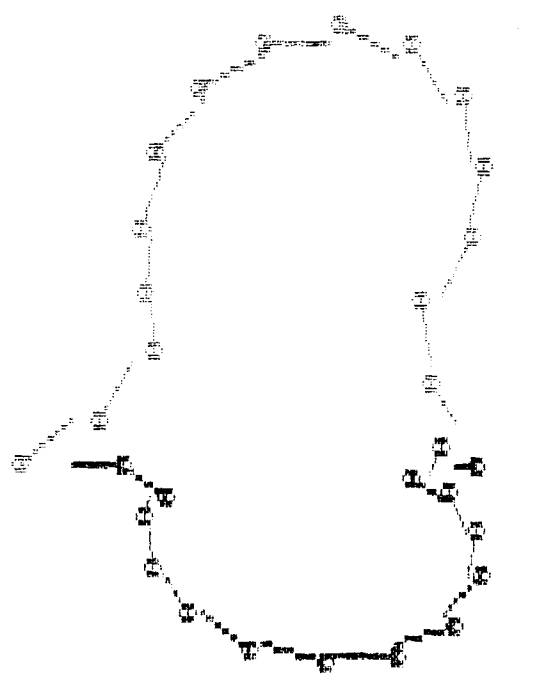

$x, t = 0.049$

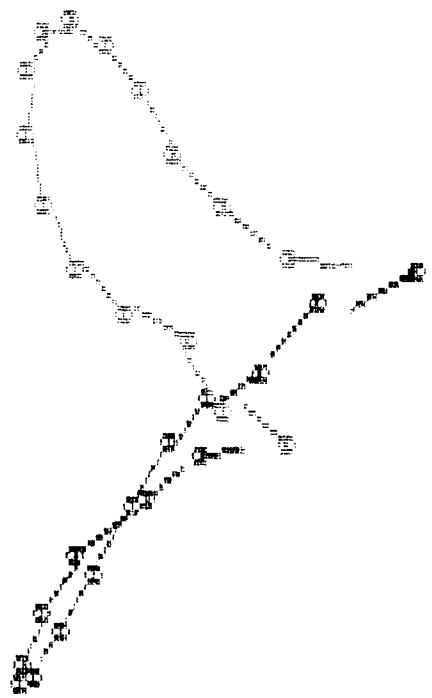

$z, t = 0.049$

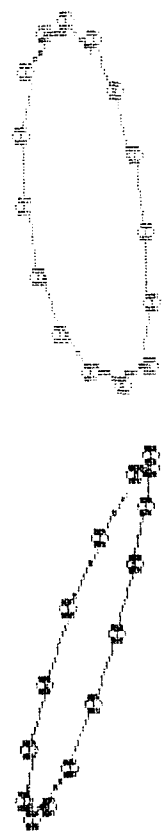

$z, t = 0.040$

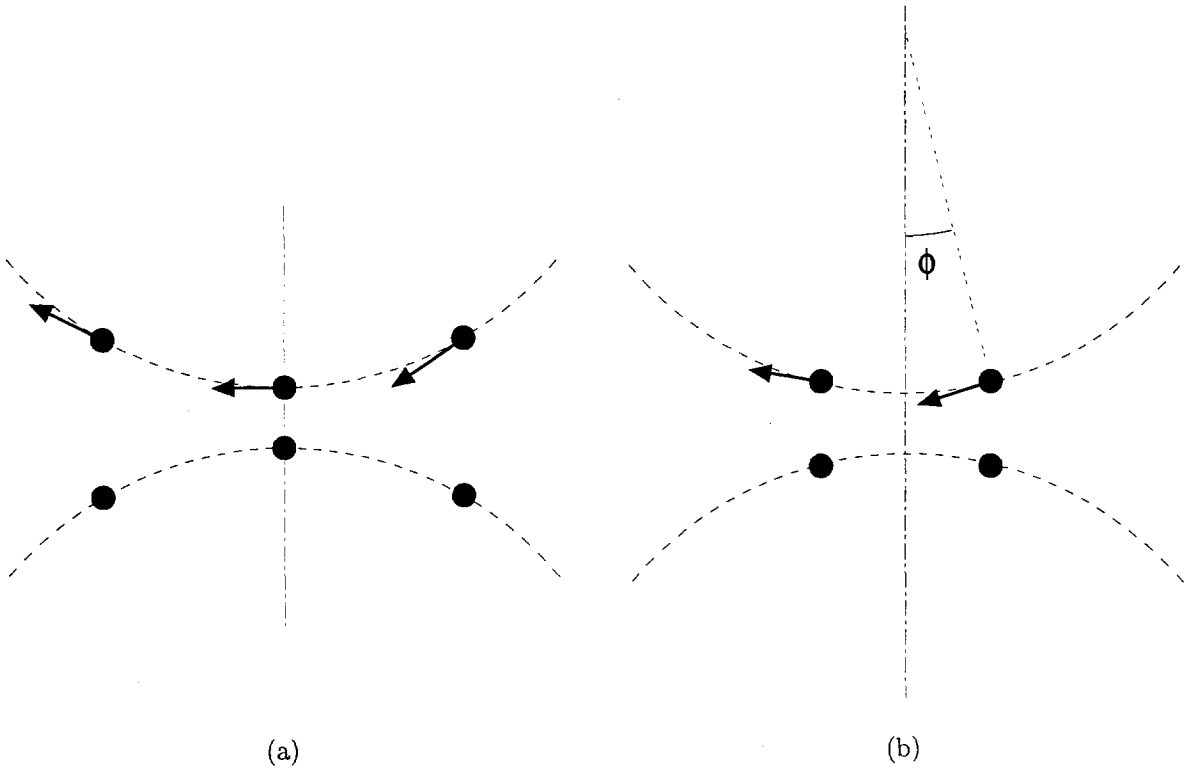

Figure 10.31: Two possbilities for the initial positions of the vortons in the configuration of fig.10.25 (seen from the left; for the lower ring only vorton locations are drawn): (a) $\phi/(2\pi/N) = 0.0$, (b) $\phi/(2\pi/N) = 0.5$.

Figure 10.32: (*see inserted sheets*) Oblique interaction of two vorton rings ($R = 1.0$, $\Gamma = 820$, $N = 15$). Vorton deformation according to (a) N-equation; (b) K-equation; (c) N+K-equation. Configuration as in (i) fig.10.31(a); (ii) fig.10.31(b). Dots indicate vorton locations, arrows indicate vorton strength vectors; the two rings are colored by different grades of black. The pictures are shown from two different points of view (compare fig.10.25): x = along the x-axis, z = along the z-axis. t = time.

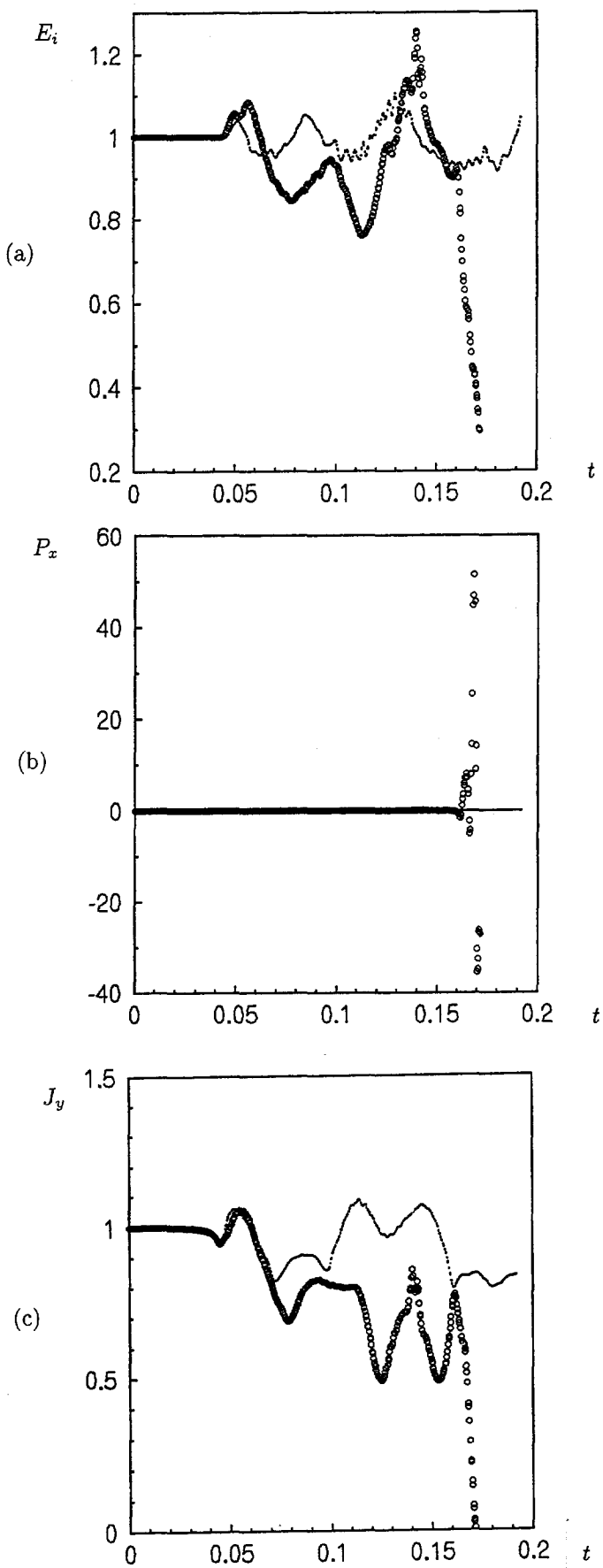

Figure 10.33: Comparison of the simulations shown in (o) fig.10.32(a)(ii) (N-equation) and (·) fig.10.32(c)(ii) (N+K-equation). (a) x-component of linear momentum, $\boldsymbol{P}$, according to (9.5) (scaled with initial value); (b) y-component of angular momentum, $\boldsymbol{J}$, according to (9.8); (c) interaction-energy E_i according to (9.10) (scaled with initial value). t is time.

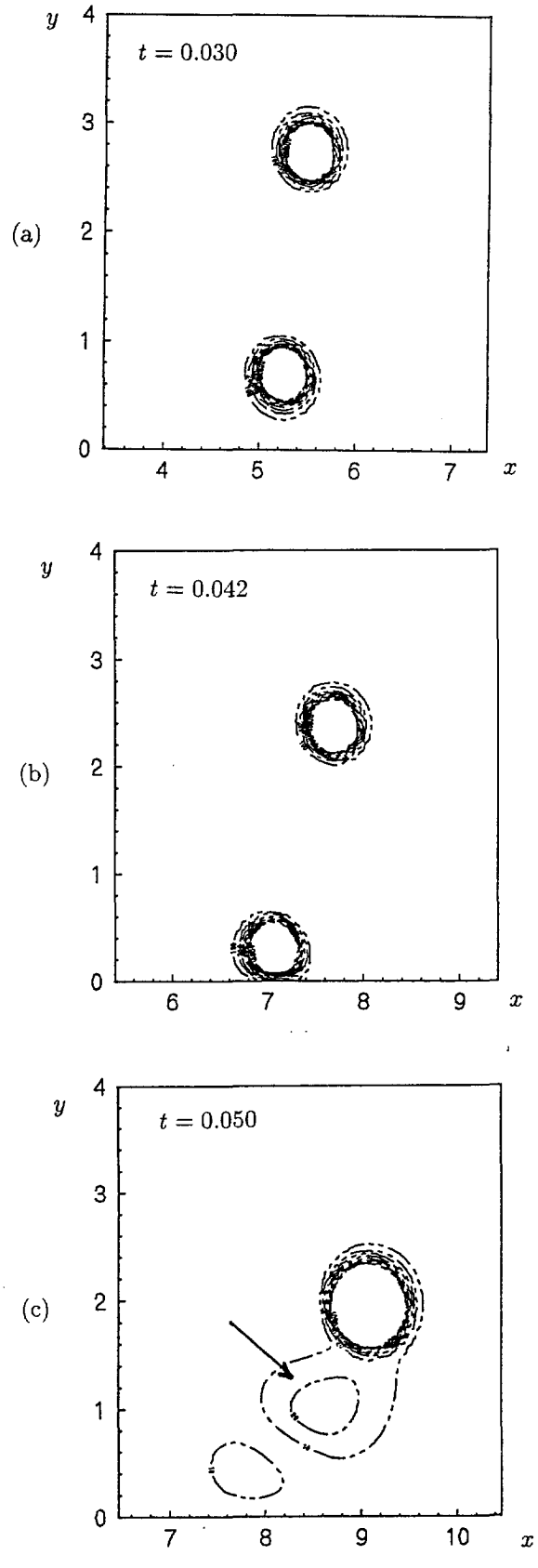

Figure 10.34: Oblique interaction of two vorton rings for the configuration of fig.10.32(c)(ii): contour plots of $|\ \bar{\mathbf{w}}\ |$. Cross-sections in $x-y$-plane for upper ring only. (a) $t = 0.030s$, (b) $t = 0.042s$, (c) $t = 0.050s$. The arrow indicates a possible thread.

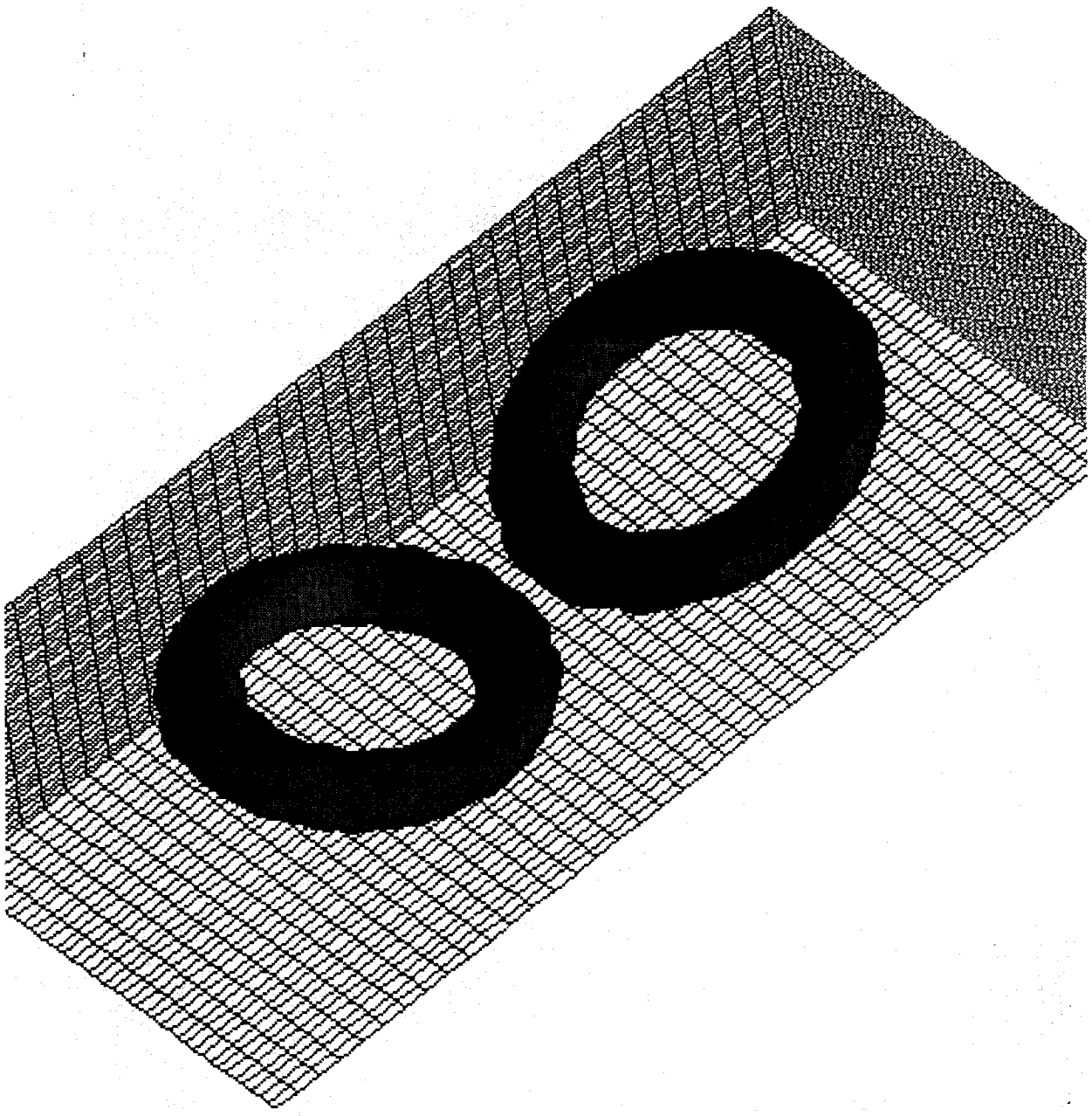

(a) $t = 0.040$.

Figure 10.35: (*continued on next pages*) Oblique interaction of two vorton rings (configuration as in fig.10.32(c)(ii)): isosurfaces of $|\ \bar{\mathbf{w}}\ |$ (given by (9.18)). t is time. Compare fig.10.27.

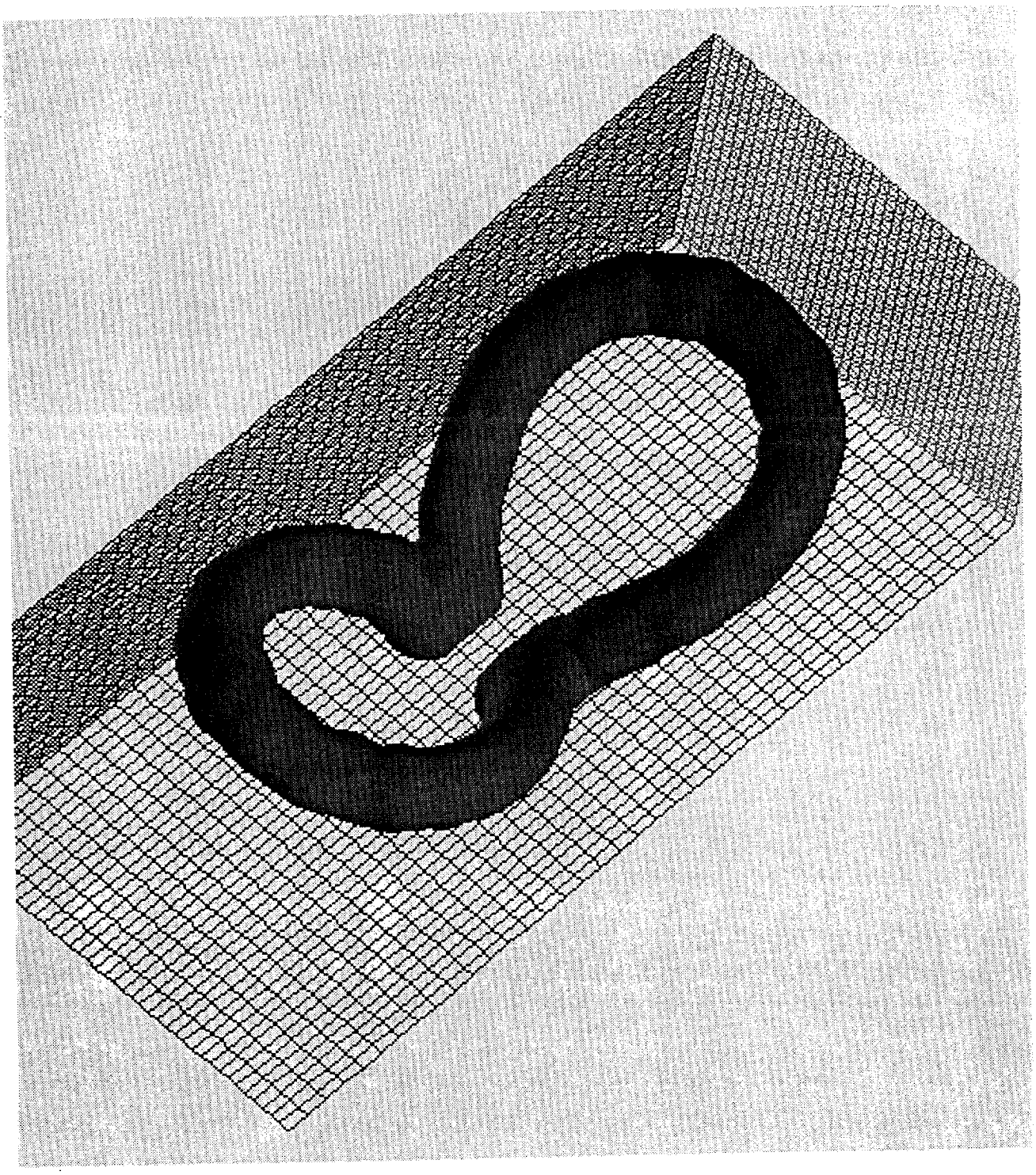

(b) $t = 0.046$.

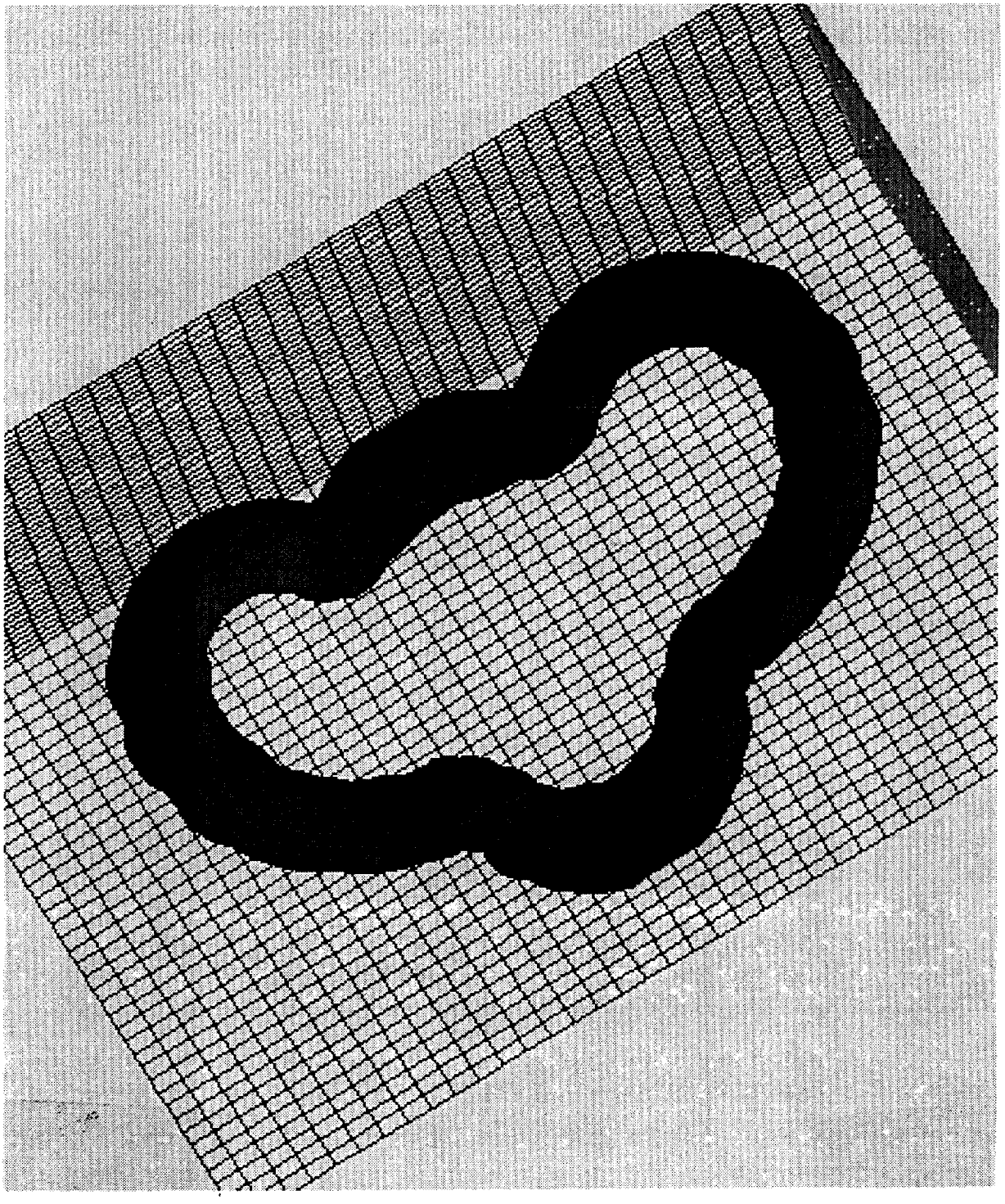

(c) $t = 0.050$.

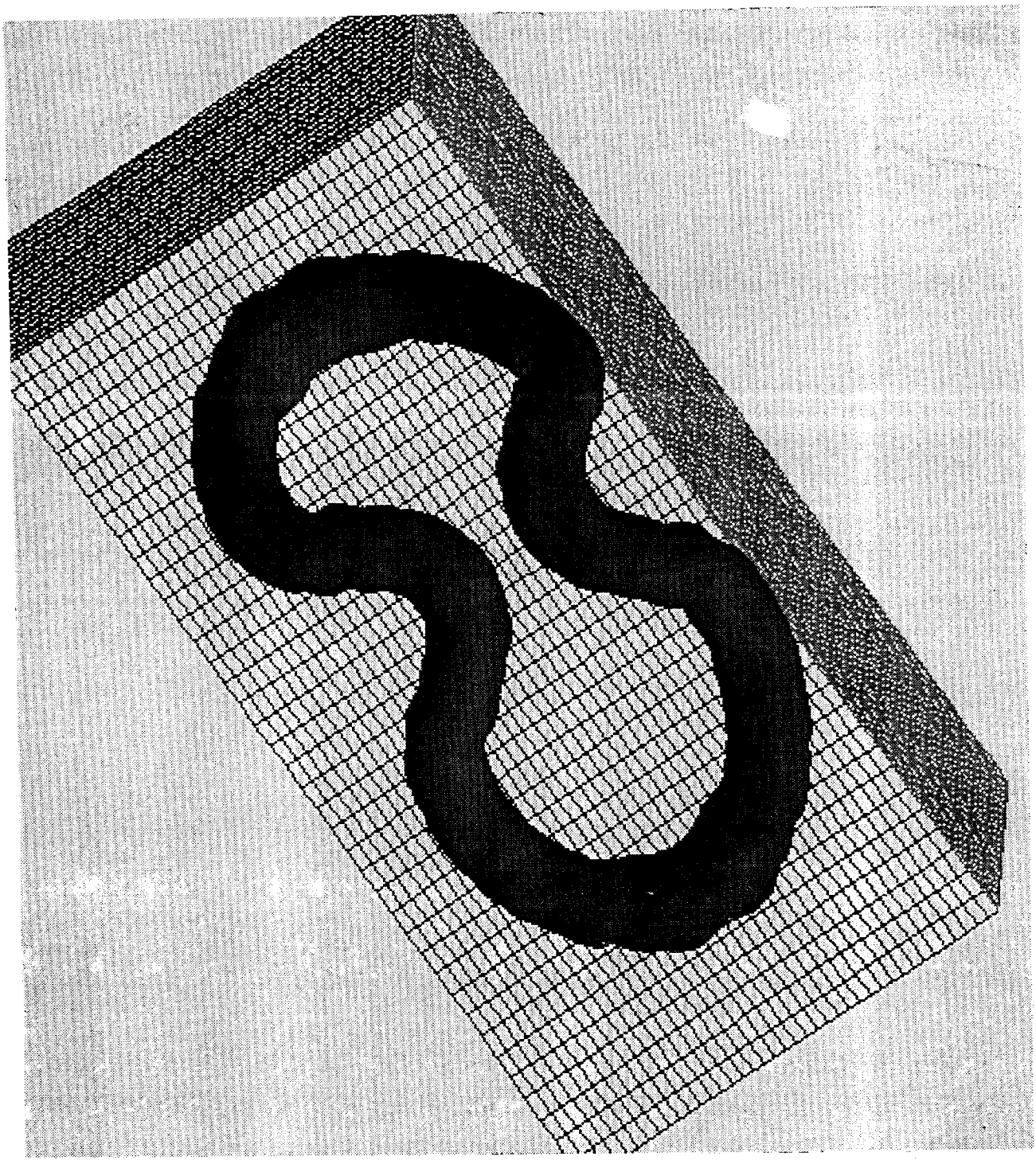

(d) $t = 0.060$.

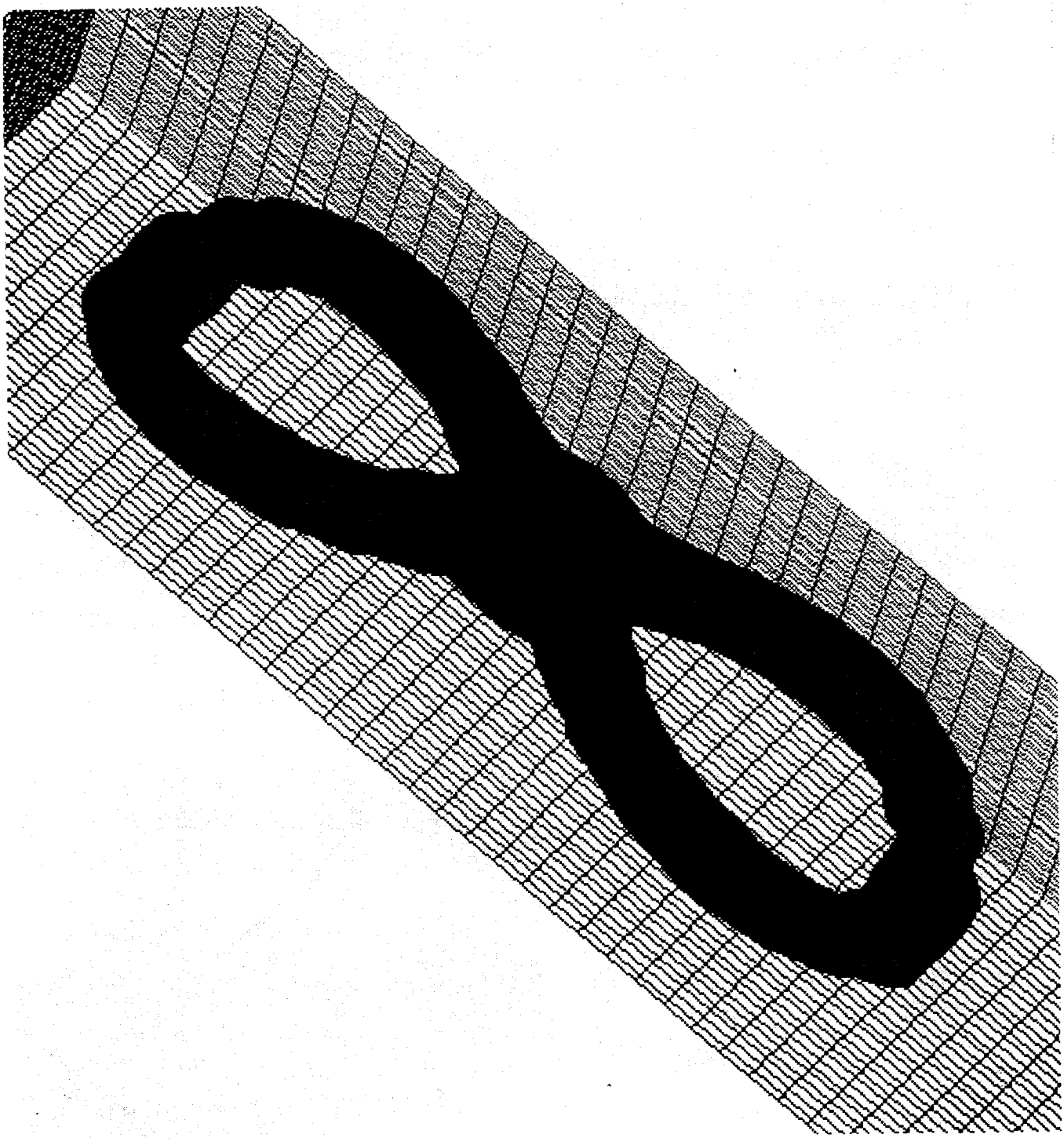

(e) $t = 0.070$.

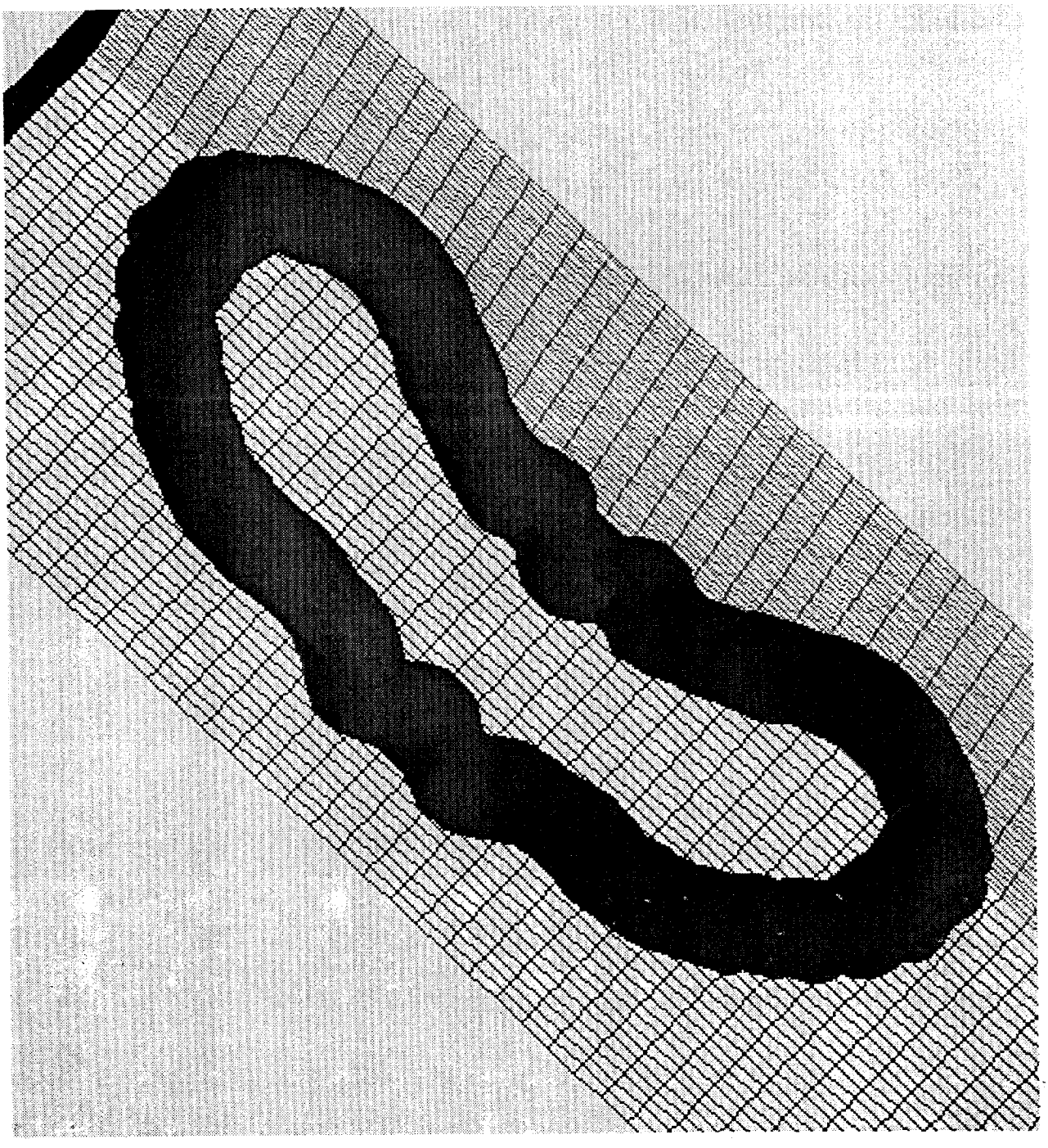

(f) $t = 0.105$.

We have also investigated the susceptibility of the simulation results to the value of the angle ϕ as defined in fig.10.31, i.e. to the locations of the vortons. For the N+K-equation the simulations have been repeated for several values of $\phi/(2\pi N)$ between 0.0 (fig.10.31(a)) and 0.5 (fig.10.31(b)): 0.125, 0.25, and 0.375. In all cases the interaction of the two vorton rings ended in chaotic vorton motions. However, when the distance between the rings' centres D was decreased to $2.5R_0$ instead of $4R_0$, we found for all three values of ϕ and for the N+K-equation that the behaviour appeared to be similar to that shown in fig.10.32(c)(ii) and chaotic behaviour held off. Application of the N- and K-equation to this configuration *did* lead to the appearance of chaotic behaviour, showing once again the superiority of the N+K-equation.

Finally, we discuss the consequences of the application of the "division with updating" procedure (see §9.4) to the case of fig.10.32(c)(ii). We have found that during the reconnection of the two rings the condition for vorton division was not met with and consequently no increase of the number of vortons was observed. However, division took place during the approach of the straight parts of the connected vorton rings as shown in fig.10.35(e). The division in this case appeared to have a negative influence on the development of the vorton configuration. The vortons started to show chaotic behaviour and the simulation had to be terminated.

When the initial number of vortons N in each ring was increased from 15 to 16, the condition for division was satisfied. However, during the reconnection vortons were added such that a "tail" of vortons formed behind the forward-moving connected vorton rings. This tail consisted of vorton "dipoles" as shown in fig.10.32(c)(i). Due to the small distance between the vortons in these dipoles, the timestep in the simulation was seriously reduced and finally chaotic behaviour appeared.

In both cases mentioned above, the problem can be attributed to the effect of division as shown in fig.10.36. The number of vortons starts to increase quickly. Though initially the vortons remain neatly aligned, at a certain moment instability behaviour sets in. This is most probably due to the growing misalignment of the vortons caused by the crude interpolation procedure, explained in §9.4.

10.5 Interaction of Two Knotted Vorton Rings

10.5.1 Introduction

The vortex configurations treated so far show symmetry in one or more planes. As a consequence, several motion-invariants like total angular momentum and total helicity are zero and remain perfectly conserved apart from slight fluctuations around zero due to numerical errors. One of the simplest configurations in which asymmetry has essential consequences and which has non-zero helicity, is that of two knotted vortex rings as shown in fig.10.37. Besides, this configuration is one of the most elementary in which the alignment of vortex tubes can be investigated (see §C of the Interlude).

10.5.2 Recent Results from Literature

The configuration of two knotted rings shown in fig.10.37 already appeared in Kelvin's paper "On vortex motion" [245] of 1869 (see Kelvin's letter to Helmholtz in §3.2 and fig.4.1). However, it got little attention for many decades, presumably due to the obvious lack of experimental results. Only the advent of numerical methods renewed interest in this problem. Some recent numerical results are listed below:

- Leonard & Chua [123] studied the configuration of fig.10.37 by means of a soft-vorton method (see Appendix B), which included a "core-spreading diffusion equation" for the

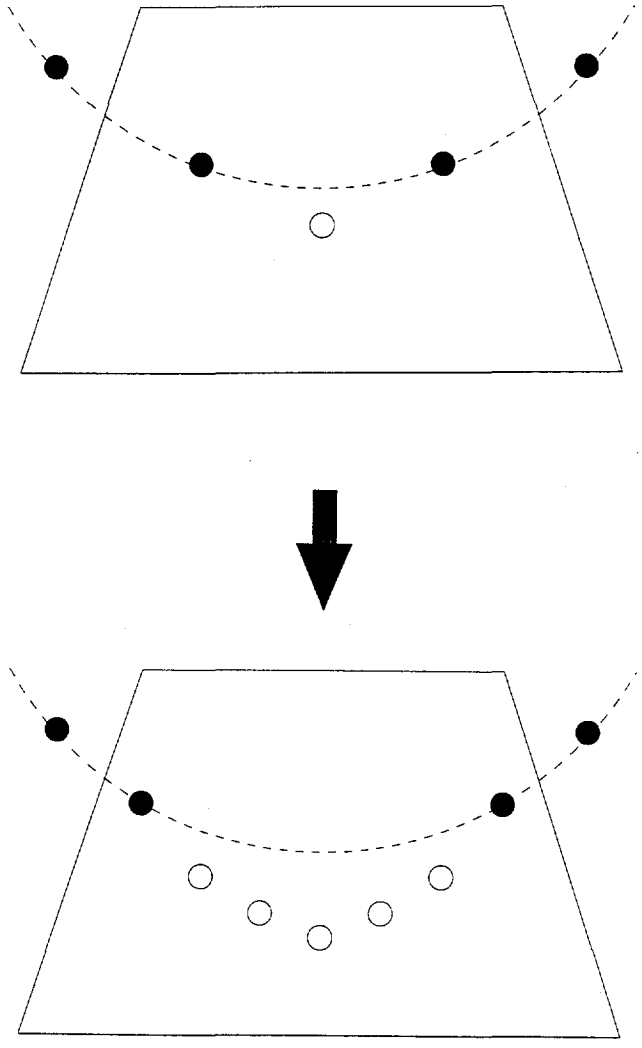

Figure 10.36: Result of vorton division (with updating) on the behaviour of two obliquely interacting vorton rings. Added vortons are indicated by open dots at the vorton locations. "Mirrored" vortons are not shown. The arrow indicates time development.

core size parameter and a viscous diffusion scheme. The cores of their rings consisted of several vortex lines comparable to the vorton ring shown in fig.10.28. Their simulation showed the formation of a "anti-parallel double tube structure". However, this structure showed no reconnection or even annihilation of vorticity.

- Aref & Zawadzki [15] applied a vortex-in-cell method (already mentioned in §10.4.2). They also observed the anti-parallel alignment of parts of the rings and claimed that these aligned parts would annihilate eahc other due to diffusion, leaving a single ring-like structure. However, this is not shown by their pictures; see fig.10.38.
- Winckelmans [283] applied a smoothed-vortex-filament method (see §7.3.1) and found the same results as Leonard & Chua. He also applied a soft-vorton method (K-equation),

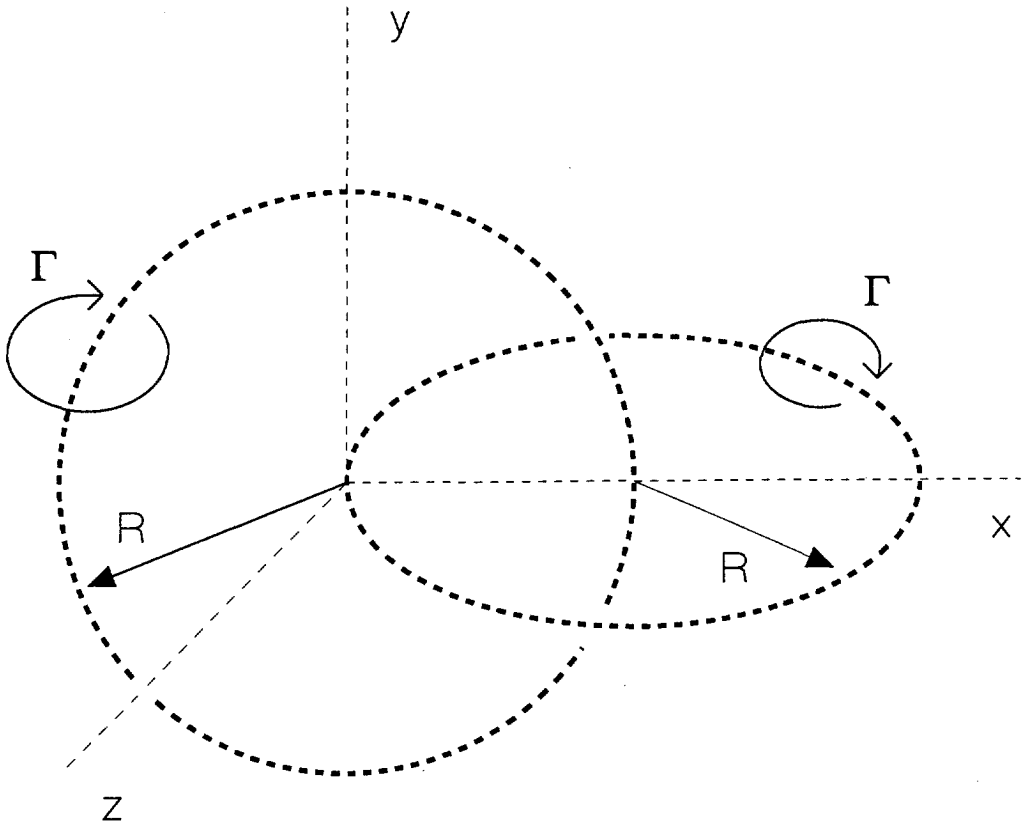

Figure 10.37: Initial configuration of two knotted vortex rings.

with and without inclusion of a vorton division scheme and his "procedure of relaxation of vorticity divergence" (see note **2** of Chapter 9). Alignment occurred but the subsequent interaction of the aligned tubes remained unclear and exhibited considerable violation of conservation of helicity. A simulation in which viscous diffusion had been included (see §10.4.2) showed no differences, due to the small convective timescale.

An even more elementary configuration to study anti-parallel alignment is the interaction of two initially orthogonally offset vortex tubes, as shown in fig.f of the Interlude. From direct numerical simulations, Zabusky *et al.* [288] suggested that the influence of the "double-layer" formed by the tubes is only local and that the topology of vortex lines contributes to limiting vortex stretching. They found that after alignment, reconnection occurred [15]. Pedrizzetti [178] simulated the interaction of two initially orthogonal vortex filaments by means of the vorton method (N-equation) and found reconnection.

[15] Zabusky and co-workers (e.g. in [288]) have also suggested that their numerical results may explain turbulence phenomena. They found a highly distorted vortex ring as debris after the process for which they suggested a similarity to the Falco ring, a structure which has been claimed to play a certain role in turbulent boundary layer flows (to be discussed in §10.6.1). The intense energy-dissipation clusters which have been found in homogeneous turbulence might be related to the regions where reconnection occurred. In these regions they observed "bursting", i.e. a sudden increase of local vorticity and dissipation.

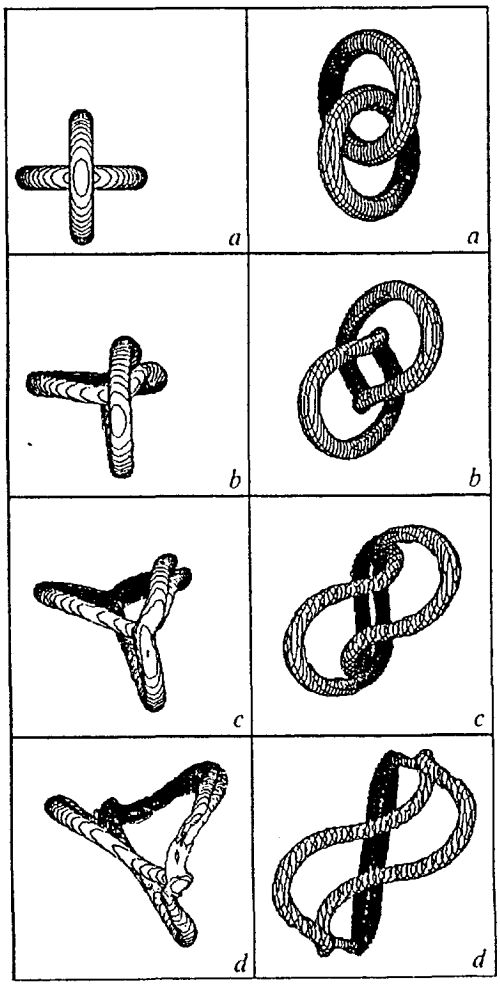

Figure 10.38: Numerical results of Aref & Zawadzki for the configuration of two knotted vortex rings as shown in fig.10.37. Isosurfaces of vorticity magnitude. Time development from top to bottom, two views are shown. From [15].

We have to conclude that the simulations mentioned above have not led to a conclusive picture of the development of two linked rings. If reconnection really takes place, we could wonder whether it is of the same kind as that of the obliquely interacting vortex rings discussed in §10.4. Kida & Takaoka [102] and Boratav *et al.* [27] have suggested that this is not the case, though an exact description of the difference appears to be still lacking.

10.5.3 Numerical Results

For our simulation of the configuration shown in fig.10.37, we have used two standard vorton rings ($N = 36$ for each ring) and applied all three vorton equations. For the N+K-equation we observed anti-parallel alignment as in the simulation of Aref & Zawadzki (see fig.10.38). For the other two cases, irregular behaviour started almost immediately after $t = 0$ and alignment did not occur. However, in case of the N+K-equation, the simulation also ended in a severe increase of the strength and chaotic behaviour of some vortons. No reconnection-like phenomena could

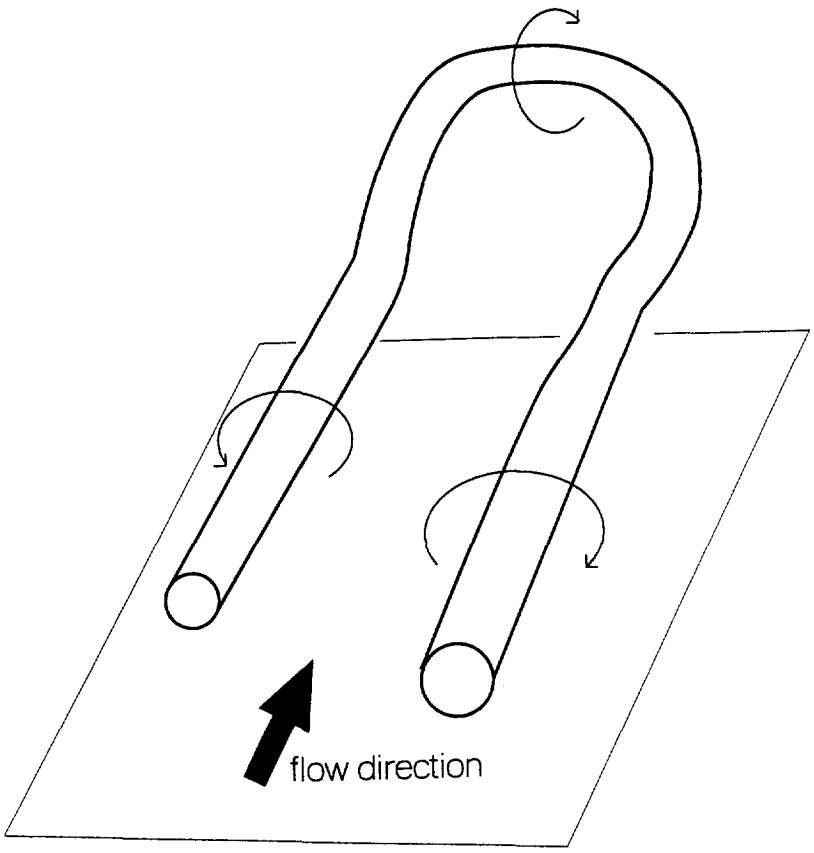

Figure 10.42: A horseshoe vortex.

First of all, we have to remark that the existence, let alone the role, of HVs is still a point of discussion. Though already proposed in the 1950s, experimental evidence of the existence of the HV only began with the flow visualizations of Head & Bandyopadhyay [74] in 1981. They showed that vertical cross-sections of elongated vortex structures made angles of 45° with the wall.

Despite ongoing controversies, the existence of HVs in TBL is nowadays generally accepted (see [68] for references; see also Smith & Lu in [107]). However, there is lack of knowledge on their formation, growth, destruction, regeneration, and contribution to gross statistics. We refer to e.g. [195] for further information. A survey of conceptual HV models can be found in Robinson's paper in [73].

Few experimens on controlled HVs have been published. Acarlar & Smith [2] studied the behaviour of HVs shed from a hemisphere in a laminar boundary layer. They concluded that between the legs of a HV low-momentum fluid is lifted up. Due to the interaction with higher-speed outer flow, secondary vortices are generated in proximity of the primary HV. These secondary vortices strongly interact with the original HV, generating chaotic structures which suddenly eject away from the wall. "These events appear very similar to the break-up stage of the burst sequence observed in turbulent boundary layers" (compare fig.10.41).

Smith *et al.* in [73] found that a viscous-inviscid interaction of a HV with the flow near the

be observed.

In order to get a better view of the alignment, we show in fig.10.39 the isosurface of $|\ \bar{\boldsymbol{w}}\ |$, given by (9.18). It shows the touching of the vortex tubes, though at this level of $|\ \bar{\boldsymbol{w}}\ |$ a hole seems to exist in the middle of the alignment area. We also observe nonuniform thickening and thinning of the tubes. Unfortunately, shortly after this time instance the simulation had to be stopped due to exponential growth of vorton strengths.

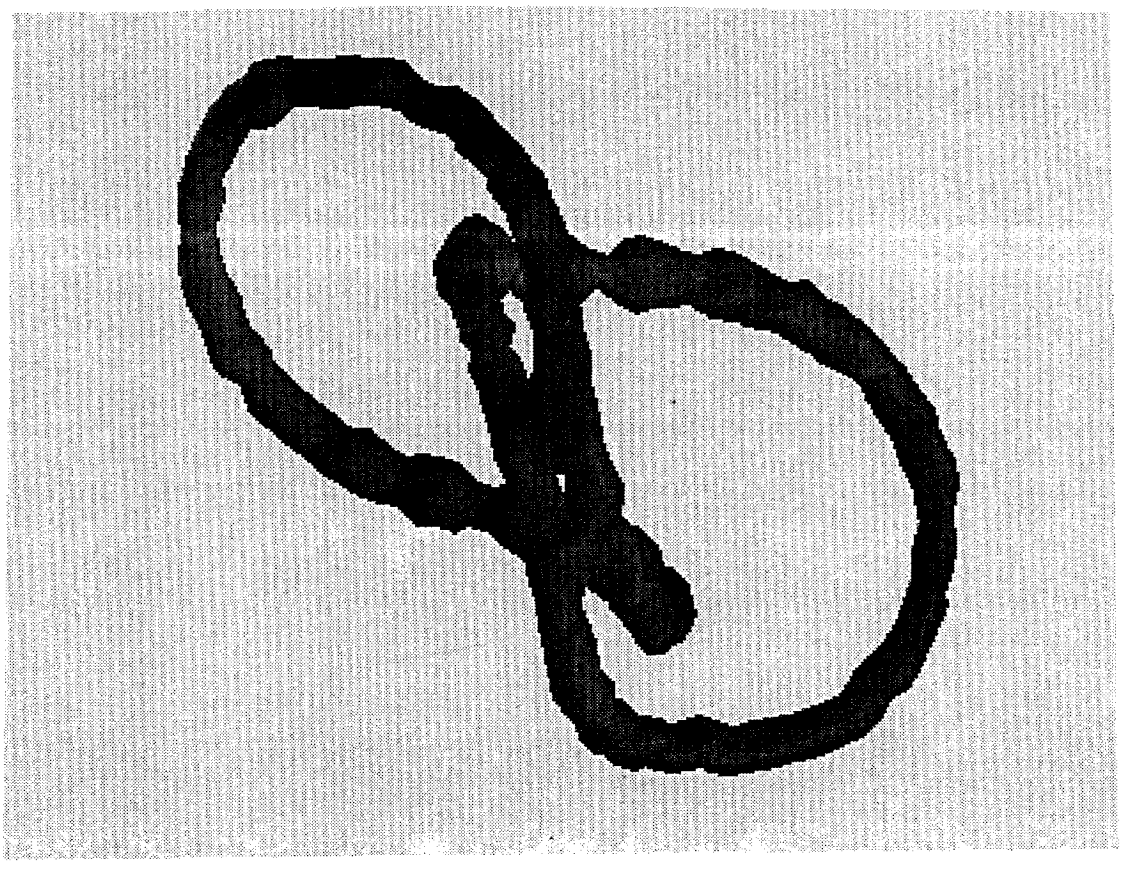

Figure 10.39: Interaction of two knotted standard vorton rings ($N = 36$): isosurface of $|\ \bar{\mathbf{w}}\ |$. Time $t = 0.0031\ s$.

In fig.10.40 we have plotted the development of several diagnostics for the case of the N+K-equations. We observe good conservation of all quantities up to time $t \approx 0.0032$, the moment the behaviour of the vortons starts to become chaotic. In this figure, also the influence of vorton division with updating (see §9.4) is shown. Though application of division appears to be able to extend the period of conservation of motion-invariants, it does not prevent severe violation of this conservation. This indicates that in case of division the vorton behaviour also gets irregular, though this is not immediately clear from the vorton visualizations (not presented here). Most probably the cause can be attributed to the development illustrated in fig.10.36.

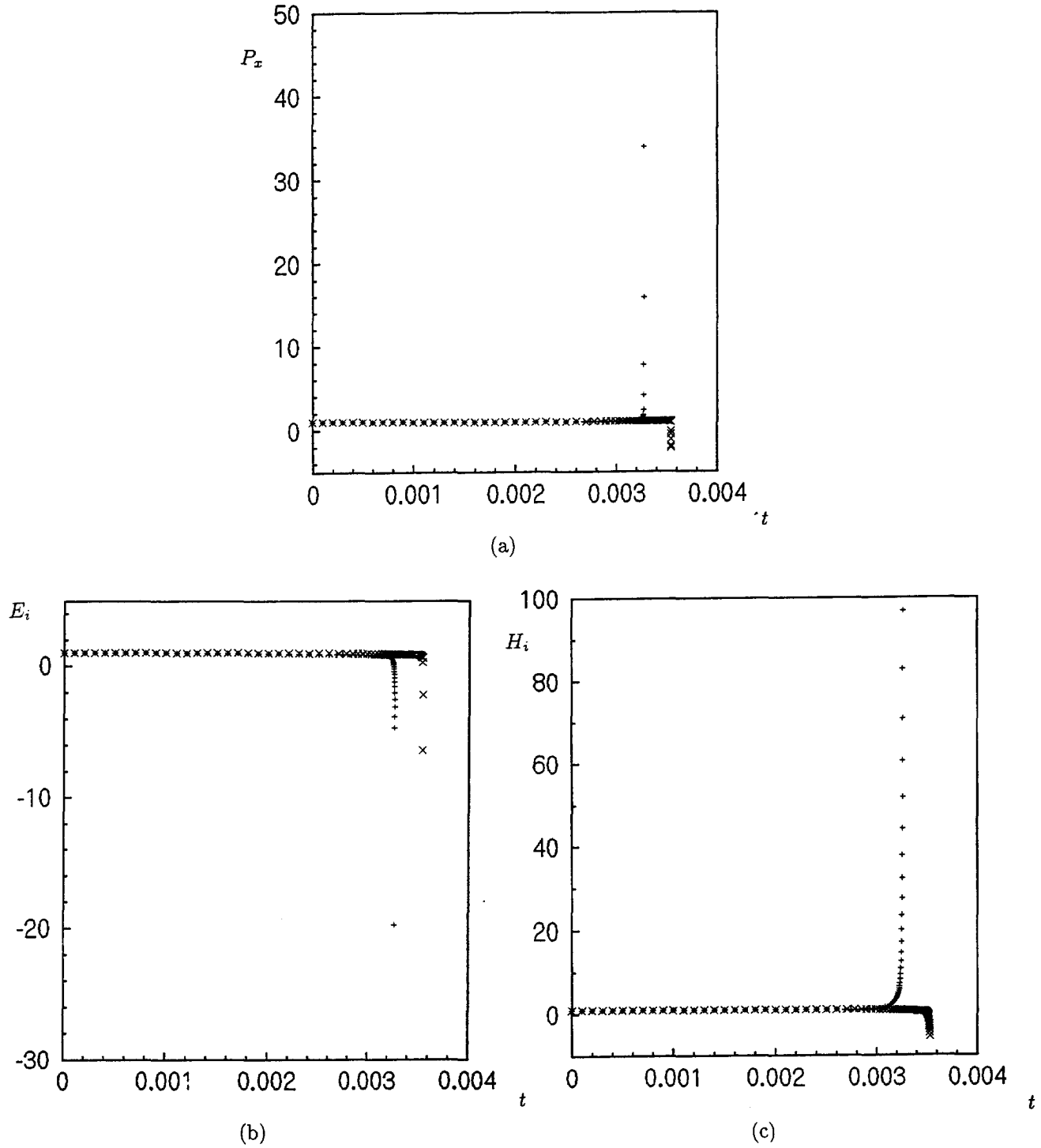

Figure 10.40: Interaction of two knotted standard vorton rings ($N = 36$): development of diagnostics. N+K-equation. (a) x-component of linear momentum $\boldsymbol{P}$ according to (9.5), (b) interaction-energy E_i according to (9.10), (c) interaction-helicity H_i according to (9.16); (all quantities are scaled with their initial values). Simulations performed (+) without and (×) with vorton division with updating. t is time.

10.6 Single Vorton Ring in a Shear Flow above a Flat Plate

In this last section we discuss the simulation of the behaviour of a single vortex ring in the neighbourhood of a flat plate in a shear flow. Since the 1970s, mainly due to publications by Falco (see below), this configuration is regarded as a possibly useful model of a coherent structure (CS) in a turbulent boundary layer (TBL) flow. It may provide some insight into this still poorly understood turbulent phenomenon.

In §10.6.1 we will present two of the several vortical structures which have been proposed as essential elements of TBL flows, i.e. the horseshoe vortex and the vortex ring. Besides, attention is given to the possible relation between both structures. In §10.6.2 the results of our vorton simulation will be discussed. This simulation has been especially set up to investigate the influence of the so-called outer layer parameters of the shear flow on the development of this CS model.

10.6.1 Structures in the Turbulent Boundary Layer

In §B of the Interlude, we have seen that vortical structures, generally referred to as coherent structures, are considered to be essential elements of turbulent flows. In this thesis we will restrict attention to one of the least understood turbulent flows with regard to its "structures", i.e. the TBL flow [16].

If we limit our attention to coherent (vortical) structures in turbulent boundary layers, we already encounter a huge amount of questions. From Robinson's discussion of the objectives of turbulence-structure research [195], the following problems can be derived:

- what is the 3-D spatial character of each of the known structural features of the TBL?
- how are the various structural features related to each other in space and in time?
- what range of vortical structure topologies exists in the flow?
- what is the range of strengths (e.g. circulation) of vortex structures?
- to what extent do vortical structures play a role in determining the average production and dissipation of turbulent kinetic energy and Reynolds shear stress [17]?
- how do vortical structures form, evolve, regenerate, and die?
- what is role of the outer layer in determining details of near-wall turbulence production?
- what is the repeating sequence of events that is responsible for maintenance of turbulence, including the role of all known structures?

These questions show that research on CS has set itself a difficult task. Several models have been proposed to describe the mechanisms taking place in a TBL flow. An example is the picture which has been presented by Hinze [89]; see fig.10.41. This figure especially shows the "cyclic" process related to the phenomenon of "bursting". Bursting (see e.g. [62]) is generally used to refer to outward eruptions of near-wall fluid, resulting in a strong temporary increase of transport of momentum (or: high values of Reynolds shear stress). However, definition and usage of the term "bursting" has been confusing (see e.g. [196, Ch.12]). Numerical simulations have shown that the production of turbulence by "bursts" in the near-wall region is much more

[16] See e.g. [28], [195], and Robinson in [73] for a review of recent developments in this area.

[17] The Reynolds shear stress will be defined in §10.6.2.

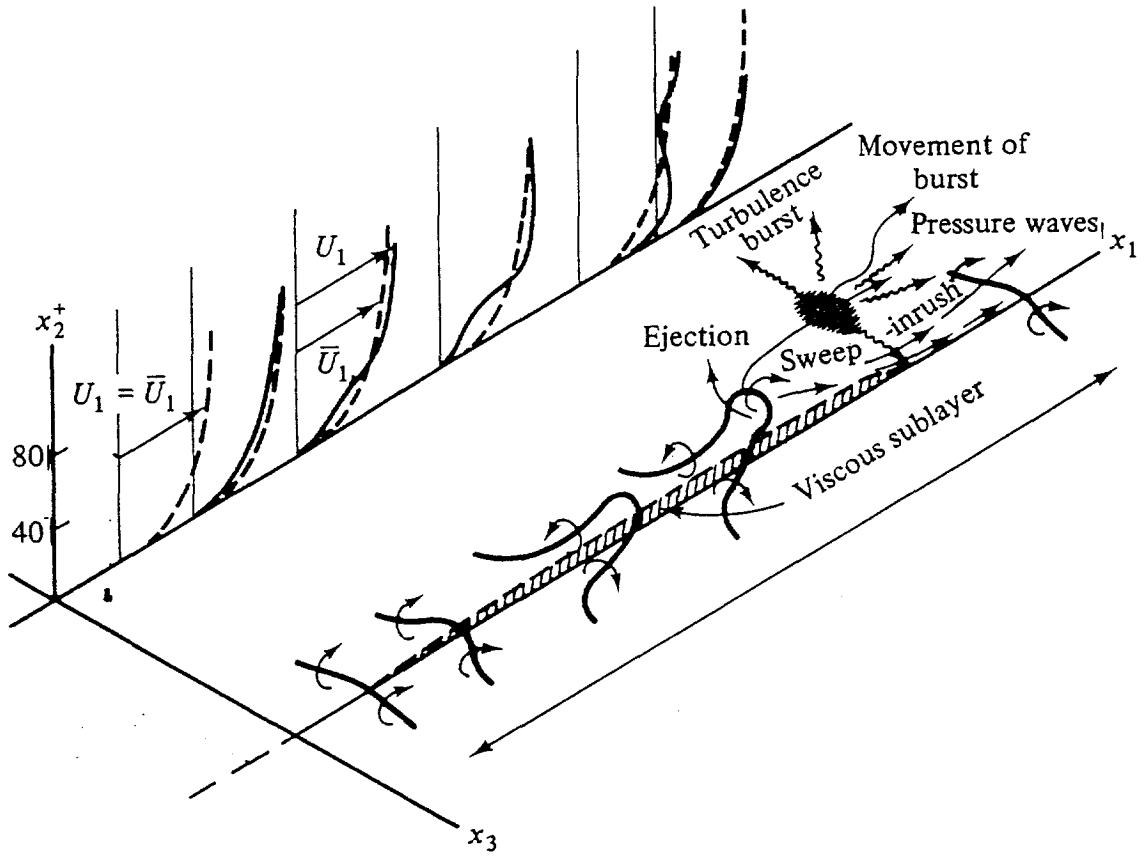

Figure 10.41: A model of the behaviour of vortical structures in a turbulent boundary layer. From [89].

intermittent in space than in time. This indicates that regions of bursting move along with the main (shear) flow.

Fig.10.41 shows how a spanwise vortex line, initially undisturbed, is deformed into a so-called horseshoe vortex. Due to an instability in the velocity profile of the flow, a burst takes place [18].

A much discussed aspect of bursting has been the parameters determining its frequency of occurrence. Does it scale with the inner or outer layer parameters? The controversy is still going on in literature (see e.g. Hussain [92] and Lumley *et al.* in [32]). We will return to this issue in §10.6.2.

Below we will treat two vortex structures which have been introduced in literature and which have been proposed as essential elements of the TBL: the horseshoe vortex, which we have already introduced, and the vortex ring, which may be related to the former.

Horseshoe Vortices

The horseshoe vortex (HV) has a shape as shown in fig.10.42 [19].

[18] We refer to Hinze's description in [89] for fuller details.

[19] The term hairpin vortex has been introduced for a HV of larger slenderness; here, we will regard both as having essentially the same structure.

wall caused an eruption of surface fluid which resulted in secondary vortices, probably similar to those observed by Acarlar & Smith. This suggests that the no-slip condition at the wall is of essential importance in this process.

Rogers & Moin [198] found evidence of the existence of HVs in homogeneous turbulent flows. Their results suggested that these structures do not necessarily require a wall for their formation, and that they may also develop in the presence of only a mean shear flow. However, they remarked, the shear must not be too large in order to allow the formation of HV. "The similarity in vortex structure between the homogeneous shear flow and inhomogeneous channel flow gives strong justification for the study of homogeneous 'building-block' flows as a stepping stone to understanding more complex flows".

Vortex Rings

The first to attribute importance to vortex rings in the TBL has been Falco (see [39] for references). He found that the outline of the TBL has the shape of large-scale bulges. At the upstream side of the bulges he visually identified coherent vortices, to which he coupled the name of "typical eddy". These Eddies, he concluded, contribute most to the production of Reynolds shear stress in the outer region and their evolution can explain the existence of streamwise vortices and horseshoe-like vortices in the TBL.

The typical eddies have been identified by Falco as a kind of vortex rings. To study their influence in boundary layer flows, Chu & Falco [39] did experiments on the interaction of vortex rings moving towards and away from a so-called Stokes' layer generated by a moving wall. This interaction led to many structural features of TBL like low-speed streaks, pockets, and HVs. The authors concluded that their results show the essential importance of vortex rings in the TBL.

With regard to the generation of typical eddies, Falco has proposed a "pinch-off" mechanism of vortex rings from Ω-shaped HV-like vortex structures; see fig.10.43. This formation process

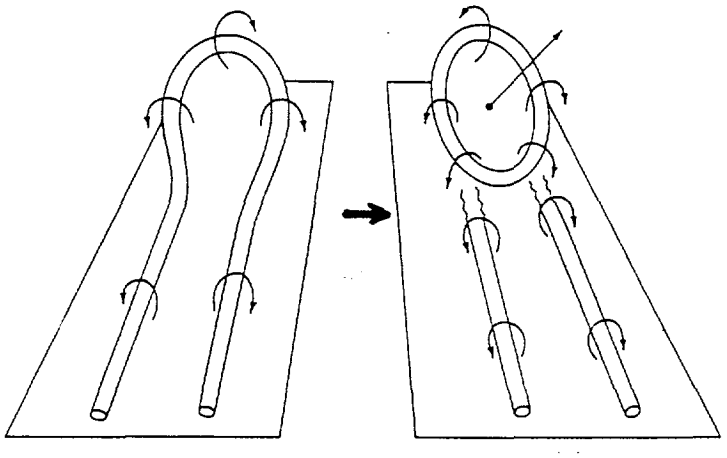

Figure 10.43: Pinch-off of a vortex ring from a Ω-shaped horseshoe vortex. Big arrow indicates time development. From [107].

was investigated by Moin *et al.* [163] who performed a numerical simulation of parabolically-shaped vortex filaments in a shear flow, modelling a HV. They applied a vortex-filament method, and hence didn't take into account vortex deformation. They indeed found pinch-off of vortex rings for parabolic shear flow profiles while linear shear profiles appeared to impede this phenomenon [20].

Evidence for the existence of vortex rings in the TBL is still lacking. For instance, Robinson [196] did not observe vortex rings or anything likewise during his diagnosis of numerical data provided by a DNS-study of a TBL. Elementary experimental studies on vortex rings near walls are still scarce. Experiments of rings in shear flows seem to be limited to that by Chu & Falco mentioned above. Walker *et al.* [274] studied the impact of a vortex ring in quiescent flow on a no-slip wall. He found the generation of secondary vorticity at the wall [21], which was ejected after some time to form a secondary vortex ring. This caused wavelike instabilities on the primary vortex ring and the flow field degenerated into smaller and smaller 3-D motions. In the end, the authors found that "the end result is an apparently chaotic flow which appears to be turbulent" and remarked a similarity with bursting in the TBL. However, they also suggested that vortex configurations in the TBL are more complicated than simple vortex rings and that the formation of secondary vorticity may be essential to understand TBL flows.

As remarked above, Falco has suggested that typical eddies may be related to horseshoe-like vortices in the TBL. However, it seems that the issue of a possible relation between typical eddies and HVs has gained only little attention from others. According to Adrian in [107] a HV can be decomposed into a vortex ring plus a mean shear plus two streamwise vortices as illustrated in fig.10.43 . The vortex rings and/or HV dominate in the outer layer and streamwise vortices dominate the wall layer. The same picture has been sketched by Klebanoff *et al.* [106], who did very extensive experiments on the transition to turbulence in a boundary layer, induced by roughness elements. They regarded the TBL as consisting of two regions: in the inner region the turbulence is generated by a complex interaction of HVs and other vortical structures induced by the obstacles; in the outer region the HV generate turbulent vortex rings. The latter may be responsable for the bulges the authors observed at the edge of the boundary. However, they found no convincing evidence for the existence of Ω-shaped HVs as suggested by Falco, but they didn't exclude them either. The authors concluded that the eddies in the outer region do not (directly) contribute to the transition to turbulence in the TBL, whereas the HVs *are* intrinsic to this process and to developing turbulence.

10.6.2 Vorton Simulations

Though we have to conclude that the existence and the role of vortex rings in the TBL is still uncertain, we try to make a contribution to the understanding of this role by considering the elementary configuration sketched in fig.10.44: a single standard vorton ring in a shear flow above an infinitely extended flat plate. We realize that we will not be able to simulate phenomena related to the no-slip condition at the wall (e.g. generation of secondary vorticity). Therefore, it is better to investigate a situation like the one presented here in which these phenomena are supposed to be absent or of minor importance.

[20] Morrison *et al.* [164], however, concluded that the pinching-off as found in simulations by Moin *et al.* [163] can only be a relatively rare phenomenon.

[21] A similar study by Lim [127] showed the same result.

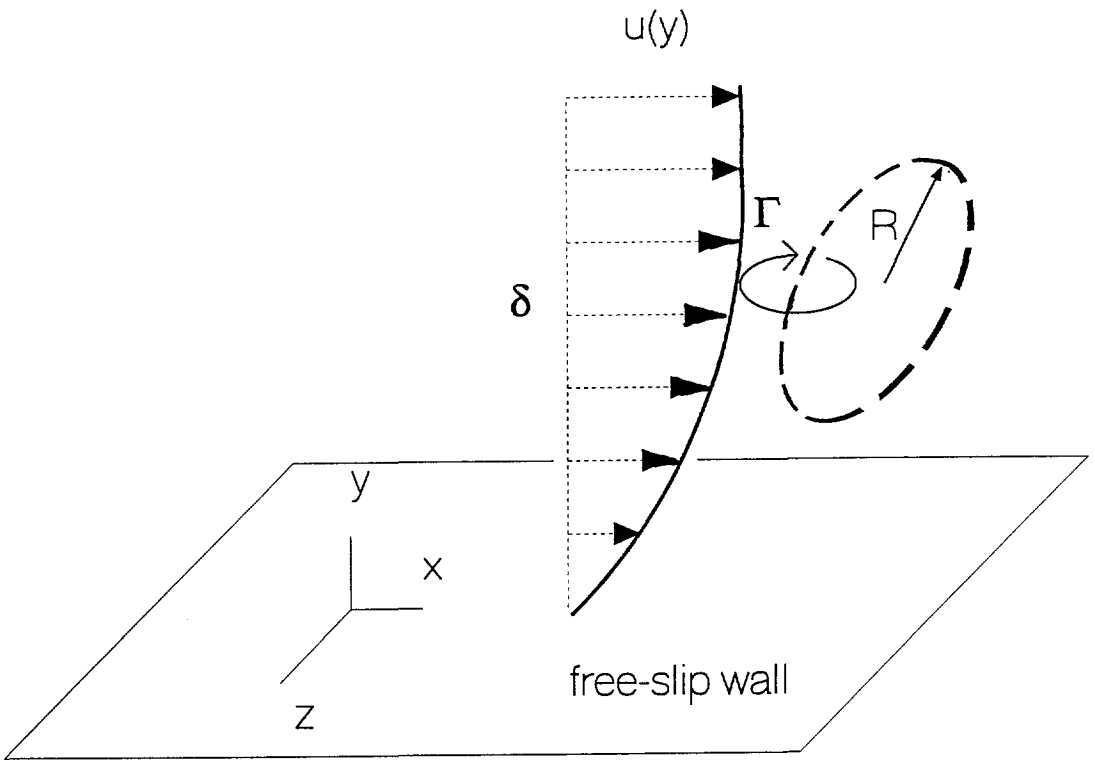

Figure 10.44: Initial configuration for the single vorton ring in a shear flow above a flat plate.

The ring is initially at an angle of 45° with the $x-z$-plane and its center is located at $y = H$. Its velocity is directed away from the plate. The flat plate is simulated by means of a mirrored vortex ring (compare fig.7.1). In our simulations we will take the $x-z$-plane as (infinitely extended) boundary plane. The parameters of the mirrored vorton α' of a vorton α are given by:

$$(r_{\alpha'})_x = (r_\alpha)_x \ , \ (r_{\alpha'})_y = -(r_\alpha)_y \ , \ (r_{\alpha'})_z = (r_\alpha)_z \tag{10.6}$$

and

$$(\gamma_{\alpha'})_x = -(\gamma_\alpha)_x \ , \ (\gamma_{\alpha'})_y = (\gamma_\alpha)_y \ , \ (\gamma_{\alpha'})_z = -(\gamma_\alpha)_z \tag{10.7}$$

where the index x, y, and z indicate the components of the vectors. These relations provide a free-slip condition, since the tangential velocity at the plate will generally not be zero.

The shear flow is represented by a one-dimensional velocity profile $\boldsymbol{v}_s = (u(y), 0, 0)$. The results by Moin *et al.* [163] (see §10.6.1) suggest that a linear shear flow is not consistent with the formation of vortex rings in shear flows. Therefore, we have chosen the following profile [22]:

$$u(y) = U \tanh \frac{3y}{\delta} \tag{10.8}$$

In this profile the quantity δ can be interpreted as the height of the boundary layer and U as the outer layer velocity since, due to the factor 3, the velocity $u(\delta) = 0.995U$. For δ we take the value 1.

[22]The profile does not need to have an inflection point, as has been shown by Kim in [53]. The profile used here has already been proposed by Novikov [170].

The simplest manner to include a shear flow into the vorton equations is to take into account only the advection of the vortons by the local shear velocity $\boldsymbol{v}_s$. However, we have to realize that the shear flow will also cause vortex deformation of the vortex ring and that the shear flow profile in its turn will be changed due to the velocity field induced by the vortex ring.

For a consideration of the importance of inclusion of these two phenomena in a simulation, we refer to an estimation by Aref & Flinchem [12] of the effect of the shear flow on a vortex filament. Their theoretical consideration led to the conclusion that only taking into account advection is a valid approximation to order a/Δ where a is a measure for the core of the filament and Δ is a measure of the shear profile height (comparable to our parameter δ in (10.8)). However, they remark that the estimation becomes invalid when transverse oscillations of the filament introduce other length scales. This means that the approximation may become invalid in time.

To fulfil the condition given by Aref & Flinchem mentioned above, we have to require:

$$\frac{R_c}{\delta} \ll 1 \tag{10.9}$$

where R_c the core size of the vortex ring. As shown in §10.1.1, for a vorton ring R_c may be taken proportional to the distance between the vortons in the ring. Consequently, the number of vortons has to be as large as possible in order to be sure that taking into account only advection is sufficient for reliable simulations. Since we use a relatively small numbers of vortons in our simulation, we have added the effect of vortex deformation due to the shear flow (as has been proposed by Novikov [169]). This means that, in the N+K-equation, $(\dot{\boldsymbol{\gamma}}_\alpha)_x$ has been extended with $(\dot{\boldsymbol{\gamma}}_\alpha)_y \partial u/\partial y|_{y=(\boldsymbol{r}_\alpha)_y}$ and $(\dot{\boldsymbol{\gamma}}_\alpha)_y$ has been extended with $(\dot{\boldsymbol{\gamma}}_\alpha)_x \partial u/\partial y|_{y=(\boldsymbol{r}_\alpha)_y}$. The change of the shear flow profile due to the vortex ring will not be included, i.e. the function $u(y)$ remains unaltered.

Fig.10.45 shows the development of the configuration of fig.10.44 for a standard vorton ring in case of the N+K-equation. We observe four stages:

1. the ring moves away from the plate, at the same time deforming into a non-circular (somewhat elliptical) shape and rotating along its horizontal axis;
2. due to its rotation the ring moves into the direction of the plate;
3. having approached the plate closely, part of the deformed ring is pinched-off as a smaller ring-like vortex structure, which starts to move away from the plate;
4. the part which has remained near the plate starts behaving chaotically and the simulation has to be stopped.

Our purpose is to investigate the possible existence of burst-like phenomena in this simulation and the possible influence of the outer parameter U. To this end, we consider as a

Figure 10.45: (*see inserted sheets*) Development of the configuration of fig.10.44 for a standard vorton ring ($N = 18$). Two views of the same simulation are given: (a) view along the x-axis, (b) view along the z-axis. t is time.

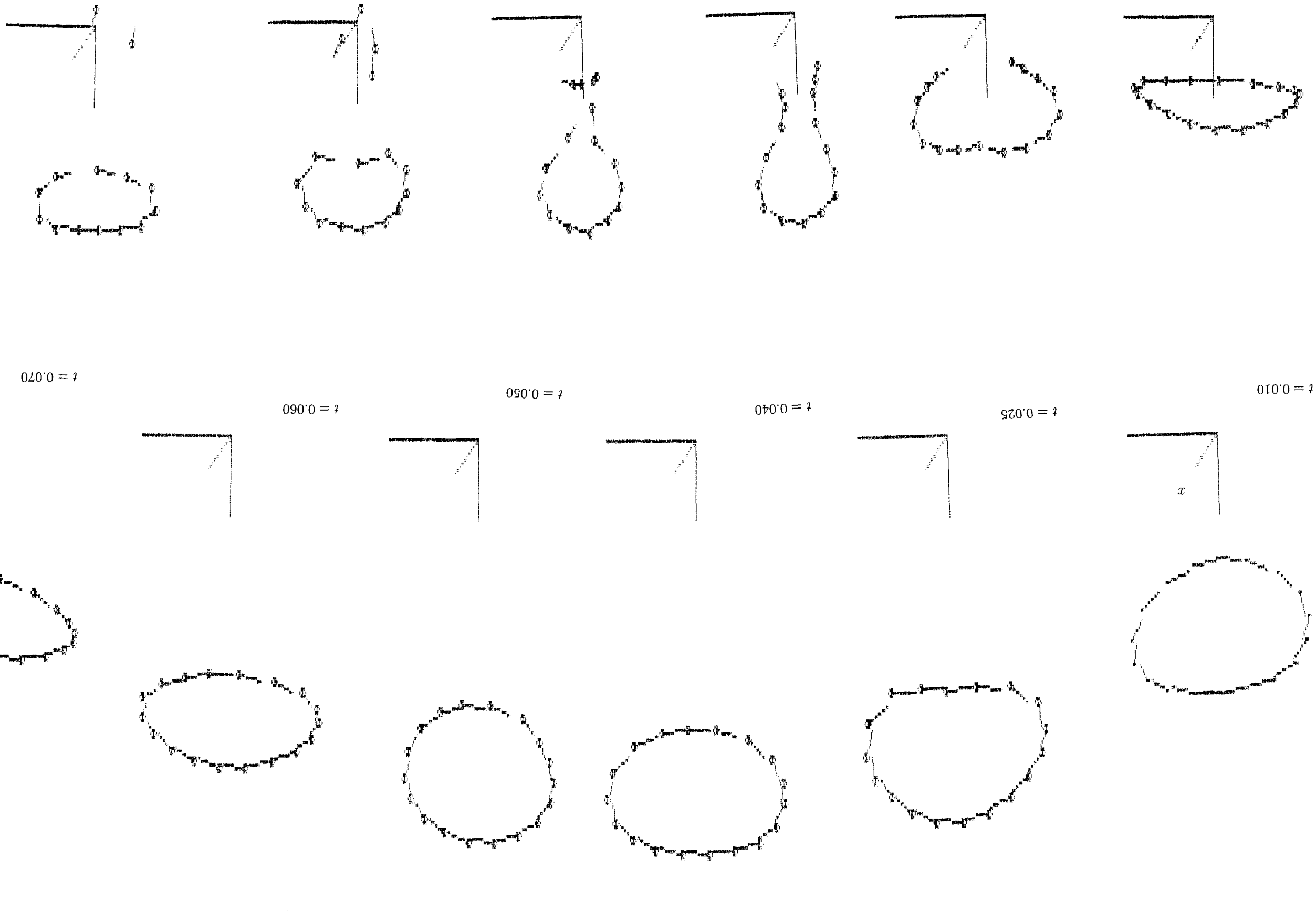

Figure 10.45 (a)

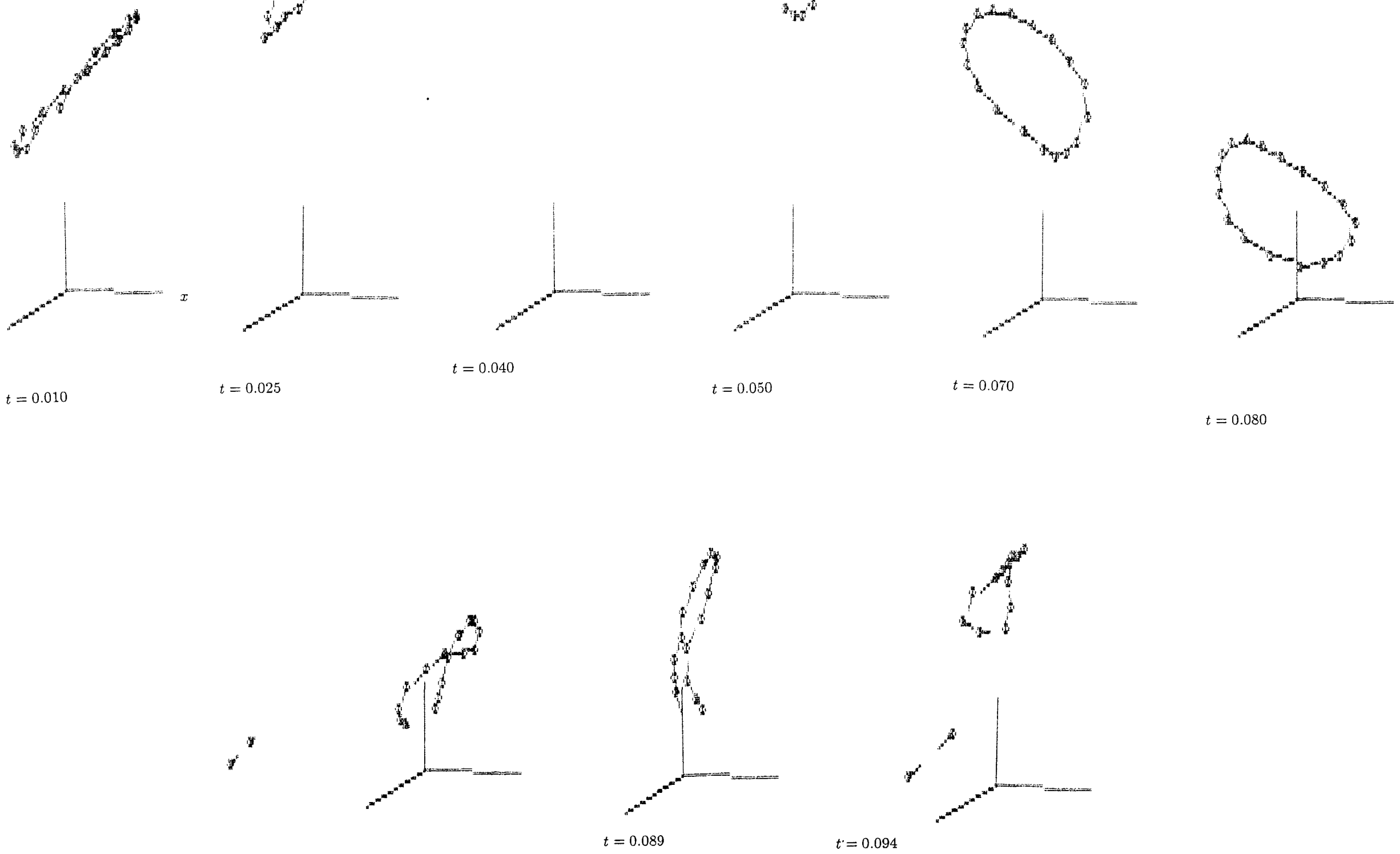

Figure 10.45 (b)

diagnostic the quantity given by uv, where u and v are the x- and y-component of the velocity field $\boldsymbol{v}$, respectively. This velocity field consists of the vorton field given by (8.10) and the shear flow field $\boldsymbol{v}_s$ mentioned above. The quantity uv will be called the Reynolds shear stress [23] and it indicates transport of momentum. Since bursts are supposed to transport momentum in the positive y-direction, we only regard the components given by $u > 0, v > 0$ and $u < 0, v > 0$. They have been calculated at the points of a grid of height δ and extending sufficiently far into the x- and z-direction. Of all grid points, the maximum value of the Reynolds shear stress is calculated [24]. In fig.10.46 these values are plotted against time for the case $U = 100$.

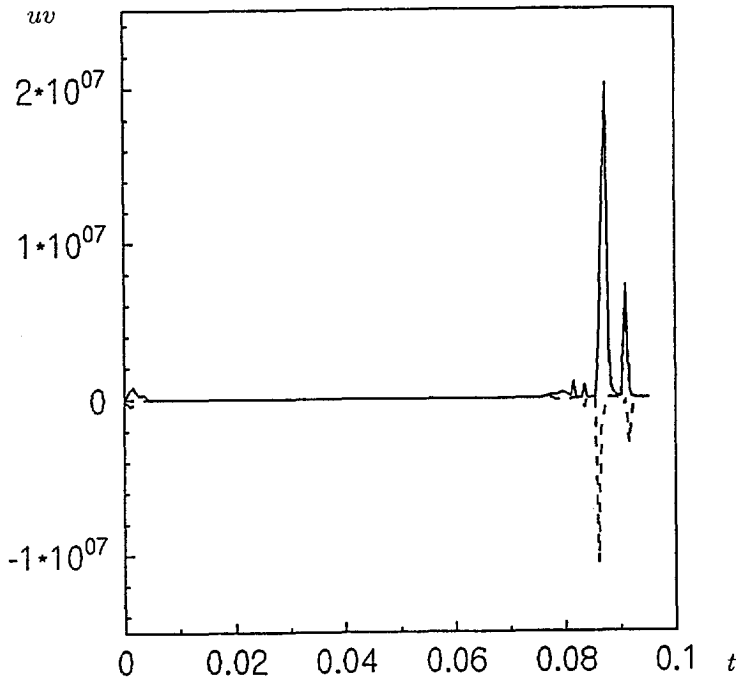

Figure 10.46: Configuration of fig.10.44 for a standard vorton ring ($N = 18$): maximum values of Reynolds shear stress uv ($v > 0$, (—) $u > 0$ or (- - -) $u < 0$) vs. time t. $U = 100$ (see (10.8)).

We observe an intense increase of both components of the Reynolds shear stress occurs at about the same moment, which will be indicated by t'. In table 10.1 we have plotted the dependence of time t' up to bursting on the characteristic velocity U of the shear flow (see (10.8)). We conclude that the outer flow parameter U constitutes a characteristic of this model of the TBL. However, it may be clear that it would be rather premature to conclude that the burst frequency in a TBL is determined by the outer flow.

[23] In turbulence, the Reynolds shear stress is usually defined as the correlation between velocity fluctuations, i.e. $\overline{u'v'}$.

[24] The contributions to the Reynolds shear stress from the vortons near the wall which start to behave irregularly at the end of the simulation shown in fig.10.45 have not been included.

U	t'
90	0.094
95	0.090
100	0.086
105	0.081
110	0.071
115	0.069

Table 10.1: Configuration of fig.10.44 for a standard vorton ring ($N = 18$): shear flow velocity U vs. time to burst t' (see fig.10.46) .